

2014-01-01

Fused Deposition Modeling (FDM) Fabricated Part Behavior Under Tensile Stress, Thermal Cycling, And Fluid Pressure

Mohammad Shojib Hossain

University of Texas at El Paso, shojib.me@gmail.com

Follow this and additional works at: https://digitalcommons.utep.edu/open_etd



Part of the [Mechanical Engineering Commons](#)

Recommended Citation

Hossain, Mohammad Shojib, "Fused Deposition Modeling (FDM) Fabricated Part Behavior Under Tensile Stress, Thermal Cycling, And Fluid Pressure" (2014). *Open Access Theses & Dissertations*. 1259.

https://digitalcommons.utep.edu/open_etd/1259

This is brought to you for free and open access by DigitalCommons@UTEP. It has been accepted for inclusion in Open Access Theses & Dissertations by an authorized administrator of DigitalCommons@UTEP. For more information, please contact lweber@utep.edu.

FUSED DEPOSITION MODELING (FDM) FABRICATED PART BEHAVIOR
UNDER TENSILE STRESS, THERMAL CYCLING,
AND FLUID PRESSURE

MOHAMMAD SHOJIB HOSSAIN
Department of Mechanical Engineering

APPROVED:

Ryan Wicker, Ph.D., Chair

Yirong Lin, Ph.D.

Sara M. Gaytan, Ph.D.

Charles Ambler, Ph.D.
Dean of the Graduate School

Copyright ©

by

Mohammad Shojib Hossain

2014

Dedication

This thesis is dedicated to my mother, my father, and my brother who have always been my inspiration

FUSED DEPOSITION MODELING (FDM) FABRICATED PART BEHAVIOR
UNDER TENSILE STRESS, THERMAL CYCLING,
AND FLUID PRESSURE

by

MOHAMMAD SHOJIB HOSSAIN, B.Sc. in Mechanical Engineering

THESIS

Presented to the Faculty of the Graduate School of

The University of Texas at El Paso

in Partial Fulfillment

of the Requirements

for the Degree of

MASTER OF SCIENCE

Department of Mechanical Engineering

THE UNIVERSITY OF TEXAS AT EL PASO

August 2014

Acknowledgements

I want to express my gratitude to my supervisor and mentor Dr. Ryan Wicker, director of the W.M. Keck Center for 3D Innovation (Keck Center), for his continuous support, encouragement, guidance and constructive comments throughout my research as a graduate student. I would like to thank Mr. David Espalin, manager of the Keck Center, for his continuous support in the research, his contribution of many ideas and encouraging me in different aspects. For that, I am really grateful to him. I would like to thank Dr. Corey M. Shemelya for helping me with the thermal cycling testing. This research would not have been possible without the enormous research facility in Keck Center, expanded recently to over 13,000 sq. ft. and which provided access to state-of-the-art facilities and equipment as a result of funding from the State of Texas Emerging Technology Fund. I would like to thank my committee members, Dr. Yirong Lin and Dr. Sara M. Gaytan.

I would like to thank the former students, present students, and staff in the Keck Center. My special thanks goes to Mr. Jorge Ramos, Mr. Alejandro Cuaron, Ms. Lluvia Herrera, Mr. Jorge Ramirez, Mr. Juan Vargas, Mr. Alfonso Fernandez, Ms. Mireya Perez, Mr. Mahesh Tonde, and Mr. Luis A. Ochoa for their help in various aspects.

Finally, I would like to thank my parents and my brother for their continuous support and encouragement.

Abstract

Material extrusion based additive manufacturing (AM) technology, such as fused deposition modeling (FDM), is gaining popularity with the numerous 3D printers available worldwide. FDM technology is advancing from exclusively prototype construction to achieving production-grade quality. Today, FDM-fabricated parts are widely used in the aerospace industries, biomedical applications, and other industries that may require custom fabricated, low volume parts. These applications are and were possible because of the different production grade material options (e.g., acrylonitrile butadiene styrene (ABS), polycarbonate (PC), polyphenylsulfone (PPSF), etc.) available to use in FDM systems. Recent researchers are exploring other material options including polycaprolactone (PCL), polymethylmethacrylate (PMMA), composites containing ceramic, glass and metal fillers, and even metals which depict the diversified materials and possibility of new material options using FDM technology.

The understanding of the behavior and mechanical properties of the finished FDM-fabricated parts is of utmost importance in the advancement of this technology. The processing parameters, e.g., build orientation, raster width (RW), contour width (CW), raster angle (RA), and raster to raster air gap (RRAG) are important factors in determining the mechanical properties of FDM fabricated parts. The work presented here focused on the mechanical properties improvement by modifying those build parameters. The main concentration is on how modifying those parameters can improve ultimate tensile stress (UTS), Young's modulus, and tensile strain of the final product. In this research, PC parts were fabricated using three build methods: 1) default method, 2) Insight revision method, and 3) visual feedback method. By modifying build parameters, the highest average UTS obtained for PC was 63.96 MPa which was 7% higher than that of 59.73 MPa obtained using the default build parameters. The parameter modification using visual feedback method led to an increase in UTS of 16% in XYZ, 7% in XZY, and 22% in ZXY.

The FDM fabricated parts using PC were tested under thermal cycling of -30° C to 85° C. A series of experiments were performed (e.g., tensile test, deformation of fabricated part, glass

transition measurement) to evaluate the possibility of FDM fabricated parts in the harsh environment (embedded electronics, wiring in automotive industry, etc.). The UTS results showed that the results were not significantly different using statistical analysis after 150 thermal cycles while average Young's modulus increased from 1389 MPa to 1469 MPa after 150 thermal cycles. The highest warping of the specimen was found to be 78 μm which was the result of continuous thermal expansion and contraction.

A sealing algorithm was developed using LabVIEW and MATLAB programming. The LabVIEW program was developed to obtain the edge information of each layer of a 3D model part. The MATLAB programming was used to gather the output information from LabVIEW and calculate the suggested RW providing least amount of gap in between rasters and contours. As a result, each layer became sealed and was able to withstand air pressure within a pressure vessel. A test specimen was fabricated according to the developed sealing algorithm parameters and used to show entirely sealed walls capable of withstanding up to 138 kPa air pressure.

Table of Contents

Acknowledgements.....	v
Abstract.....	vi
Table of Contents.....	viii
List of Tables	x
List of Figures.....	xi
CHAPTER 1: Introduction	1
1.1 Background.....	1
1.2 Motivation.....	2
1.3 Thesis Objective.....	3
1.4 Thesis Outline	3
Chapter 2: Literature Review	4
2.1 Introduction.....	4
2.2 Fused Deposition Modeling.....	5
2.3 FDM Material	7
2.4 Previous Works on Modifying Processing Parameters.....	8
2.5 Thermal Cycling	10
2.6 Amorphous Polymer	12
2.7 Glass Transition Temperature.....	13
2.8 Previous Works on Sealing FDM Parts	14
CHAPTER 3: Materials and Methods	16
3.1 Thermoplastic Material: PC.....	16
3.2 Fabrication of Specimens.....	17
3.3 Parameter Modifications for Improving Mechanical Properties	18
3.4 Mechanical Testing.....	22
3.5 Density Measurement Specimens using Parameter Modifications.....	22
3.6 Processing Parameters of Specimens for Thermal Cycle Testing	23
3.7 Thermal Cycle Testing.....	24
3.8 Sealing Algorithm.....	26
3.9 Processing Parameter of Specimens for Pressure Test	40

3.10 Density Measurement Specimens using Sealing Algorithm.....	42
3.11 Pressure Testing.....	43
CHAPTER 4: Results	44
4.1 Parameter Modification Results.....	44
4.2 Thermal Cycle Testing Result	54
4.3 Sealing Algorithm result	58
CHAPTER 5: Conclusion and Recommendations	63
5.1 Conclusion	63
5.2 Recommendations for Future Work.....	64
References.....	66
Appendix A.....	70
Appendix B	75
Appendix C	78
Appendix D.....	82
Appendix E	87
Vita	91

List of Tables

Table 2.1: Different FDM machine comparison.....	5
Table 2.2: Selected properties of commercially available FDM materials.....	7
Table 2.3: Anisotropic properties of FDM fabricated parts.....	10
Table 2.4: Operation temperature of automotive electronic systems	11
Table 3.1: Processing parameters used in improving mechanical testing	19
Table 3.2: Build parameters for default method	20
Table 3.3: Build parameters for Insight revision method	20
Table 3.4: Build parameters for visual feedback method	21
Table 3.5: Build parameters for density measurement specimens using three build methods	22
Table 3.6: Processing parameters used in thermal cycling test specimens	24
Table 3.7: Thermal cycling test parameters.....	25
Table 3.8: Analysis of gaps between the rasters. At least five measurement were taken for each RW.....	37
Table 3.9: Analysis of surface roughness. Five different surfaces were taken to measure the surface roughness value	39
Table 3.10: Processing and building parameters used in pressure test specimens of flat plate	40
Table 3.11: Processing and building parameters used in pressure test specimens using sealing algorithm: square feature and circular dome	41
Table 3.12: Default processing and building parameters used in pressure test specimens and density measurement specimens	42
Table 4.1: Percentage UTS increase relative to UTS from default method.....	48
Table 4.2: t-test results comparing UTS of default and visual feedback method	50
Table 4.3: ANOVA table for UTS to compare results in 3 RAs for each method considering all three build orientations	50
Table 4.4: Density measurement result using build parameter modification	54
Table 4.5: Density measurement result.....	59

List of Figures

Figure 1.1: Schematic diagram of FDM Machine	2
Figure 2.1: Generic AM Process.....	4
Figure 2.2: FDM building parameters	7
Figure 2.3: Variation of volume as a function of temperature for amorphous polymer	13
Figure 2.4: Change of Young's modulus against temperature showing the glass transition temperature of an amorphous polymer	14
Figure 3.1: Chemical structures of PC	16
Figure 3.2: Process flow diagram of sealing algorithm	27
Figure 3.3: Edge pixel location based on gaining or losing edge	29
Figure 3.4: Edge calculation for number of contours	30
Figure 3.5: Schematic design consideration for conversion co-efficient measurements.....	32
Figure 3.6: Pixel to inch conversion for square prism considering Type I design	33
Figure 3.7: Pixel to inch conversion for circular dome considering Type II design	34
Figure 3.8: Pixel to inch conversion for both square feature and circular dome (both showed same result) considering Type III and Type IV design, respectively.	35
Figure 3.9: Adding or deleting rasters based on features.....	36
Figure 3.10: Deposition of raster showing gap at between raster and contour using three different RWs.....	38
Figure 3.11: Pressure test.....	43
Figure 4.1: Optical images of specimens build in XYZ orientation with gaps shown by black circles (parameters are set in mm)	44
Figure 4.2: Optical images of specimens build in XZY orientation with gaps shown by black circles (parameters are set in mm)	45
Figure 4.3: Optical images of specimens build in ZXY orientation with gaps shown by black circles (parameters are set in mm)	46
Figure 4.4: Ultimate tensile strength for a) XYZ build orientation b) XZY build orientation and c) ZXY build orientation.....	47
Figure 4.5: Schematic diagram raster deposition in ZXY build orientation.....	49
Figure 4.6: Young's modulus for a) XYZ build orientation, b) XZY build orientation and ZXY build orientation.	51
Figure 4.7: Tensile strain for a) XYZ build orientation, b) XZY build orientation and ZXY build orientation	52
Figure 4.8: Characteristic stress-strain curves for three build orientations	53
Figure 4.9: UTS result of thermal cycled specimen.	55
Figure 4.10: Young's modulus result of thermal cycled specimen.	56
Figure 4.11: Tensile strain result of thermal cycled specimen.	56
Figure 4.12: Deformation of thermal cycled specimen.	57
Figure 4.13: Glass transition temperature of thermal cycled specimen.....	58
Figure 4.14: Pressure testing on circular dome using default parameters.	60
Figure 4.15: Pressure testing on square feature using modified sealing algorithm parameters....	61
Figure 4.16: Pressure testing on circular dome using modified sealing algorithm parameters.	62

CHAPTER 1: Introduction

1.1 Background

Additive manufacturing (AM) is a fabrication process that uses computer aided design (CAD) to produce a solid model by adding material in a layer by layer fashion. Fused deposition modeling (FDM) is a material extrusion based AM process [1], which has traditionally been used for concept modeling prototypes, some functional prototypes, pre-surgical instruments and many other applications [2]. Recent researchers have focused on the advancement of the FDM technology to make production grade end use parts [3]. There are different processing parameters involved with the technology, such as build orientation, raster angle (RA), contour width (CW), raster width (RW), raster to raster air gap (RRAG), and more. Those parameters can play vital role in determining the end part quality. FDM built parts have yet to reach the quality in terms of mechanical strength, density, etc. in comparison to the plastic injection molding method. Modifications to these parameters can lead to achieving desired quality.

FDM technology requires a three dimensional CAD model to fabricate a part. The process involves extruding thermoplastic material in the X and Y direction of the build platform, in order to create a single layer of the part. After finishing the layer, the build platform moves down one FDM layer thickness and deposits a new layer on top of the previous one. This process continues until the entire part finishes. A point worth noting, a sacrificial support material is also deposited to fabricate complex geometries and overhanging features (Figure 1.1).

There are scopes for developing the suitable processing parameters for the FDM systems, which can lead FDM products to be more durable, and stronger than present condition. A thermal study can lead to determining the survivability of FDM parts in electronic applications, where temperature change is a major issue. A FDM fabricated part that is able to hold fluid pressure can

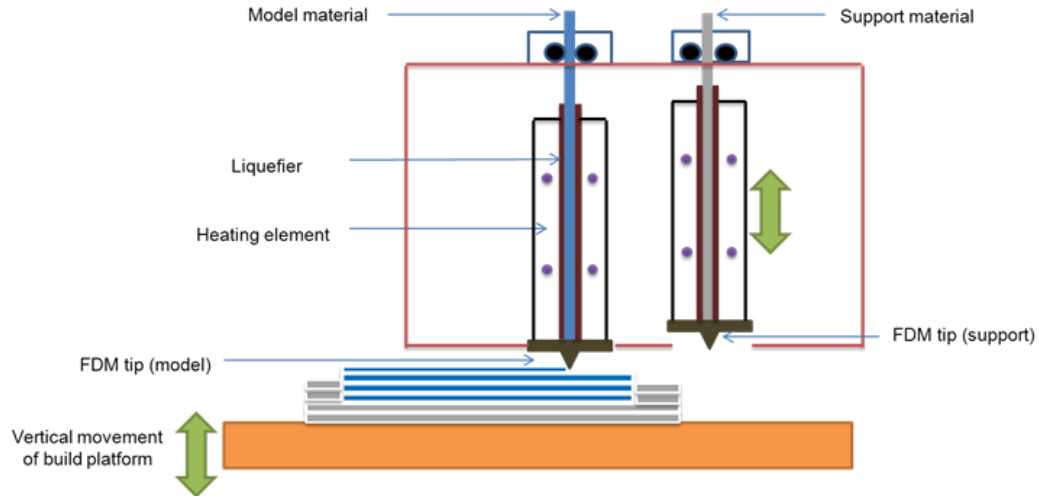


Figure 1.1: Schematic diagram of FDM Machine

be a revolutionary step for FDM parts to be used in engineering applications (e.g., sprinkler, pressure tubes, home appliances, etc.).

1.2 Motivation

FDM systems may be capable of fabricating parts with improved mechanical properties using suitable building parameters. As a result, FDM systems will be able to compete with conventional injection molding processes, when comparing mechanical properties, surface finish, and so on. In order to determine the usabilities of FDM parts in wire harnesses, switches, fuses, etc. inside the passenger compartment of an automotive car requires thermal cycle testing. A FDM as fabricated part capable of withstanding fluid pressure can lead to new engineering applications. Therefore, the research will explore three studies that performed to better understand FDM. The first study states that reduction or complete removal of gaps between two adjacent rasters, and between contour and rasters will improve mechanical properties of FDM parts. The second study states that FDM parts will be able to withstand the thermal cycling based on several criteria, including mechanical properties, glass transition temperature, and warping. The third study states that edge detection technique will be implemented for each layer of the part and a set of processing

parameters will be obtained that will create the smallest possible gap in each layer. The FDM fabricated part using those parameters will be able to hold fluid pressure.

1.3 Thesis Objective

The main objectives of this work are the following:

1. Modify processing parameters based on optical observation using microscopy to improve mechanical properties.
2. Experimentally determine the effect of thermal cycling on FDM fabricated parts.
3. Develop an edge detection technique to assess the gap between rasters and contours in each layer of the part.
4. Develop a method, which can predict a set of processing parameters for FDM fabricated parts which can hold fluid pressure.

1.4 Thesis Outline

The results from this study are described in the following four chapters. Chapter 2 is comprised of an overview of FDM technology as well as related topics including mechanical properties, thermal cycling properties, and fluid pressure application. The chapter specifically covers the FDM technology overview, material options and properties, effects of FDM parameter modification, material properties under thermal cycling, amorphous polymer, glass transition temperature, and conventional methods to seal FDM fabricated parts. In Chapter 3, the methods of 1) parameters modification, 2) thermal cycle testing, and 3) sealing FDM fabricated parts are described. This chapter also mentions the associated parameters that were used in fabricating the test specimens and briefly describes the sealing algorithm. The experiment results are discussed in Chapter 4. The results consist of 1) mechanical performance using parameter modification, 2) effect of thermal cycling on FDM fabricated parts, and 3) sealing of FDM fabricated parts using a sealing algorithm. Finally, a conclusion and recommendations for future work are provided in Chapter 5.

Chapter 2: Literature Review

2.1 Introduction

The Additive Manufacturing (AM) process is comprised of fabricating prototypes, end-use, or consumer level parts using CAD models in a layer by layer fashion without the need of any process planning (e.g., build sequence, arrangement of machining process). AM fabrication mainly consists of 8 steps, which are illustrated in Figure 2.1. According to ASTM standard F2792 [1], there are 7 AM process categories, 1) binder jetting, 2) directed energy deposition, 3) material extrusion, 4) material jetting, 5) powder bed fusion, 6) sheet lamination, and 7) vat photopolymerization. With a wide range of fabrication processes, AM processing has the option to use polymers, photoreactive resins, metals, ceramics, etc. The fabrication time may vary with the above mentioned AM processes, and processing parameters (such as, decreasing layer thickness may increase build time significantly depending on the model dimensions). Based on the final part condition, and application, AM parts may require some post processing (e.g., machining, sanding, painting, polishing, etc.).

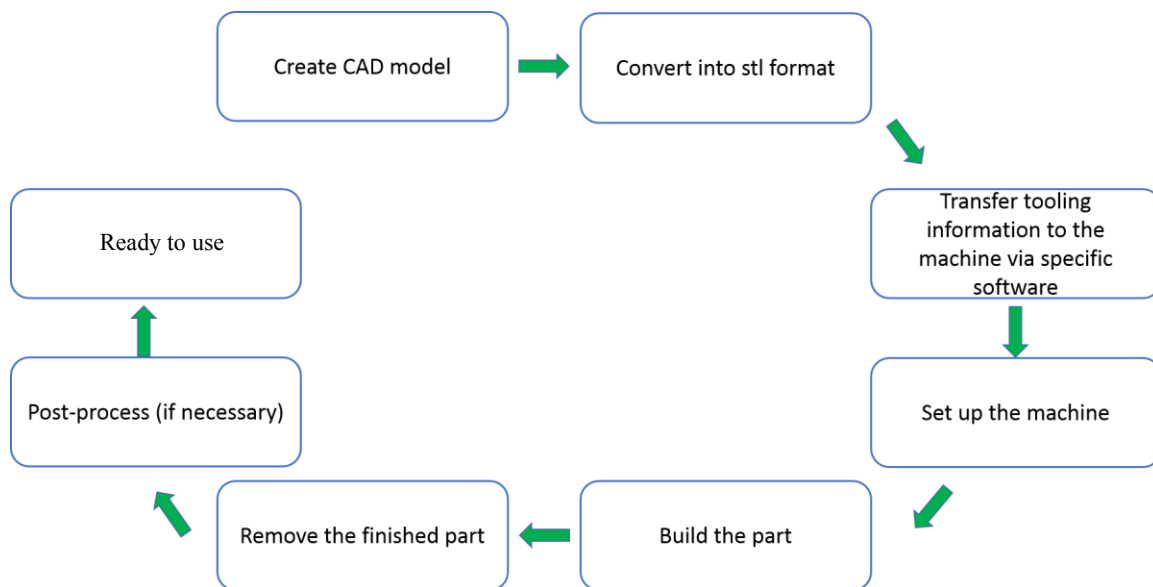


Figure 2.1: Generic AM Process

Previously, AM technology was mainly serving prototyping purposes. With continuous advancement, concentrating on mechanical properties, machine speed, and surface finish, AM has allowed the fabrication of rapid tooling parts, bio-medical scaffolds, metallic structures, complex shapes (foam like structures), and many more [4, 5].

2.2 Fused Deposition Modeling

The FDM technology was first patented by Scott Crump, founder of Stratasys Inc. (Stratasys Inc., Eden Prairie, MN), dates back to 1992 [6]. FDM machines were previously being used exclusively in prototyping applications such as concept modeling, pre-surgical models in medical applications, etc. [7]. The FDM technology is advancing to the capability of fabricating production grade end-use parts. The key factors (e.g., build size, material options, etc.) for production grade manufacturing has evolved tremendously (Table 2.1).

As mentioned earlier, FDM is a material extrusion based technology. As an extrusion based technology, it has several distinguished features, 1) loading of thermoplastic material, 2) liquification of extruding material, 3) push to drive (using a motor) thermoplastic spool, 4) depositing the material according to the machine instructions in a controlled speed, and 5) bonding

Table 2.1: Different FDM machine comparison [43] [44] [45]

Features	uPrint SE	FDM Titan	Fortus 900mc
Build Size	203×152×152 mm	406×355×406 mm	914×610×914 mm
Materials	ABSplus	ABS ABSi PC-ABS PC PC-ISO PPSF	ABS-M30 ABS-M30i ABSi ABS-ESD7 FDM Nylon 12 PC-ABS PC-ISO PC ULTEM 9085 PPSF
Layer thickness	0.254 mm	0.127 mm - 0.33 mm	0.178 mm-0.33 mm

of currently depositing material to the previous one [8]. The entire process of fabrication will be discussed in detail below.

The fabrication steps of FDM technology use three dimensional CAD data in order to create solid parts using a material extrusion process, which in most cases, does not require further machining. First, the three dimensional CAD model is created and converted into a .stl file format, which is then sent to a specific AM software package. For FDM machines, one of the software packages is Insight (Stratasys Inc., Eden Prairie, MN). Insight software slices the CAD model into layers and creates toolpaths based on user specified processing parameters. After receiving tooling instructions from Insight, the FDM machine drives the thermoplastic filament, driven from the filament spool, through the heated liquefier. In the liquefier, the thermoplastic material reaches a flowable state and is extruded through a small orifice extrusion tip. The tip, inserted in a head assembly, translates in the X and Y directions while thermoplastic material is being deposited over the build platform to create a layer. After finishing one layer, the build platform then moves down one layer height and the next layer is built over the previous one. This process keeps going until the entire model is done. To fabricate overhanging and complex features, a sacrificial support material is deposited along with the model material. The whole process is performed in a controlled envelope temperature which helps to improve bonding between layers and reduces internal stress [9, 10].

In the fabrication process, there are different parameters that can be changed. These parameters include build orientation, RA, RW, CW, RRAG, raster to contour air gap, slice height, and more. Build orientation refers to the orientation of the entire part in respect to the build platform in accordance with the ASTM F2921 standard (Appendix A Figure A1) [11]. The RA is the angle created by the raster with the positive X direction of the build platform. RW is the width of each raster, and CW is the width of the contour (Figure 2.2). RRAG is the gap between two rasters. Similarly, raster to contour air gap is the gap between the raster and contour. The default is 0 for both RRAG, and raster to contour air gap. A negative air gap leads to the partial overlap

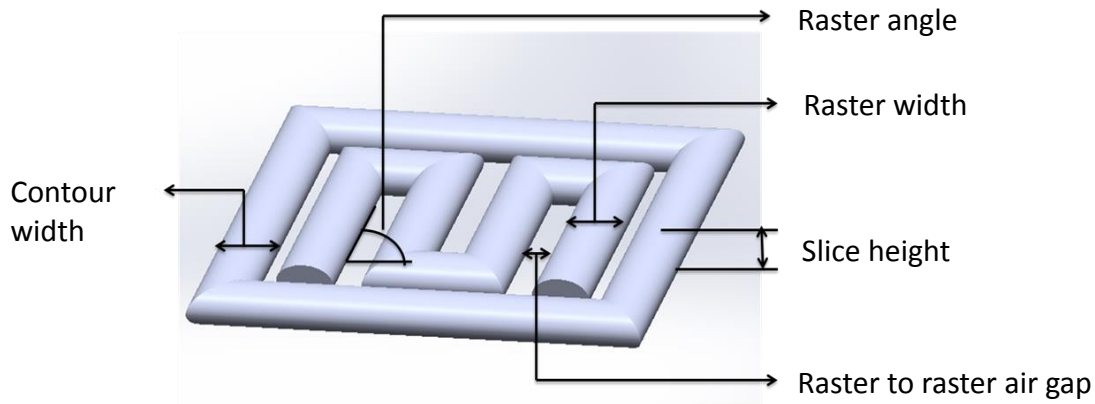


Figure 2.2: FDM building parameters

of the rasters (in case of RRAG) or between raster, and contour (in case of raster to contour air gap). Slice height is the height, or thickness of each layer.

2.3 FDM Material

Stratasys has made major contributions in respect to the variety of printable material types when compared with other FDM machines. A wide selection of commercially available materials (Table 2.2) with different inherent properties are now available, including acrylonitrile butadiene styrene (ABS), polycarbonate (PC), a PC-ABS blend, polyphenylsulfone (PPSF), ULTEM 9085, proprietary materials of Stratasys Inc. These materials fulfill commercial requirements as well as

Table 2.2: Selected properties of commercially available FDM materials [8, 42]

Property	ABS	PC	PC-ABS	ULTEM 9085	PPSF
Tensile Strength (MPa)	22	68	41	71.6	55
Tensile Modulus (MPa)	1,627	2300	1900	2200	2100
Elongation	6%	5%	6%	6%	3
Glass transition temperature ($^{\circ}\text{C}$)	104	161	125	186	230
Specific gravity	1.05	1.2	1.10	1.34	1.28
Thermal Expansion ($\text{mm}/\text{mm}/^{\circ}\text{C}$)	10.08×10^{-5}	6.84×10^{-5}	7.38×10^{-5}	6.6×10^{-5}	5.5×10^{-5}

specific applications for biocompatible applications [12]. The parts fabricated using FDM technology may exhibit lower strength when compared to the strength of the material itself because of interfacial bonding between the layers and possible voids between the rasters.

Some novel materials mentioned in literature that are also used for FDM fabrication include polymethylmethacrylate (PMMA) [13], polycaprolactone (PCL) [14], a composite consisting of glass, ceramic, or metal fillers [15], and metals such as eutectic Bi58Sn42 and non-eutectic Sn60Bi40 [16]. The different choice of materials for FDM systems is useful in respect to research as well as commercial use. The various material options can lead to numerous possibilities of different engineering applications, which can benefit AM technology.

2.4 Previous Works on Modifying Processing Parameters

FDM is a relatively new technology, dating back to 1990s. Since then, the evolution of FDM machine has undergone different processing parameter modifications, experimented by many researchers, which mainly focused on mechanical properties. Currently, numerous options for extrusion based AM machines exist, such as Fortus series (e.g., Fortus 900 mc, Fortus 400 mc), FDM series (e.g., FDM 3000, FDM Titan, etc.) and uPrint (Stratasys Inc., Eden Prairie, MN), Makerbot ReplicatorTM (MakerbotTM, Brooklyn, NY), and various other desktop models. Different processing parameters (e.g., build orientation, RA, CW, RW, RRAG, layer thickness, and more) are available based on each of these machines. Some software packages limit the user's access to build parameters, only providing build styles (e.g., sparse, double sparse, solid), which restricts the effort of further research with processing parameters. The processing parameters can be a key factor in the improvement of FDM system, particularly concentrating on mechanical properties.

Masood, Mau, and Song [17] experimented on polycarbonate (PC) FDM fabricated specimens and found a tensile strength of about 75% when compared with molded and extruded PC parts. The results showed that the UTS of PC was reduced about 8% and 13% due to the change of RAs from 45°/-45° to 90°/0° using RWs of 0.4064 mm and 0.6064 mm, respectively. An increase of about 18%, in UTS, was observed due to the change of RAs from 45°/-45° to 90°/0° using the RW

of 0.8314 mm. The results showed both increases, and decreases of UTS when changing the RAs using different RWs. The results also showed a non-linear trend of UTS for different RWs using the same RA. The non-linear behavior of UTS results were not addressed. Ahn *et al.* [18] worked on a similar experiment using ABS and found an increase in UTS, about 8%, due to the change of RA from 45°/-45° to 90°/0° using RWs of 0.508 mm and 1 mm, respectively. A negligible variation in UTS due to the change in RWs was mentioned. An increased build time and improved surface quality was addressed as well. Sood, Odhar, and Mahapatra [19] found a decrease of about 19% in UTS due to the change of RA from 60°/-30° to 90°/0° using ABS. The authors disputed that the higher RA creates smaller rasters, which can cause less distortion. However, it is worth noting that layer thickness was 0.1780 mm, and the specimens were inclined by 15° from XY plane rather than parallel to build platform. Montero *et al* [20] found UTS of axially build (0°) specimens was increased about 200%, compared to transversely build (90°) specimen.

In respect to the effect of RRAG, Ahn *et al* [18] found an increase in UTS for specimen built using a RRAG of -76.2 μm (-0.003 in), and found about a 30% increase for a RA of 0°/90° in comparison to a RRAG of 0 mm. Montero *et al* [20] also found an increase in UTS using a negative RRAG, for a transversely built specimen which was increased by approximately 400% using a RRAG of -50.8 μm compared to a RRAG of 0 mm. On the contrary, Sood *et al* [19] argued that a positive RRAG led the material to flow in between two adjacent layers, which in turn led to the increase of bonding between surfaces as well as UTS. An increase of about 15% in UTS was found for specimens built with a thinner layer of 0.127 mm. The UTS did not vary significantly for changing RRAGs for specimens built with a layer thickness of 0.254 mm. The cause of flow between layers is indistinct and may be a result from other factors, e.g., heat dissipation.

Bellini, and Güçeri [21] experimented on specimens built with ABS for mechanical properties of three build orientations: XYZ, XZY, and ZXY (build orientation terminology according to ASTM F2921 shown in Appendix A Figure A1) [11]. The highest UTS of 15.99 MPa, and Young's modulus of 1653 MPa was found for specimens built in XZY orientation. On the other hand, specimens built in ZXY orientation showed the lowest UTS of 7.60 MPa and Young's

Table 2.3: Anisotropic properties of FDM fabricated parts

Authors	Material	Criteria			
Bellini, and Güçeri [21]	ABS	Build orientation	XYZ	XZY	ZXY
		UTS	11.7 MPa	15.99 MPa	7.61 MPa
Masood, Mau and Song [17]	PC	Raster angle	45°/-45°	60°/-30°	90°/0°
		UTS	58.8 MPa	46.9 MPa	~50 MPa
Ahn <i>et al.</i> [18]	ABS	Raster angle	0°		90°
		UTS	~20 MPa		~4 MPa

modulus of 1391 MPa. The overview of anisotropic properties of FDM fabricated parts can be shown in Table 2.3.

The aforementioned studies showed the variation of the results using different building parameters (e.g. RA, RW, RRAG, layer thickness, build orientation, etc.). The reasons of the increase or decrease in mechanical properties, in some cases, were discussed. Research has shown that FDM fabricated part fall behind in UTS compared to what an injection molded part can withstand [18]. A method to increase the mechanical properties of a FDM fabricated part can be useful from the point of view of engineering applications that require specific performance criteria. Furthermore, a comprehensive data set using legacy and state of the art facilities can help document the mechanical properties from various FDM systems [18].

2.5 Thermal Cycling

The use of thermoplastic material in different aspects of the aerospace industries and automobile industries urges the importance of final parts usability in harsh environments. As a certification of feasibility for industrial purposes, determining the survivability of FDM fabricated parts in thermally harsh conditions can be of great benefit. FDM fabricated parts can be a great choice for embedding options of different components for electro-mechanical systems [22]. A comparative idea of thermal operations required in an automotive system is shown in Table 2.4.

Table 2.4: Operation temperature of automotive electronic systems [47] [48]

ECU Location	Detail Position	Required Operation Temperature
Passenger Room	Under dash board	-30 to +85 ⁰ C
Engine Room	ECU box	-30 to +105 ⁰ C
	Under hood	-30 to +125(150) ⁰ C
	Connected to Engine	-30 to >+175 ⁰ C

The engineering applications of 3D printed parts in electric wiring, embedded electric components are of great interest. Obviously, the main challenge is the longevity of FDM fabricated part in thermal cycling. There is the possibility of thermal shock, thermal fatigue stress that may be a potential hindrance in engineering application.

The thermal cycling effect was mainly studied on the polymeric composites. The polymeric composites show different expansion and contraction under thermal cycling which can ultimately cause thermal stress. The study of Shimokawa *et al.* [23] found micro-cracking in thermoplastic-polyimide matrix composites, IM7/PIXA and IM7/K3B, and micro-cracks were found after 10 cycles, and 5000 cycles respectively. In bismaleimide matrix composite, G40-800/5260, the micro-cracks initiated at 1000 cycles. The thermal cycle consisted of a maximum temperature of +177° C, and a minimum temperature of -54° C with a holding time of 15 min. The study indicated that open hole compression strength did not degrade for either IM7/PIXA or IM7/K3B for up to 1000 cycles. For G40-800/5260, the open hole compression strength did not degrade up to 1000 cycles. Though, for all matrix composites, a considerable micro-crack was found. The study conducted by Chung *et al.* [24] found a dramatic drop of glass transition temperature due to thermal cycling (80° C to 200° C) using carbon fiber reinforced epoxy composite (prepreg F593, rubber modified epoxy with T-300 carbon fibers). The rapid drop of glass transition temperature was found at the initial stages of the thermal cycles. A drop of glass transition temperature from 187° C to 167° C occurred after 7 hour for samples aged at 200° C. After the rapid drop, the glass transition temperature was found to be increased slightly in that same experiment. The initial drop of glass transition temperature was assumed to happen because of the degradation of the rubber modifier. The

additional crosslinking in the matrix resin material served to increase the glass transition temperature. An assumption was made that the depletion of rubber modifier might have caused the matrix to be brittle and increase the glass transition temperature.

From a practical point of view, the structure or material has to show good mechanical properties, and no polymer degradations. The thermal cycling study can lead to determine the possibility of use of the fabricated parts in engineering applications e.g., automotive industries, sprinkler systems, and even home appliances.

2.6 Amorphous Polymer

Thermoplastic polymers can be categorized as amorphous polymers, and crystalline (or semi-crystalline) polymers. PC is an amorphous polymer that is widely used in FDM technology. The amorphous polymer has a disordered polymer chain and does not show any crystalline X-ray diffraction pattern, does not have a melting transition temperature, and exhibits glassy and brittle behavior at low temperatures. As the temperature rises, they show a glass to rubbery transition which is referred as glass transition temperature (described in Section 2.7) [25]. Above the glass transition temperature, the amorphous polymer reaches a flowable state, although, the viscosity remains very high. On the other hand, crystalline polymers generally contain a significant amount of amorphous material, thus the semi-crystalline term is used. They show melting of crystalline domains, at the melting temperature (T_m), at which the Young's modulus is reduced tremendously. After that point, the behavior of semi-crystalline polymer is similar to the amorphous material [26].

The FDM technology best works with amorphous material. The viscous paste that forms right after glass transition temperature can be deposited in layer by layer fashion because of high viscosity of the polymer. The viscosity of the polymer decreases with the increase of temperature. The temperature that maintains the shape of extruding bead under pressure and solidifies quickly and easily, is appropriate for fabrication using FDM machine [8].

2.7 Glass Transition Temperature

The glass transition temperature is a phenomenon of amorphous polymers that occurs at a temperature when brittle and glassy characters transforms into a rubbery stage. At glass transition temperature the thermal expansion, heat capacity, and mechanical properties are changed. The glass transition temperature is a second order transition or glass transition that changes the rate of change of volume with temperature. The volumetric expansion α can be defined as:

$$\alpha = \frac{1}{V} \left(\frac{\partial V}{\partial T} \right)_P$$

Here, V is the volume. The rate of change is the volume of the temperature through glass transition temperature (Figure 2.3). The change usually occurs for a wide range of temperatures ranging from 10-30° C [25].

The glass transition temperature can be studied by change of volume with the increase of temperature using dilatometry method (Figure 2.3). Another method is the dynamic mechanical thermal analysis which is performed using a constant frequency of sinusoidal mechanical stress and changing the temperature at a constant rate. In this process, Young's modulus is measured at increasing temperature and a huge downfall in Young's modulus is observed around the glass

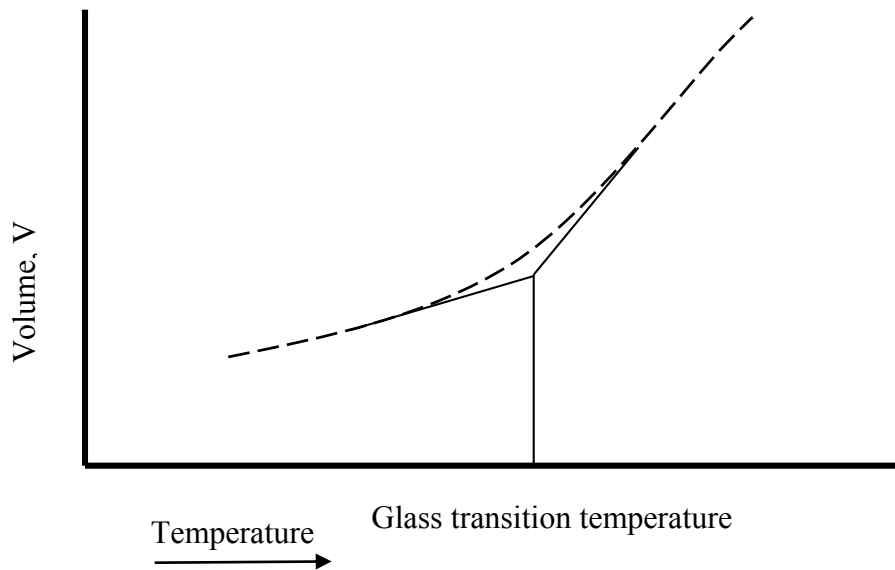


Figure 2.3: Variation of volume as a function of temperature for amorphous polymer

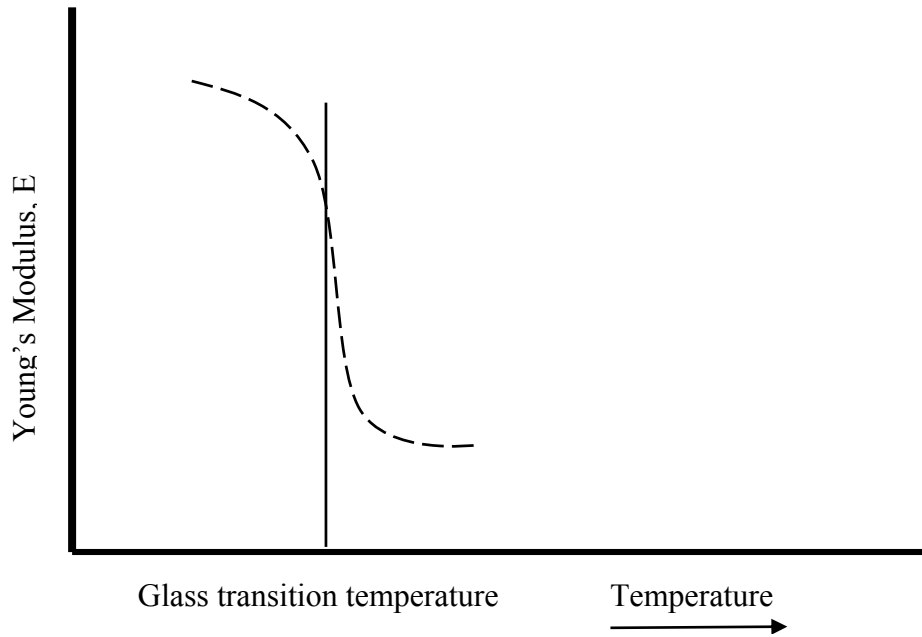


Figure 2.4: Change of Young's modulus against temperature showing the glass transition temperature of an amorphous polymer

transition temperature (Figure 2.4) [27]. The glass transition temperature indicates the transformation of thermoplastic material from glassy stage to rubbery stage transition. In the rubbery stage, the thermoplastic material changes into the high viscous flowable stage which is one of the most important criteria for FDM fabrication [8].

2.8 Previous Works on Sealing FDM Parts

Sealed FDM parts can be applicable in various applications, including sprinkler design [28], wind tunnel testing facility [29], enclosed biomedical devices (e.g., heart pace maker, defibrillator, etc.) [30], and polymer compact heat exchangers [31].

Prior works focused mostly on sealing FDM parts using different post processing methods. For example, brushing, vacuum infiltration, vapor smoothing, hipping, dipping, etc. The main objective of this study was to eliminate voids and improve the bonding between two adjacent layers. Mireles *et al.* [32] experimented on 11 different sealants using two methods: vacuum

infiltration, and brushing of sealant. The specimens were fabricated with ABS-M30, a proprietary material made by Stratasys. A maximum of 276 kPa pressure was applied using BJB TC-1614, a commercial sealant in comparison with 138 kPa pressure achieved using the vacuum infiltration method. The infiltration method and brushing method (using two coatings of sealant) showed an average dimensional change of 0.064 mm, and 0.0139 mm, respectively. Parker investigated the effect of hot isostatic pressing in FDM parts in order to eliminate voids. The results showed a 4.3% to 0.5% decrease of porosity using PC. The hot isostatic pressing caused a reduction of 0% to 35% in thickness. [33, 34]. Although, Parker did not perform any kind of pressure test, but the removal of porosity might lead to the possibility of sealing FDM parts.

The literature showed that post processing can improve FDM parts through removing voids. Those post processes caused either a decrease or increase in dimensions. Some of the processes led to the use of manual intervention, which can lead to further imperfection in dimensional accuracies. Moreover, those sealing methods require extra processing time (e.g., post processing, curing, drying, etc.), as well as an increase in cost (e.g., sealant, vacuum chamber, etc.). FDM fabricated parts that can be used in fluid pressure applications without any post processing will be a great step forward for FDM technology.

CHAPTER 3: Materials and Methods

3.1 Thermoplastic Material: PC

PC is a commonly used material in FDM systems. Being an amorphous polymer makes PC an excellent choice for FDM systems. PC contains the carbonate group in its chemical structure (Figure 3.1). Its strong mechanical property and higher glass transition temperature (Table 2.2) makes PC fabricated parts usable in various applications including automotive [35], biomedical applications [12] and even household components. As mentioned earlier, FDM fabricated parts show anisotropic properties. A datasheet containing the effect of building parameters (e.g., build orientation, RA, RW, CW, and RRAG) can serve as a useful addition that may be referred to by the FDM user community. In this study, building parameter modifications were studied to get improved tensile properties using PC. A low level thermal cycling test was also performed to verify its survivability in a concentrated application (automotive wire harness system), which can also be an information source for other practical use in engineering applications. A sealing algorithm was developed to fabricate test specimens using PC which showed little to no gap in-between rasters and also between rasters and contours. The ultimate goal was to fabricate a sealed part using an FDM system. A sealing algorithm allows for an improved calibration method in different production grade FDM systems, which can achieve the goal of sealed FDM parts out of the machine. The pressure testing performed using PC could ensure the possibility of sealed parts using other materials available for FDM systems as well.

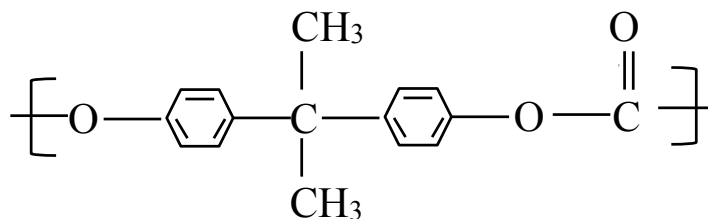


Figure 3.1: Chemical structures of PC

3.2 Fabrication of Specimens

3.2.1 Tensile test specimens for improving mechanical properties

The tensile test specimens were fabricated using the Fortus 900mc. The machine has a build chamber of 914 mm × 610 mm × 914 mm. The dimensional accuracy is of either ± 0.09 mm or 0.0015 mm/mm, based on larger value. The model, support and envelope temperatures were 345° C, 365° C and 140° C, respectively. As mentioned earlier, the specimens were built using PC, and PC support was used as a support material. Three build orientations were considered: XYZ, XZY and ZXY (Appendix A Figure A1). The ZXY specimens were built using surround support style (Appendix A Figure A2). In all other cases, a basic support style was chosen (basic support style commonly creates 5 layers of support at the base to hold the fabricated part in the platform). The surround support style was used to prevent the falling over or moving of the specimen during fabrication, due to the higher height to base ratio. The supports were removed manually from the finished specimens. The specimens were created according to the ASTM D638 Type I specimen (Appendix A Figure A3) [36]. The building parameters will be discussed in Section 3.3.

3.2.2 Thermal cycle testing Specimen

The thermal cycle testing specimens were fabricated using the FDM Titan (Stratasys Inc., Eden Prairie, MN). The machine has a build chamber of 406 mm × 355 mm × 406 mm, which is quite smaller than the Fortus 900mc. The model accuracy is ± 0.127 mm for model sizes up to 127 mm. For sizes greater than 127 mm, the accuracy is ± 0.0015 mm per mm. Two types of test specimens were built:

- a. Tensile test specimens
- b. Glass transition temperature measurement specimens

The tensile test specimens were fabricated according to ASTM D638 type I specimen (same as described in Section 3.2.1). The rectangular prisms with a dimension of 60 mm × 13 mm × 4 mm (Appendix A Figure A4) were fabricated to perform the dynamic mechanical analysis.

The specimens were fabricated using PC as model material, and PC support as a support material. The building parameters will be discussed in Section 3.6.

3.2.3 Pressure test specimens

The specimen was fabricated using the FDM Titan. Three type of specimens were fabricated:

- a. Flat plate
- b. Square feature
- c. Circular dome

The dimensions are shown in Appendix A (Figure A5-A7). PC was used to fabricate test specimens. PC support was used as a support material. The support was removed by breaking the supports manually. The building parameters will be discussed in Section 3.9.

3.3 Parameter Modifications for Improving Mechanical Properties

The parameter modifications were done using three successive methods. The three methods were:

- 1) Default method
- 2) Insight revision method
- 3) Visual feedback method

Each of the methods were tested for three different build orientations, XYZ, XZY, and ZXY (Appendix A Figure A1). Three different RAs ($0^\circ/90^\circ$, $30^\circ/-60^\circ$, and $45^\circ/-45^\circ$) were used to fabricate the specimens. The layer thickness was kept constant at 0.254 mm. The processing

parameters for the method are shown in Table 3.1. The detailed information concerning building parameters of the three methods are described in Sections 3.3.1, 3.3.2, and 3.3.3.

3.3.1 Default method

The default processing parameters were used in order to fabricate the tensile test specimens. The build parameters are shown in Table 3.2. The gap between rasters and contour was both observed in renderings created by Insight software, and optical images (Appendix B Figure B1-B3). For this reason, it is necessary to modify the building parameters.

3.3.2 Insight revision method

In the Insight revision method, the renderings of the job file created in the Insight software was analyzed. For a RA of 0°/90°, the CW and RW were changed from 0.4064 mm to 0.8128 mm in increments of 0.0254 mm using three build orientations. To give an idea, a total of 289 images

Table 3.1: Processing parameters used in improving mechanical testing

Machine used	Fortus 900mc
Model	
Material	PC
Extrusion tip	T16
Extrusion temperature	345 ⁰ C
Part interior style	Solid normal
Part RW	Described in Section 3.3.1-3.3.3
Part CW	Described in Section 3.3.1-3.3.3
Part RRAG	Default and Insight revision:0 mm, Visual feedback method: -0.0127 mm
No of Contours	1
Support	
Material	PC support
Extrusion tip	T16
Extrusion temperature	365 ⁰ C
Support style	Based on build orientation (Basic support for XYZ and XZY orientations, and Surround support for ZXY orientations)
Envelope	
Envelope temperature	140 ⁰ C

Table 3.2: Build parameters for default method

Build Orientations	RA	CW	RW	RRAG
XYZ	0°/90°	0.508	0.508	0
	30°/-60°	0.508	0.508	0
	45°/45°	0.508	0.508	0
XZY	0°/90°	0.508	0.508	0
	30°/-60°	0.508	0.508	0
	45°/45°	0.508	0.508	0
ZXY	0°/90°	0.508	0.508	0
	30°/-60°	0.508	0.508	0
	45°/45°	0.508	0.508	0

were analyzed for each different build orientation. The job file that rendered the smallest gap between rasters and contour using a RA of 0°/90° was selected as the building parameter among all the combinations of RWs, and CWs (Appendix B Figure B1-B3). Then, the same RWs and CWs were applied to both the 30°/-60° and 45°/-45° RAs (the building parameters are shown in Table 3.3). The reason behind choosing the 0°/90° RA as the modification foundation was because of the more distinguishable gap produced by the Insight renderings. The parameters (RW and CW combination) showed better results while changing the RAs. Each build orientation showed different sets of RW, and CW values, which showed renderings with less gaps. The reason for this

Table 3.3: Build parameters for Insight revision method

Build Orientations	RA	CW	RW	RRAG
XYZ	0°/90°	0.432	0.432	0
	30°/-60°	0.432	0.432	0
	45°/45°	0.432	0.432	0
XZY	0°/90°	0.508	0.483	0
	30°/-60°	0.508	0.483	0
	45°/45°	0.508	0.483	0
ZXY	0°/90°	0.559	0.457	0
	30°/-60°	0.559	0.457	0
	45°/45°	0.559	0.457	0

is that, with changing the build orientations, the planar area or surface covered by the FDM tip also changed. With different surface areas, different sets of parameters were needed.

3.3.3 Visual feedback method

In the visual feedback method, the specimens obtained from the Insight revision method were analyzed using a microscope. For this purpose, low magnification (32x) optical images were taken using a Retiga 2000R fast charge coupled device camera (QImaging, Surrey, Canada), which is installed in a Leica MZ16 stereomicroscope (Leica Microsystems, Wetzlar, Germany). For image analyzing, QCapture Pro (QImaging, Surrey, Canada) was used. Using a microscope, gaps between two adjacent rasters were identified despite the fact that those gaps were not depicted in Insight software renderings. A negative RRAG was introduced to remove those gaps. Five different RRAGs, in the range of -0.0025 mm to -0.0254 mm, were analyzed. Images showed little to no gap in between rasters using a RRAG of -0.013mm, and selected as a modified parameter. The building parameters are shown in Table 3.4. The only change from the Insight revision method was the addition of a RRAG of -0.013mm. The analysis of the images will be discussed in the Section 4.1.1.

Table 3.4: Build parameters for visual feedback method

Build Orientations	RA	CW	RW	RRAG
XYZ	0°/90°	0.432	0.432	-0.013
	30°/-60°	0.432	0.432	-0.013
	45°/45°	0.432	0.432	-0.013
XZY	0°/90°	0.508	0.483	-0.013
	30°/-60°	0.508	0.483	-0.013
	45°/45°	0.508	0.483	-0.013
ZXY	0°/90°	0.559	0.457	-0.013
	30°/-60°	0.559	0.457	-0.013
	45°/45°	0.559	0.457	-0.013

3.4 Mechanical Testing

Tensile testing was performed according to ASTM D638 standard using an Instron 5866 (Instron, Norwood, MA) tensile testing machine (Appendix C Figure C1). The tensile test was performed using a load cell of 10 kN which was sufficient for testing the low strength components. The machine's accuracy was $\pm 0.4\%$ according to the manufacturer's specifications. The prescribed ramp speed was 5mm/min during the tensile testing [36]. A video extensometer was used to capture the elongation of the specimen during testing. For that, two points at a distance equal to the gauge length was marked. The video extensometer locked into those two points before testing. The displacement of these two points was measured during testing to calculate the elongation. The tensile properties (e.g., UTS, Young's modulus, and tensile strain) were calculated by the built-in software, Bluehill (Instron, Norwood, MA). At least five specimens were tested for every set of parameters. The mechanical testing was performed after pre-conditioning of the specimen according to ASTM D618 standard (40 hours at 23°C and 50% relative humidity) [37].

3.5 Density Measurement Specimens using Parameter Modifications

The dogbone shaped specimens were fabricated using a RA of 0°/90° to measure density of the fabricated parts. The dimensions of the specimens are shown in Appendix C Figure C2. Three types of specimens were fabricated using three build methods default, Insight revision method, and visual feedback method, respectively. Three specimens were fabricated for each of the build methods. The processing parameters are the same as shown in Table 3.1. The build parameters are shown in Table 3.5. The building parameters were different because of the change in dimensions of the test specimens compared to tensile test specimens. The density was measured using two test

Table 3.5: Build parameters for density measurement specimens using three build methods

Method	RA	CW	RW	RRAG
Default	0°/90°	0.508	0.508	0
Insight revision method	0°/90°	0.457	0.5334	0
Visual feedback method	0°/90°	0.457	0.5334	-0.013

methods ASTM D1622 [38] and ASTM D792 [39]. The later method omits the manual measurements error which can occur using ASTM D1622 standard. The density according to ASTM D1622 was measured using the following equation:

$$\text{Density, } \rho = \frac{W}{V}$$

W = weight of the specimen in g

V = volume of the specimen in cm³

ρ = density in g/cm³

The specimens were preconditioned at 23° C and at 50% relative humidity for not less than 40 hours before weighing the specimens. The specimens were weighed using an analytical balance, CP124S (Sartorius Corporation, NY) and an ABSOLUTE Digimatic Caliper (Mitutoyo, IL) was used to measure the dimensions of the specimens to calculate the volume.

The density using displacement method according to ASTM D792 standard was measured using the following equation:

$$\text{Density, } \rho = \frac{a}{a+w-b} \times \text{density of water at temperature during the experiment}$$

a = apparent mass of the specimen in air

w = apparent mass of totally immersed sinker along with partially immersed wire

b = apparent mass of the specimen (with sinker) completely immersed in water along with partially immersed wire

The temperature of water during experiment was 25° C and therefore, density of water at that temperature (0.997 g/mm³) was used. The specimens were preconditioned according to the ASTM D618 standard (23° C and at 50% relative humidity for not less than 40 hours). The weighing was done using Sartorius M-prove scales (Sartorius Corporation, NY).

3.6 Processing Parameters of Specimens for Thermal Cycle Testing

Two types of specimens were fabricated for thermal cycling tests. As mentioned earlier, the tensile test specimens were fabricated according to ASTM D638 standard. Another set of specimens were built to measure the glass transition temperature. The tensile test specimens and

Table 3.6: Processing parameters used in thermal cycling test specimens

Machine used	FDM Titan
Model	
Material	PC
Extrusion tip	T16
Extrusion temperature	360 ⁰ C
Part interior style	Solid normal
RA	45 ⁰ /-45 ⁰
Part RW	0.508 mm
Part CW	0.508 mm
Part RRAG	0 mm
No of Contours	1
Support	
Material	PC support
Extrusion tip	T16
Extrusion temperature	365 ⁰ C
Support style	Basic support
Envelope	
Envelope temperature	145 ⁰ C

the glass transition temperature measurement specimens were fabricated using the same building parameters. All the default values recommended by the Insight software were used. The default values were used to investigate the behavior of the as-fabricated FDM parts (no parameter modification necessary) in engineering applications. The processing parameters are shown in Table 3.6.

3.7 Thermal Cycle Testing

After fabrication of the tensile testing parts and glass transition temperature measurement parts, both were pre-conditioned according to the ASTM D618 standard. After the pre-conditioning process, the height of two points at edges were measured for warping test (procedure will be described in Section 3.7.1 and test procedure is shown in Appendix C Figure C3-C4). The points were marked with a black circle in order to take the measurement at the same place after thermal cycling. A THERMOTRON (THERMOTRON, Holland, MI) machine was used to

perform the thermal cycling. An aluminum foil protective cover was used to prevent any kind of direct exposure to the thermal shock. A thermal feedback system was used in order to get temperature profile of the specimen. For that purpose, a thermocouple was inserted into a square shaped part that was fabricated using PC. The internal temperature of the specimens was monitored using that inserted thermocouple in the square shaped part (shown in Appendix C Figure C5) along with the temperature obtained from the in-built temperature sensor from the THERMOTRON system. The thermal cycle test conditions are described in Table 3.7.

A series of experiments (Section 3.7.1 - Section 3.7.3) were performed on the thermal cycled specimens (up to 150 cycles) to determine the properties of FDM parts after thermal cycling. The specimens were removed in every 20 cycles except when that batch ended in odd times (such as: middle of the night), in those cases the specimens were removed early or later (in this case, at cycle 18, cycle 41, etc.). So, after around 20 thermal cycles, 7 tensile test specimens and 5 glass transition temperature measurement specimens were taken out from the machine and conditioned for 40 h at 23° C, and 50% relative humidity before testing was performed.

3.7.1 Warping measurement

All the specimens were marked at the edges in order to take measurements at the same spot before and after thermal cycling using a touch probe type measure system, SmartScope Flash 250 (OGP Industries, NY) (Appendix C Figure C3). The tensile test specimen's thickness was

Table 3.7: Thermal cycling test parameters

Machine used	THERMOTRON
Parameters	
Temperature cycle	-30 ⁰ C – 85 ⁰ C
Temperature increase rate	1 ⁰ C/ min
Temperature decrease rate	1 ⁰ C/ min
Waiting temperature (at maximum, and minimum temperature	45 min
Total cycle time	320 min
Total number of cycle	150

measured using the touch probe, which touched at the edges of the specimen. The measurements were taken again after thermal cycling using the same procedure to measure the possible warping that might have occurred due to the thermal cycling.

3.7.2 Mechanical testing

The mechanical testing was performed using the same procedure described in Section 3.4. The mechanical testing was done for both non-cycled specimens and thermal cycled specimens.

3.7.3 Glass transition temperature measurement

The glass transition temperature measurements were done for both non-cycled, and thermal cycled specimens. The test was done using a dynamical mechanical analysis (DMA) instrument (model Q800, TA Instruments, Delaware) machine. The following test parameters were maintained: 0.01 N preload, 15 μm amplitude, 1 Hz frequency, and 2° C/min ramp rate. The glass transition temperature (Appendix C Figure C6) was measured using the plot of storage modulus with respect to temperature. The curve showed a sudden drop of storage modulus [39], and the intersection of the slopes of steady stage and rapid drop stage of storage modulus was marked as the glass transition temperature.

3.8 Sealing Algorithm

The algorithm was based on the basic idea of filling up each layer of the FDM fabricated part with rasters without having any gaps in between rasters and also between rasters and contours. The default value of RW, and CW is 0.508 mm, the distance perpendicular to the raster-raster direction must be a multiplication of 0.508 mm. Otherwise, a gap of less than 0.508 mm might occur in each layer. This process adds up in different layers of the FDM built part. The gaps are not only a source of crack initiation which can affect the mechanical properties (Section 4.1), but also a location where fluids can leak through. It is believed that these gaps are the reason FDM fabricated parts cannot be effectively sealed. To address the issue, a sealing algorithm was developed to suggest the best suitable RW in each layer of FDM fabricated parts. In this process, the CAD model was converted to .stl file format. The .stl file format was sliced into a layer height

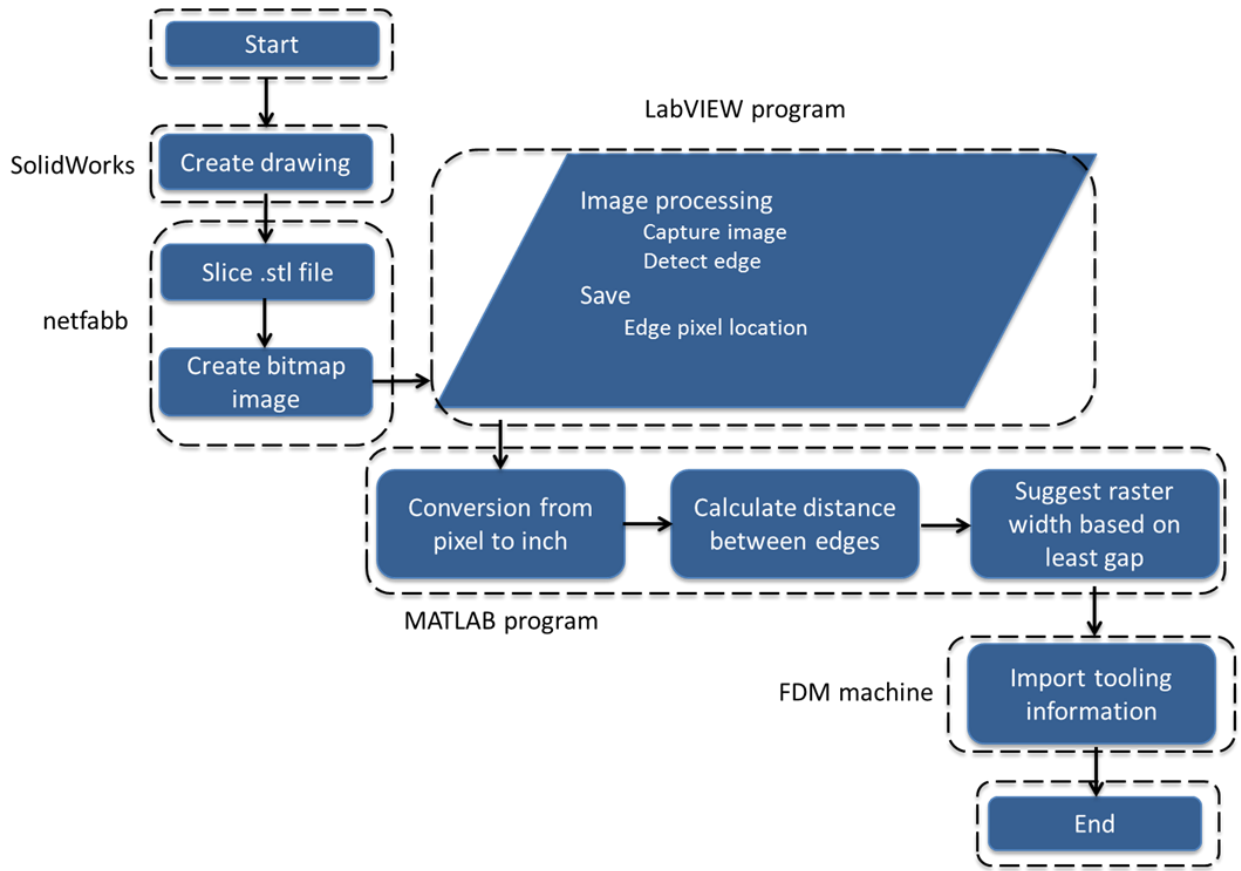


Figure 3.2: Process flow diagram of sealing algorithm

(slice height) of 0.254 mm (same slice height of FDM machine) using netfabb (netfabb GmbH, Lupburg, Germany). The bitmap images of every layer of the entire model were obtained using netfabb. A program was developed using LabVIEW (National Instruments, Austin, Texas) to gather the edge pixel locations of each layer from those bitmap images. The program wrote the edge pixel locations in a text file. The MATLAB code used the edge pixel location and determined the best value of RW using a series of calculations, which ultimately gave the least or no gap in a layer. After obtaining the build parameters, the job file was created using Insight software to export tooling information to the FDM machine. The process flow diagram is shown in Figure 3.2. More details of the algorithm are presented in Sections 3.8.1 – Section 3.8.6.

3.8.1 LabVIEW programming

After getting the bitmap image of each layer, the image was exported into a LabVIEW program to find the edge pixel location. The program scanned the entire image with a horizontal line travelling from the top most point of the bitmap image to the bottom. The program stored the edge pixel location through the entire scanning process. Based on the scan, the program returned the pixel location if it gained edge, or lost edge compared to the scanning of previous pixel (Figure 3.3). The process can be written as:

$A_{\mu+1} > A_{\mu}$; gained edge

$A_{\mu+1} < A_{\mu}$; lost edge

Here, A is the number of edges that were detected along a line in a pixel, and μ was the pixel number, starting from the top most point ($\mu=0$) to bottom ($\mu=n$). A NI vision assistant (National Instruments, Austin, Texas) was used to analyze the edge information. Based on getting edge or losing edge, the program returned the pixel number in a .dat file. Depending on total number of edges (R), a matrix of $R \times R$ was created in the .dat file. The pixel information was stored in such a way that $R_{i1} = R_{i2} = \dots = R_{in}$, (i , and n were positive integers, and n is the total edges found in the respective layer). So R_{i1} was defined as the pixel number of the corresponding edge of an image. This edge information is further analyzed using the MATLAB code.

3.8.2 MATLAB programming

In the MATLAB code, an input of tip number or size was necessary, which fixed the lowest and highest possible RW (based on the available RWs in Insight software) for the FDM fabrication. In the experiment, a tip of T16 was used, the RW started from 0.406 mm to 0.863 mm. The matrix information ($R \times R$) is also necessary to calculate the edge pixel location (mentioned in Section 3.8.1). The distance from the top most edge, R_{11} , to any other edge, R_{i1} was calculated by subtracting the corresponding pixel numbers. It is necessary to transfer the pixel number into inches (as FDM uses inches as the working dimension). The pixel to inch conversion will be described in Section 3.8.3. The conversion can be shown in this way,

$N_{i1} = R_{i1} \times \text{conversion variables for pixel to inches}$

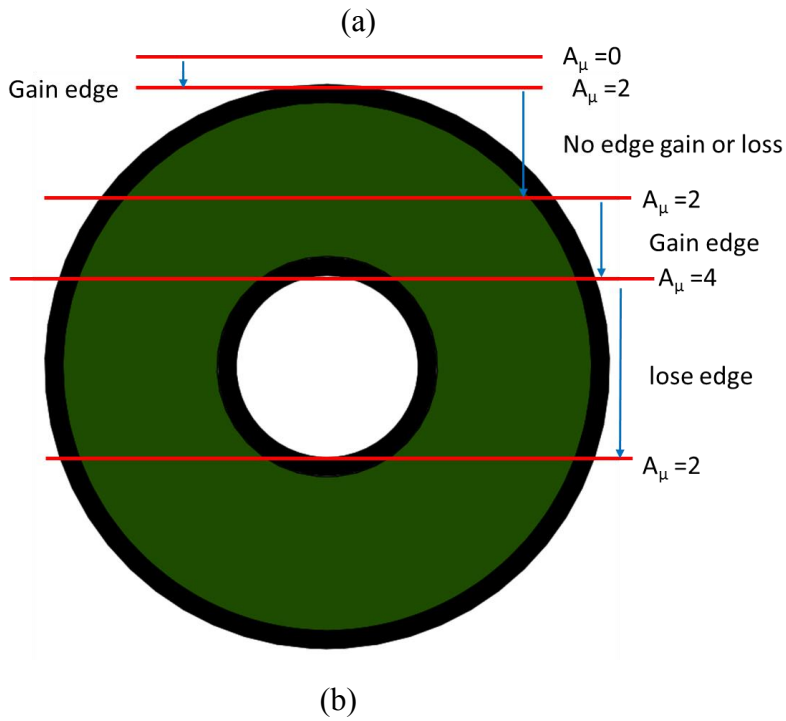
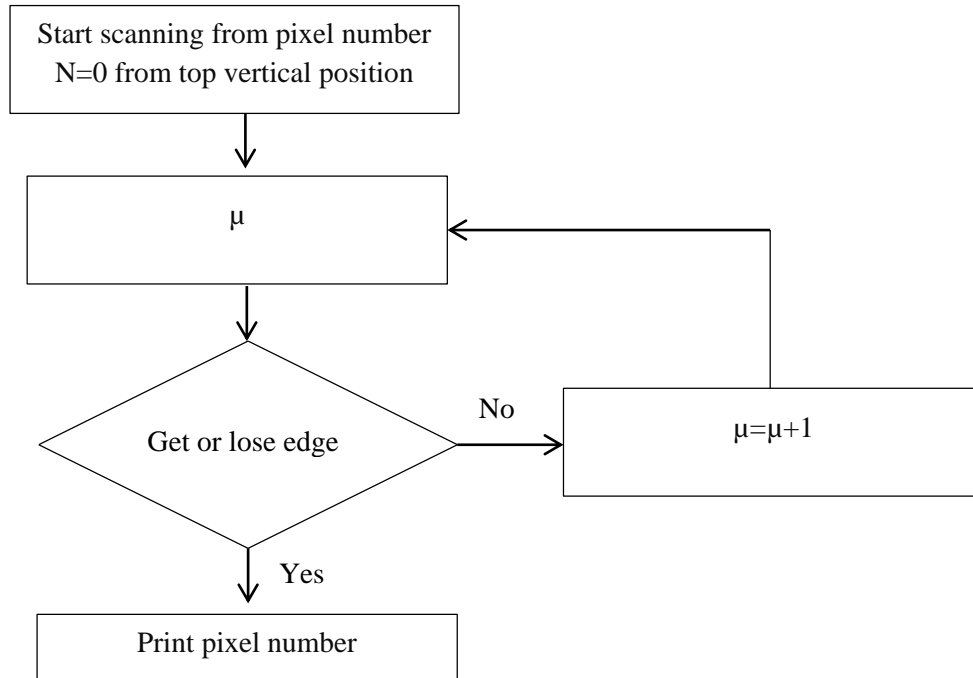


Figure 3.3: Edge pixel location based on gaining or losing edge (a) process flow diagram, and (b) schematic diagram.

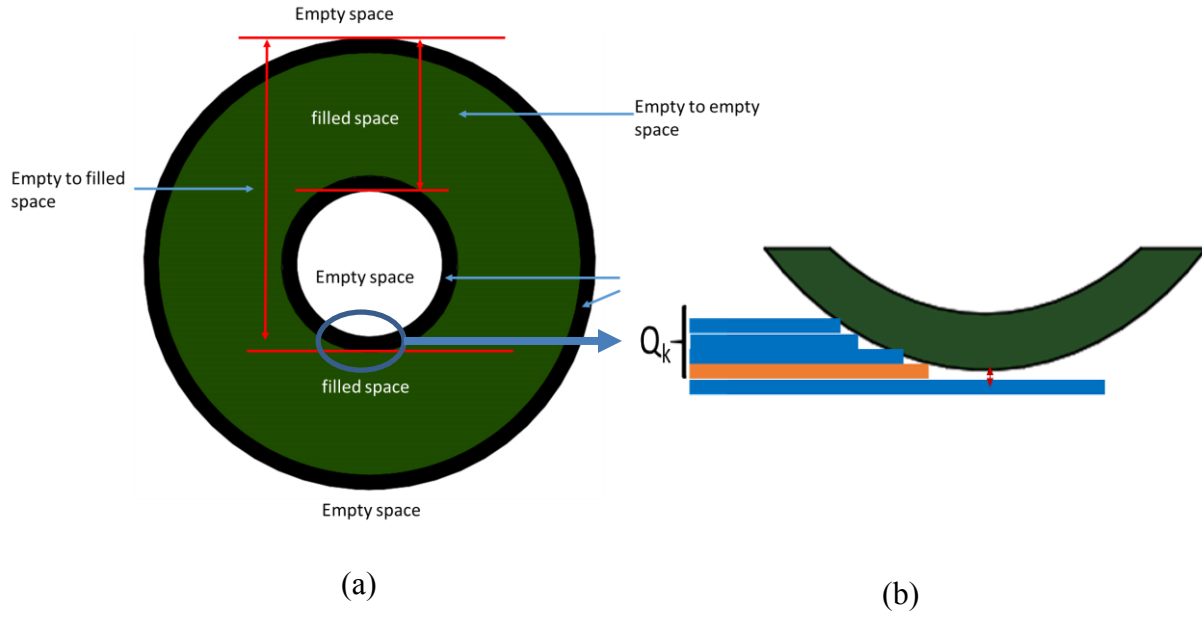


Figure 3.4: Edge calculation for number of contours (a) complete image of a layer (b) selected portion of the layer

As mentioned earlier, a constant CW of 0.508 mm was used for a total no. of 4 contours. The subtracting of total CW (number of contours \times CW) depended on whether the subtracting pixel numbers were between empty spaces, or from empty to filled space. In the Figure 3.4, it was evident that, in case of empty to empty space, a total of 8 contours (4 contours in each side) along with total RW were needed to fill the surface by rasters. On the other hand, in case of empty to filled space, the total surface filled, Y_i by rasters was just the difference of the converted pixel number into inches.

$$Y_i = (N_{i1} - N_{11}) - 2 \times \text{total CW (for case of in between empty space)}$$

$$Y_i = (N_{i1} - N_{11}) - \text{total CW} + \text{total CW} = (N_{i1} - N_{11}) \text{ (for case of empty space to filled)}$$

Here, Y_i is distance between edges considering contours and rasters.

The number of rasters (including fractional rasters) to the specific layer was calculated using following equation:

$$P_k = \frac{Y_i - \text{RRAG}}{\text{RW}_j - \text{RRAG}}; \text{ Here, } j, \text{ and } k \text{ are integers. } k = \text{total no. of edges in a layer (n)} - 1 \text{ (In case}$$

of Figure. 3.4(a) there are 4 edges). j represents the index of each RWs available in Insight.

The whole number of P_k was taken to calculate the raster number, Q_k .

Q_k = whole number of P_k (for case of in between empty space)

Q_k = whole number of $P_k + 1$ (for case of empty space to filled, an extra raster was added which is shown using orange colored raster in Figure 3.4.b)

The remainder was calculated using the following equations:

$$\text{Remainder, } T_k = (P_k \sim Q_k) \times (RW_j - RRAG)$$

A variable matching rasters with Insight software suggested number (described in Section 3.8.4) was taken into account based on remainder (T_k).

$$S_k = Q_k \pm \text{no. of raster due to raster variables}$$

The final remainder was calculated by the following equation,

$$F_k = (P_k \sim S_k) \times (RW_j - RRAG)$$

Total gap created between the rasters and contours was found by,

$$X_i = \sum F_k$$

The X_i is the summation of gaps found between the rasters and contours in a specific layer. The RW that provided least gap was selected as the desired RW for that layer. These calculations were applied in each layer of the CAD model, and found a set of suggestive RW (Appendix E Table 1-Table 2). The square feature and circular dome were fabricated using those RWs.

3.8.3 Variables for pixel to inch conversion

The pictures of each layer were taken with a resolution of 300 DPI. That way, conversion of pixel number to inches is achieved by multiplying pixel numbers by 1 over 300. The sealing algorithm showed a variable conversion coefficient when pixel values were converted into inches. This might happen because of an error (such as: round off error of the pixel number), associated with getting pixel information using the LabVIEW program. The roundness or curvature in the bitmap picture might be another reason behind variable conversion of the co-efficient. For this purpose, a set of square prisms (for square feature), and a set of cylinders (for circular dome) were used to determine the pixel to inch conversion. A set of features (shown in Figure 3.5) with a

dimension of 0.6 inch (10.16 mm) to 6 inch (152.4 mm) for Type I and II design, and 3 inch (76.2mm) for Type III and IV design, with an increase of 0.2 inch (5.08 mm) were drawn using SolidWorks (length for square prism, and diameter for cylinders). The edge pixel locations were obtained using LabVIEW program for the corresponding drawings. Now using this simple conversion co-efficient equation, the conversion co-efficient was determined,

$$\text{Conversion Co-efficient} = \frac{\text{dimension in inch (according to the SolidWorks drawing)}}{\text{Difference in Pixel (from LabVIEW program)}}$$

Four types of shapes were considered for conversion criteria. The shapes are shown in Figure 3.5. The different values of α were plotted against pixel number in Figure 3.6-Figure 3.8. Figure 3.6 shows the conversion co-efficient results considering Type I design for square feature. Figure 3.7 shows the conversion co-efficient results considering Type II design for circular dome.

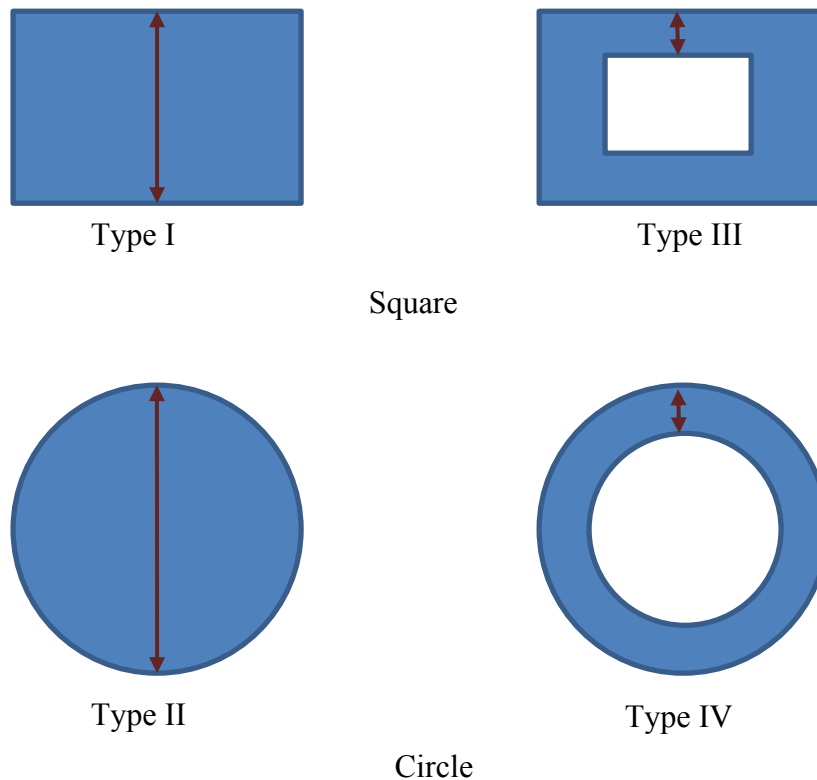
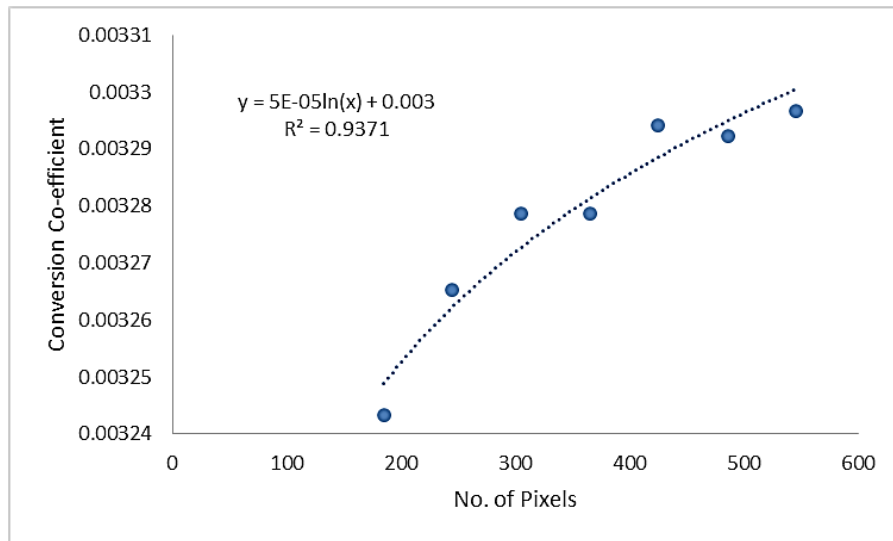
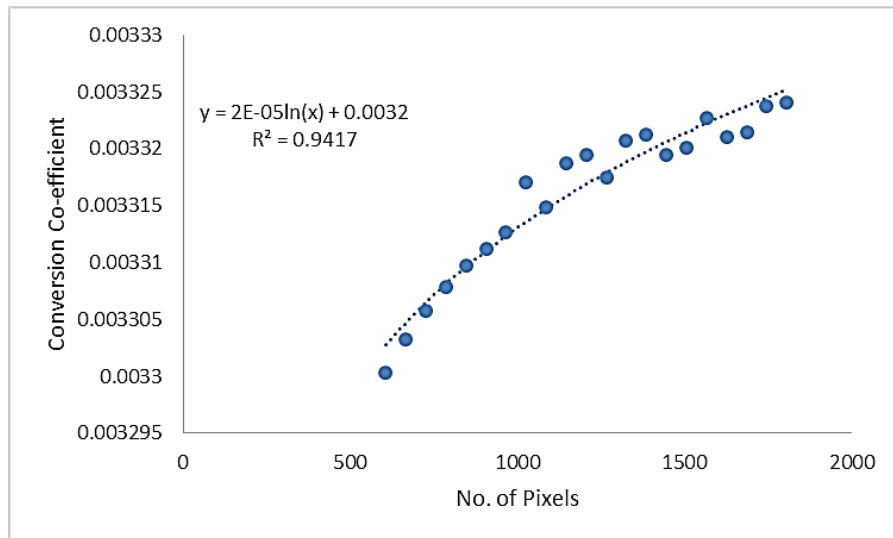


Figure 3.5: Schematic design consideration for conversion co-efficient measurements. The double sided arrow show the intended measurements that were taken into account

Finally, Figure 3.8 shows the conversion co-efficient of Type III and Type IV designs considering square feature and circular domes, respectively. A point worth noting, Type III and Type IV depicted same values for conversion co-efficient. The curves showed somewhat oscillating behavior, this could be due to low pixel resolution. It is anticipated, with the high resolution (such as: 1200 dpi or more), it can be fixed or at least minimized. The equations were obtained using



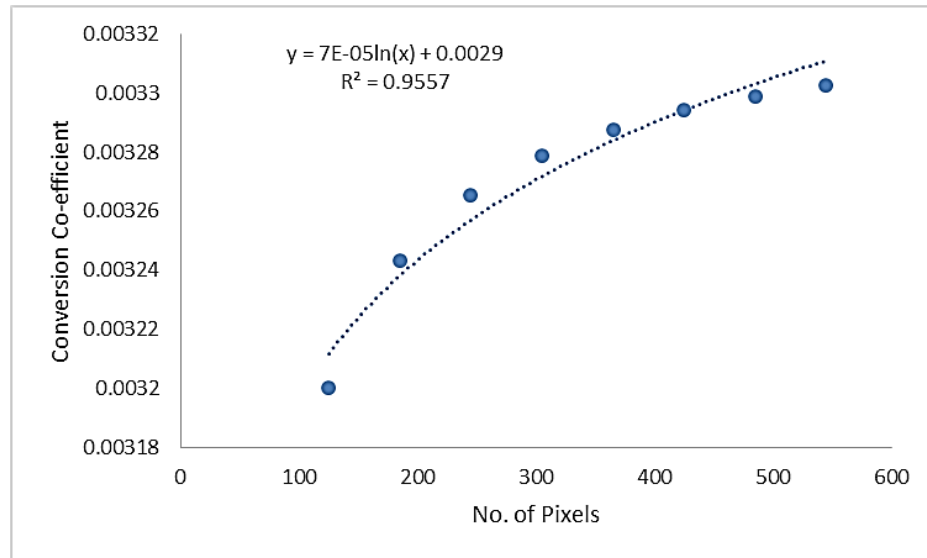
(a)



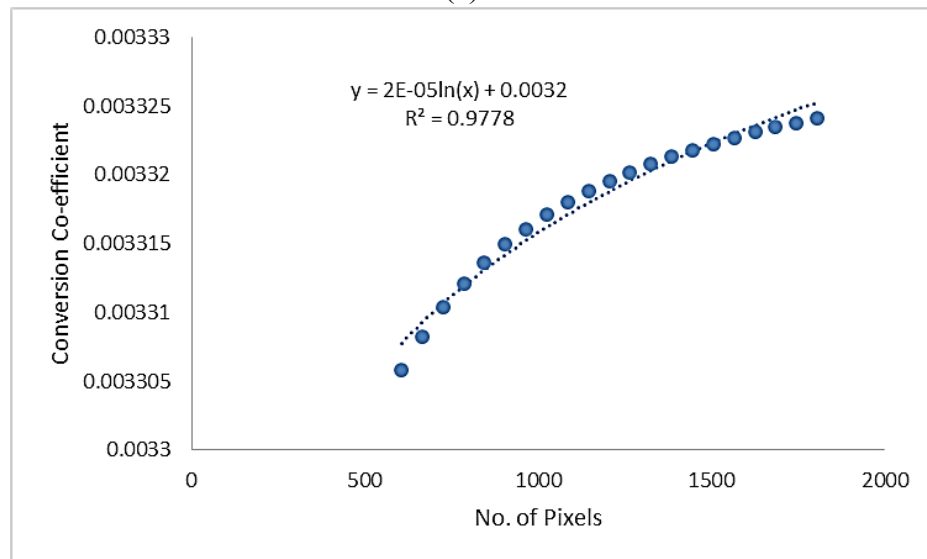
(b)

Figure 3.6: Pixel to inch conversion for square prism considering Type I design, (a) up to 600 pixel number and (b) over 600 pixel number. The equation of the curve is shown in the figure

trend lines (dotted line in Figure 3.6-3.8). These equations were used in MATLAB code to convert pixel values into inches values.

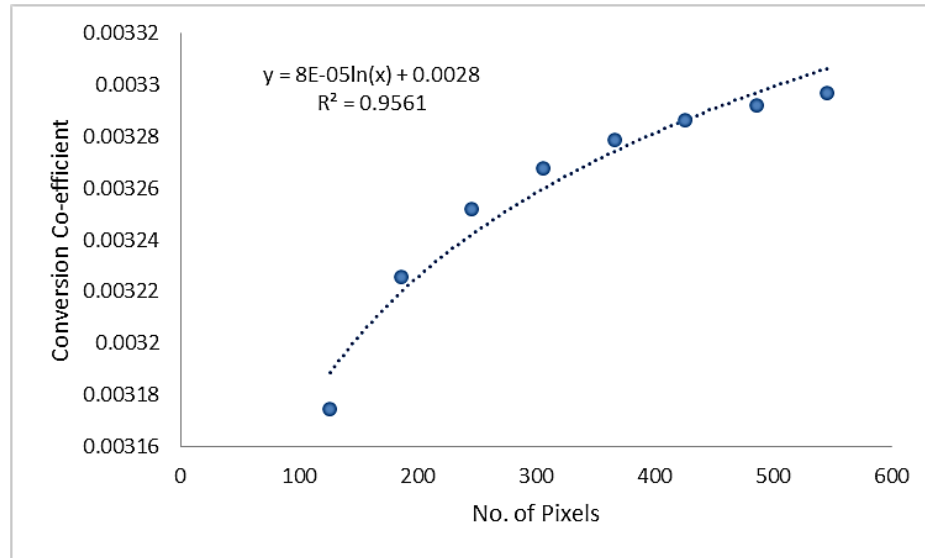


(a)

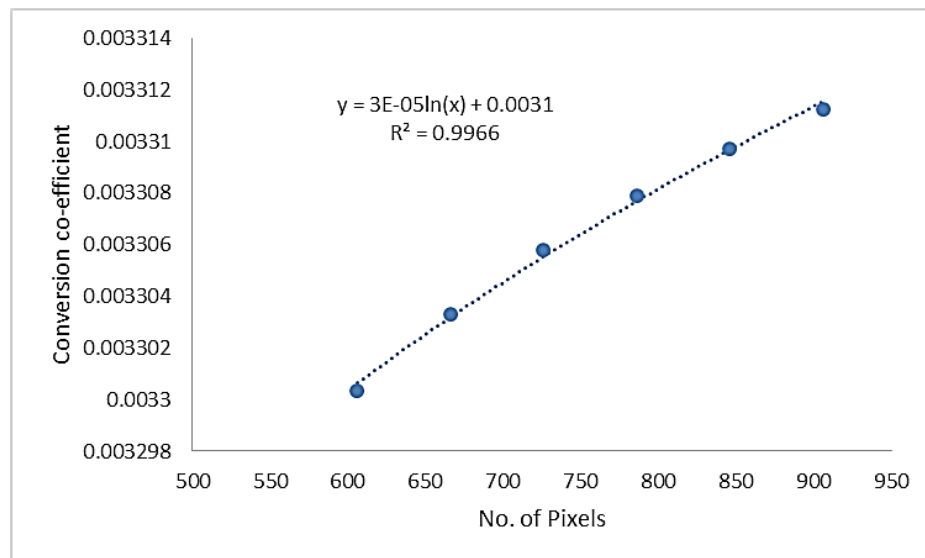


(b)

Figure 3.7: Pixel to inch conversion for circular dome considering Type II design, (a) up to 600 pixel number and (b) over 600 pixel number. The equation of the curve is shown in the figure



(a)

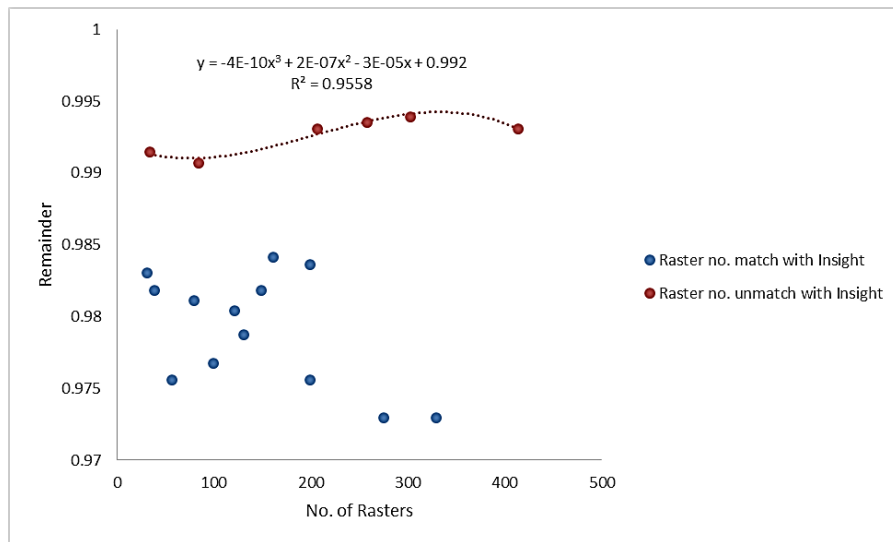


(b)

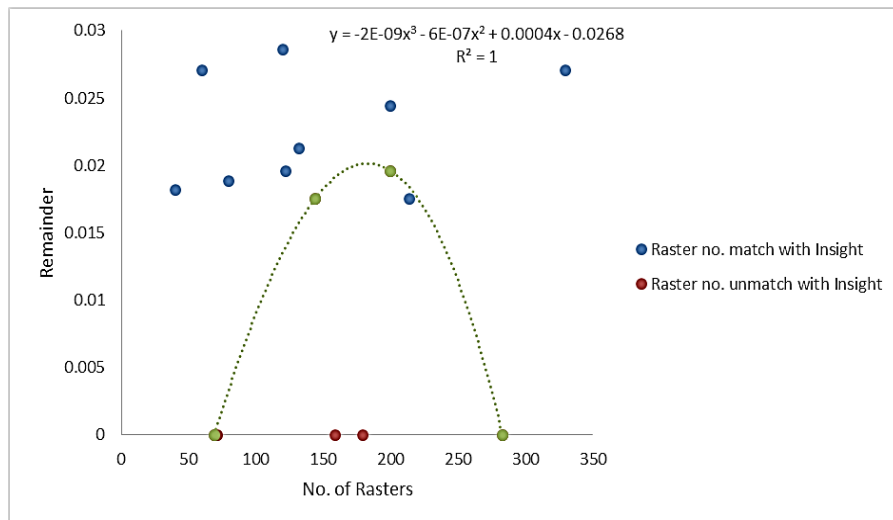
Figure 3.8: Pixel to inch conversion for both square feature and circular dome (both showed same result) considering Type III and Type IV design, respectively , (a) up to 600 pixel number and (b) over 600 pixel number. The equation of the curve is shown in the figure.

3.8.4 Variables for adding or deleting rasters

A series of square prisms similar to the Type I design (for square feature), and circular cylinders similar to Type II (for circular dome) from Figure 3.5, were drawn using SolidWorks. The .stl file was exported into the Insight software and checked for the total number of rasters. The total number of rasters in some cases were not matched with the raster number calculated using MATLAB code. The variation of the results (Figure 3.9) were found to be related with the



(a) Square feature



(b) Circular dome

Figure 3.9: Adding or deleting rasters based on features. A dotted curve was created using unmatching raster numbers with Insight and the equation of the curve is shown in the figure.

remainder of the raster number. The remainder was calculated by the difference of Q_k and P_k . A plot (shown in Figure 3.9) was developed which represent the fraction of RW that needs to be round up to the next number (in case of square dome) to add a raster, or round down to the previous number to delete a raster (in case of circular cylinder) in the calculation. As a result, the final suggestive raster number (S_k) matched with the raster number represented by Insight. The equation was developed using the remainder of unmatching rasters (where number of rasters in Insight does not match with S_k). For example, in case of square feature, if the MATLAB code calculated $P_k = 75.95$, and Insight used 75 rasters, it was considered as a match and was plotted as a blue dots. On the other hand, if Insight used 76 rasters (round up), it was considered as unmatched and was plotted using red dots with the trend line shown as a dotted red line (Figure 3.9 (a)). In case of circular dome, if the MATLAB code calculated $P_k = 75.10$ and Insight used 75 rasters, it was considered to match and was plotted as blue dots. On the other hand, if Insight used 74 rasters (round down), it was considered as unmatched and was plotted using red dots. In the case of circular dome, the peak numbers were selected (green dots) and a trend line was obtained (dotted green lines) and shown in Figure 3.9 (b). This analysis was used to determine when to round up or round down.

3.8.5 Limiting raster width

In the sealing algorithm the raster width used was limited to the range 0.41 mm to 0.64 mm. The 0.41 mm is the lowest possible RW using tip T16. The reason behind using 0.64 mm as the highest limit was that the gap between rasters increased with increasing RW (result of

Table 3.8: Analysis of gaps between the rasters. At least five measurement were taken for each RW.

RW (mm)	Total gaps between rasters (μm)	Average gap (μm)	Standard deviation
0.41	19.92	3.98	0.59
0.64	17.47	3.49	0.41
0.81	26.41	5.28	0.63

measurement of gap shown in Table 3.8). Three specimens were built using RWs of 0.41 mm, 0.64 mm and 0.81 mm, respectively (shown in Appendix D Figure D1-D2). The RRAG was kept at 0 mm. The average gap in between the rasters was found to be about 30% higher using RW of 0.812 mm in comparison to RW of 0.406 mm. Removing large gaps (as those for the 0.81 mm) using a constant negative RRAG might not be a solution. That is why the RW was kept up to 0.64 mm, to maintain less gaps in-between the rasters. That way, the gaps were minimized or completely removed using a constant RRAG. Another point was that a larger gap was created between rasters and contours using higher RWs (optical picture shown in Figure 3.10). The higher RWs created

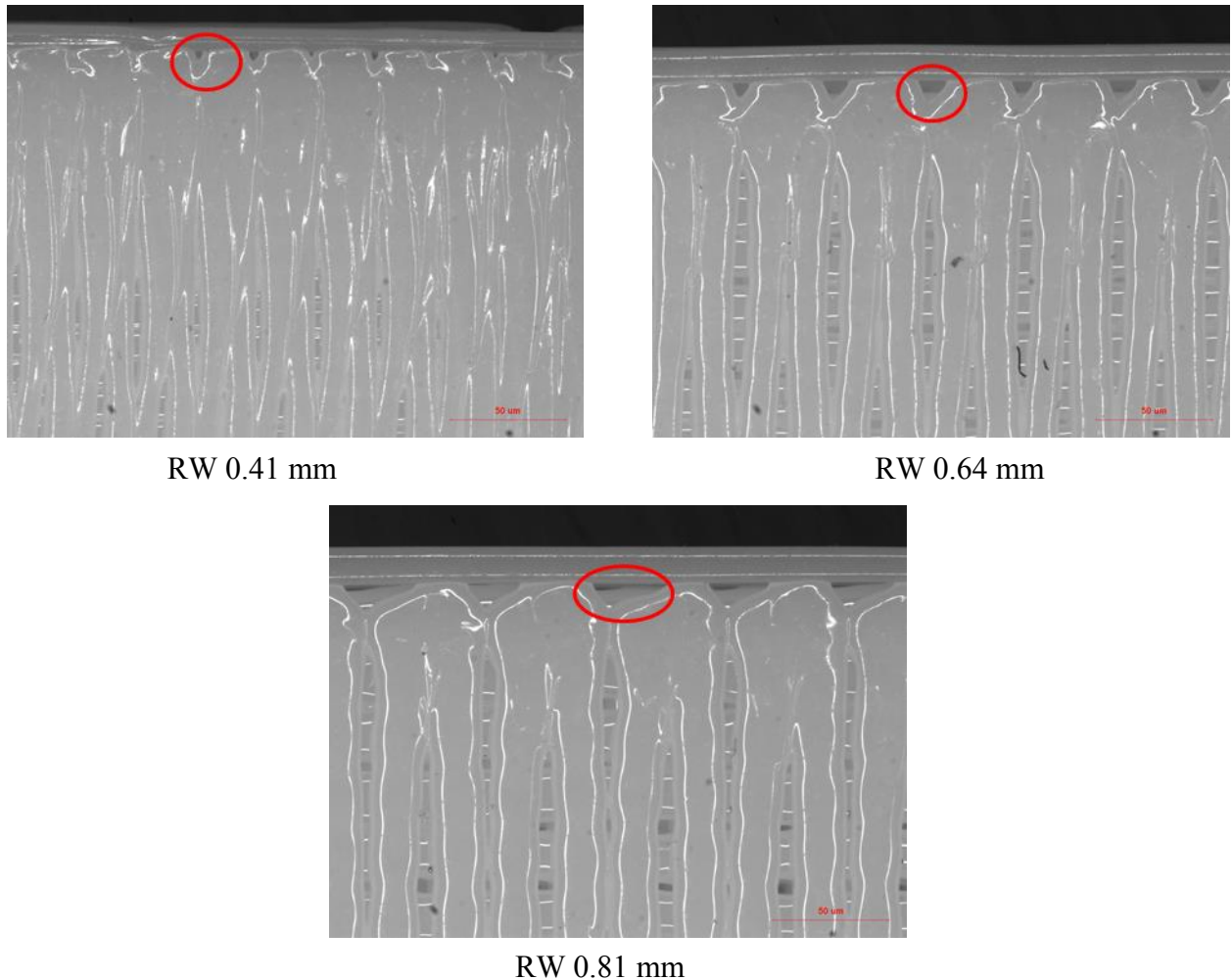


Figure 3.10: Deposition of raster showing gap at between raster and contour using three different RWs. Some gaps are highlighted in circle. The figures were taken using same magnification.

more gap during depositing rasters at the end of a raster whenever it starts to deposit another raster in the same layer. The effect might be referred to as cornering defect using FDM.

3.8.6 Selecting RRAG for sealing algorithm

A negative RRAG was used to remove the gap in-between rasters that was found in optical images (Appendix D Figure D3). A set of base plates of a circular dome was fabricated using three different RRAG (-0.0228 mm, -0.0304 mm, and -0.0381 mm) (Appendix D Figure D4). A RRAG of -0.0381 mm was used because it removed air gaps in between the rasters (Appendix D Figure D3) and did not affect planarization (i.e., the layer surface was still smooth so that subsequent deposition was not affected). With the increase in negative RRAG, the rasters become more congested due to the partial overlapping of adjacent rasters. At some point, the increase of RRAG created dislocated rasters, and resulted in a distorted surface at the top of the part. The surface roughness was increased by increasing the negative RRAG, which was a clear indication of distorted surface. The roughness value is shown in Table 3.9. The surface roughness was measured using a Mitutoyo SJ-201P surface roughness tester (Mitutoyo America Corp., Aurora, IL). The surface roughness results indicated that the higher roughness was obtained using higher negative RRAG. The RRAG of -0.0381 mm was chosen for the fabrication purpose. Though, the roughness value was still high, the optical image showed complete removal of air gaps in between rasters (appendix D Figure D3) and that is the main reason for selecting the RRAG of -0.0381 mm.

Table 3.9: Analysis of surface roughness. Five different surfaces were taken to measure the surface roughness value

Negative RRAG (mm)	Average Ra (μm)	Standard deviation
0.0228	66.38	0.78
0.0304	37.184	5.06
0.0381	123.6	14.50

3.9 Processing Parameter of Specimens for Pressure Test

3.9.1 Flat plate specimen

A flat plate was fabricated to see the feasibility of the FDM fabricated parts in pressure application. Processing parameters are shown in Table 3.10. PC was used to fabricate the part. The building parameters were selected using a successive process of obtaining a minimum gap using Insight software renderings. A negative RRAG was established based on a trial and error basis. A negative RRAG of 0.381 mm was used for the fabrication. This was possible due to the fact that each layer was the same in terms of geometry because there was no upper feature beyond the flat plate. It was observed that with additional feature of the design and with increased thickness, the part became more distorted. One of the reasons for the distortion of the part is due to the heat capacity of the thicker and larger part. The dimensions of the flat plate are shown in Appendix A Figure A5.

Table 3.10: Processing and building parameters used in pressure test specimens of flat plate

Machine used	FDM Titan
Model	
Material	PC
Extrusion tip	T16
Extrusion temperature	360 ⁰ C
Part interior style	Solid normal
RA	45 ⁰ /-45 ⁰
Part RW	0.457 mm
Part CW	0.457 mm
Part RRAG	-0.038 mm
No of Contours	1
Support	
Material	PC support
Extrusion tip	T16
Extrusion temperature	365 ⁰ C
Support style	Basic support
Envelope	
Envelope temperature	145 ⁰ C

3.9.2 Square feature specimen

A square feature (dimensions shown in Appendix A Figure A6) was fabricated using the building parameters shown in Table 3.11. The RWs (shown in Appendix E Table E1) were calculated using the algorithm described in Section 3.8. The RWs in the algorithm were based on the specimen's surface dimensions in the respective layer height. As a result, the RW varied along the specimen's height.

3.9.3 Circular dome specimen

The circular dome was fabricated using the same building parameters, and sealing algorithm as was mentioned in Section 3.8. Another specimen was fabricated using default

Table 3.11: Processing and building parameters used in pressure test specimens using sealing algorithm: square feature and circular dome

Machine used	FDM Titan
Model	
Material	PC
Extrusion tip	T16
Extrusion temperature	360 ⁰ C
Part interior style	Solid normal
RA	0 ⁰ /90 ⁰
Part RW	Based on test specimen and layer height (Appendix E)
Part CW	0.508 mm
Part RRAG	-0.038 mm
No of Contours	4
Contour style	Link contours
Support	
Material	PC support
Extrusion tip	T16
Extrusion temperature	365 ⁰ C
Support style	Basic support
Envelope	
Envelope temperature	145 ⁰ C

Table 3.12: Default processing and building parameters used in pressure test specimens and density measurement specimens

Machine used	FDM Titan
Model	
Material	PC
Extrusion tip	T16
Extrusion temperature	360 ⁰ C
Part interior style	Solid normal
RA	0 ⁰ /90 ⁰
Part RW	0.508 mm
Part CW	0.508 mm
Part RRAG	0 mm
No of Contours	1
Support	
Material	PC support
Extrusion tip	T16
Extrusion temperature	365 ⁰ C
Support style	Basic support
Envelope	
Envelope temperature	145 ⁰ C

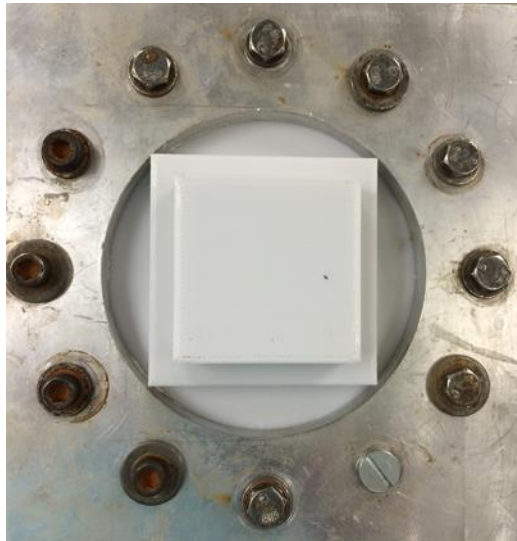
parameters (Table 3.12) to compare the as fabricated part with the part fabricated using sealing algorithm. The dimensions of the circular domes are shown in Appendix A Figure A7.

3.10 Density Measurement Specimens using Sealing Algorithm

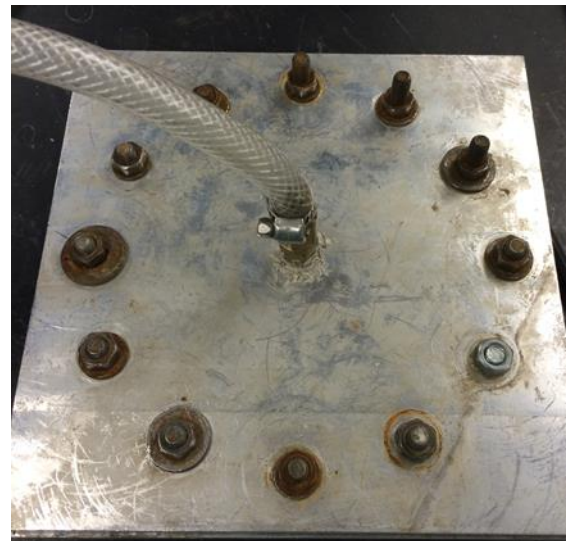
A cube was designed with dimensions of 25.4 mm × 25.4 mm × 25.4 mm according to ASTM D1622 standard [38]. Two types of samples were fabricated, 1) using the default parameters (Table 3.12), 2) using the sealing algorithm suggested parameters. In the case of sealing algorithm suggested parameters, all the processing parameters were the same as Table 3.11 except that the RW of 0.457 mm was used. Three specimens were fabricated using each build parameters. The density was measured using both methods described in Section 3.5. The specimens were conditioned at 23° C and at 50% relative humidity for not less than 40 hours prior to testing the specimens.

3.11 Pressure Testing

An aluminum test fixture was machined using a computer numerical control (CNC) system. In this case a HAAS mini mill 2 (Haas Automation Inc., California) was used. The test specimen was installed in a custom made text fixture (shown in Figure 3.11). The fixture had an air tube inserted at the bottom section of the setup. The test set up assembly was submerged in water. A compressed air source was attached to the air tube to supply high pressure inside the cavity (both square feature and circular dome). As a starting point, air pressure of 34.47 kPa (5 psi) was applied. After that, an increase of 34.5 kPa/min (5 psi/min) was maintained until the test failed. For safety concern, the maximum limit of pressure was set at 207 kPa (30 psi) so that any kind of catastrophic failure or explosion did not occur during the testing. The test failed condition was noted by leaking, in the form of air bubble formation due to the applied air pressure.



(a)



(b)

Figure 3.11: Pressure test (a) test specimen inserted in the fixture and (b) air pressure tube assembly at the back side.

CHAPTER 4: Results

4.1 Parameter Modification Results

4.1.1 Optical observation

The toolpath renderings generated by Insight and optical images of the actual material deposition is shown in Appendix B Figure B1-B3 (more optical observations are shown in Figure 4.1-4.3). As mentioned earlier, the gap between rasters and contour can be seen in the Insight software toolpath renderings. In Appendix B Figure B1, it can be seen that the gap between the rasters and contour are visible for XYZ build orientation. The gap between the rasters and contour were removed using the Insight revision method using modified build parameters of CW at 0.432

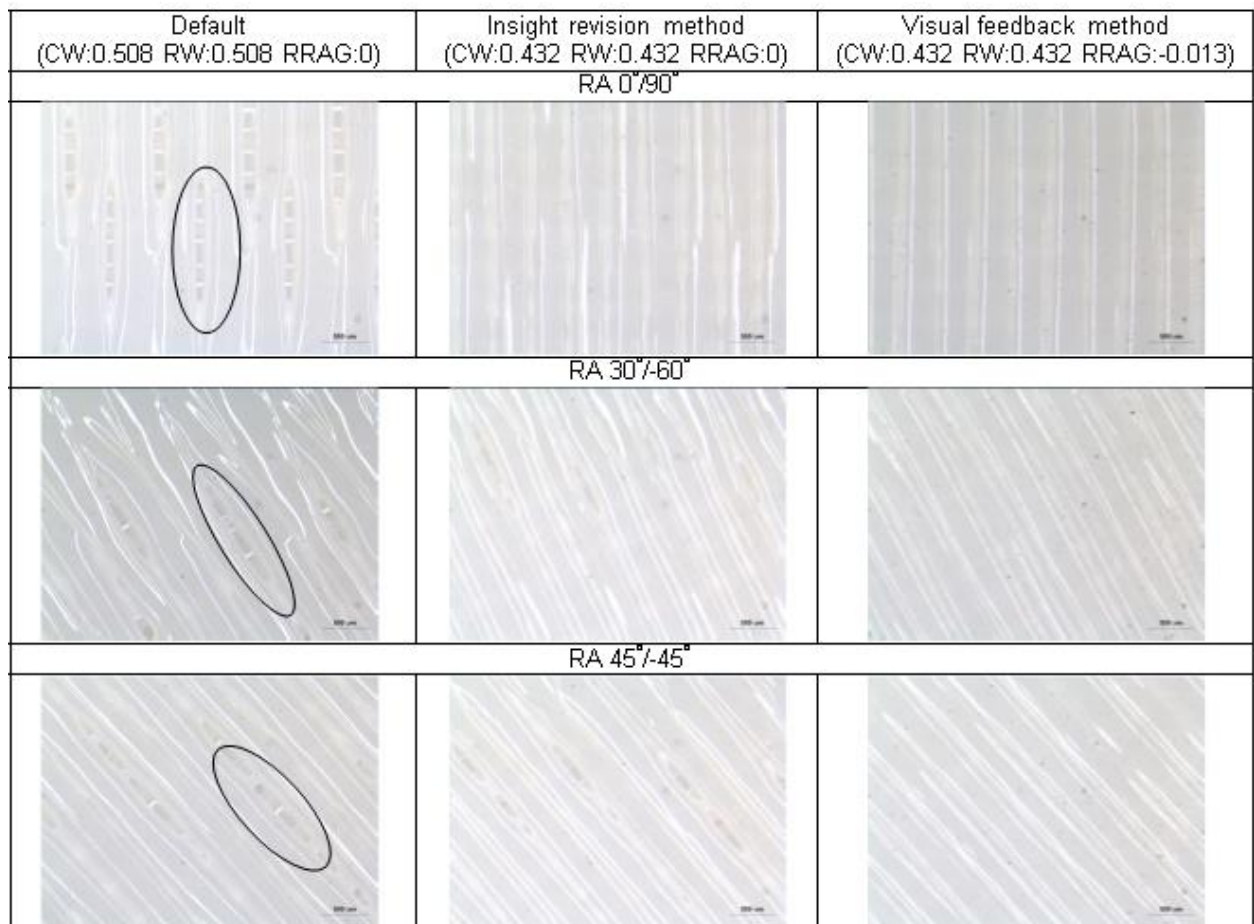


Figure 4.1: Optical images of specimens build in XYZ orientation with gaps shown by black circles (parameters are set in mm)



Figure 4.2: Optical images of specimens build in XZY orientation with gaps shown by black circles (parameters are set in mm)

mm, and RW at 0.432 mm. The same observation for the XZY, and ZXY build orientations was detected, from the point of view of the removal of gaps between the rasters and contour. Despite the removal of gaps in the Insight revision method, some gaps were observed in the optical observation. The gaps between the rasters were not depicted in Insight toolpath renderings. The more optical observations for three methods, 1) Default method, 2) Insight revision method, and 3) visual feedback method, are shown in Figure 4.1-4.3.

The optical observations for the XYZ build orientation using RAs of 0° / 90°, 30° / -60°, and 45° / -45° is shown in Figure 4.1. The default method (CW of 0.508 mm, RW of 0.508 mm, and RRAG of 0 mm) showed gap between the rasters. With the Insight revision method, using a decreased CW, and RW widths (CW of 0.432 mm, RW of 0.432 mm, and RRAG of 0 mm), the



Figure 4.3: Optical images of specimens build in ZXY orientation with gaps shown by black circles (parameters are set in mm)

gaps between the rasters were reduced. A RRAG of -0.013 mm was introduced in the visual feedback method to remove the gaps. The gaps between the rasters were completely removed using CW of 0.432 mm, RW of 0.432 mm, and RRAG of -0.013 mm for XYZ build orientation. The optical images for the XZY orientation are shown in Figure 4.2. The gaps between rasters, and contour were more visible for a RA of 0°/90°. The gaps were removed using the Insight revision method. However, the gaps were still visible for the other two RAs. The visual feedback method, showed similar gaps when compared with the Insight revision method. The optical view for the ZXY orientation is shown in Figure 4.3. The gaps between rasters, and contour are more visible

using default parameters. In this orientation, the FDM tip had to cover less geometric area, which created more congested rasters. This ultimately showed little to no gap in between rasters. The gaps between rasters, and contour were minimized using the Insight revision method. Gaps were also further minimized using the visual feedback method.

4.1.2 Mechanical testing result

The UTS results are shown in Figure 4.4 for the 3 build orientations (XYZ, XZY, and ZXY) and 3 different RAs ($0^\circ / 90^\circ$, $30^\circ / -60^\circ$, and $45^\circ / -45^\circ$). The highest increase in UTS was obtained using the visual feedback method, compared to the UTS obtained using default

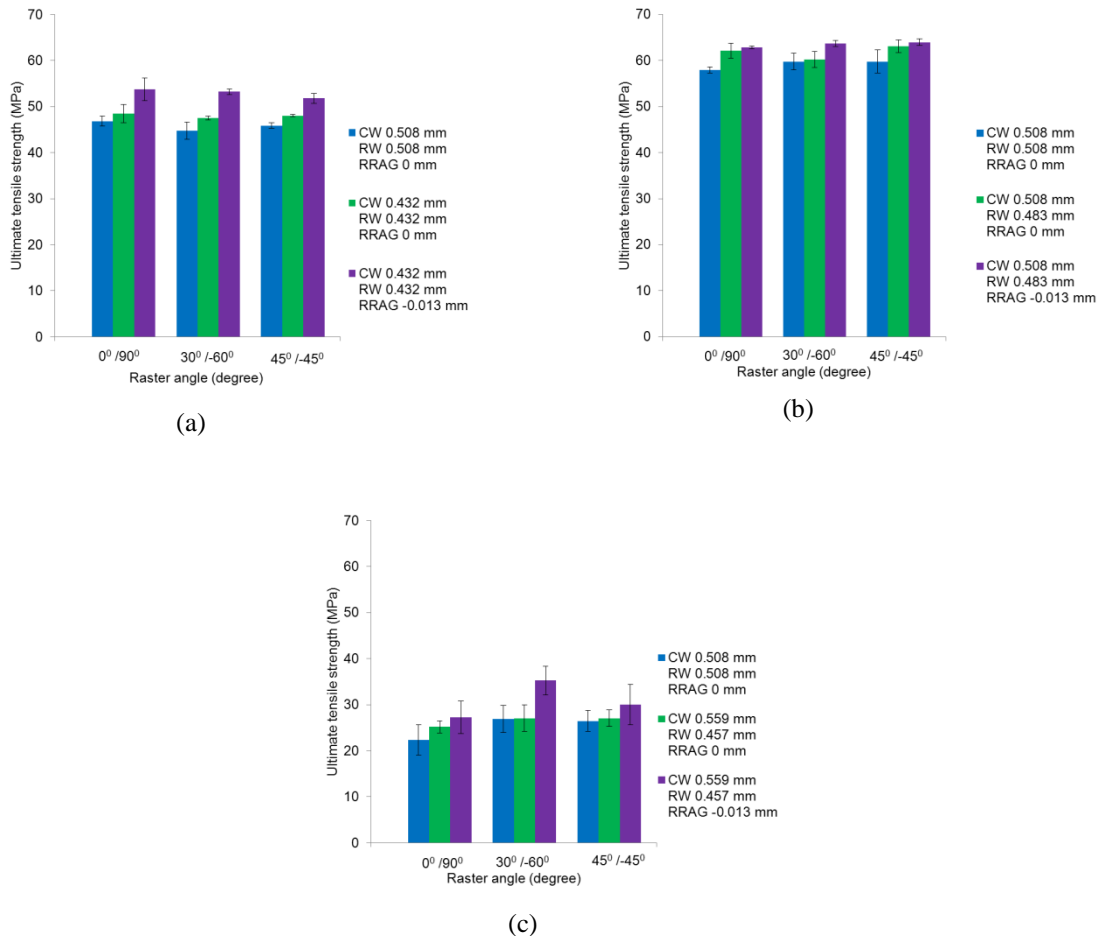


Figure 4.4: Ultimate tensile strength for a) XYZ build orientation b) XZY build orientation and c) ZXY build orientation. Each bar represents the average of at least 5 specimens and the error bars are +/- standard deviation

Table 4.1: Percentage UTS increase relative to UTS from default method

RA	Insight revision method	Visual feedback method
XYZ build orientation		
0°/90°	4%	15%
30°/-60°	6%	19%
45°/-45°	5%	13%
XZY build orientation		
0°/90°	7%	8%
30°/-60°	1%	7%
45°/-45°	6%	7%
ZXY build orientation		
0°/90°	13%	22%
30°/-60°	1%	31%
45°/-45°	2%	13%

parameters. The highest percent increase obtained in UTS was 19% (44.76 MPa to 53.22 MPa), in comparison to the results obtained using default parameters, for a RA of 30° / -60° and XYZ build orientation. The highest increase in UTS was obtained 8% (57.94 MPa to 62.84 MPa) in XZY, and 31% (26.87 MPa to 35.27 MPa) in ZXY build orientation using visual feedback method when comparing results obtained using the default method. The percent increase in UTS for the three methods are noted in Table 4.1.

The highest UTS was obtained for the specimen built in XZY orientation, and specimens built in ZXY orientation showed the lowest (Figure 4.4). The work performed by Bellini & Güceri [21] showed similar results with ABS and reported highest UTS achieved using the parts built in XZY orientation. The specimen built in XZY orientation has more contours deposited in the tensile loading direction. This might be one of the reasons for the increase in UTS using XZY orientation. The specimens built in ZXY orientation showed poor UTS and a highest UTS of 35.27 MPa was obtained, which was, around half of the UTS observed for the specimens built in the XZY orientation. In case of ZXY orientation, the layers were created in perpendicular orientation of the loading direction (Figure 4.5). As a result, the tensile strength obtained by the specimen built in

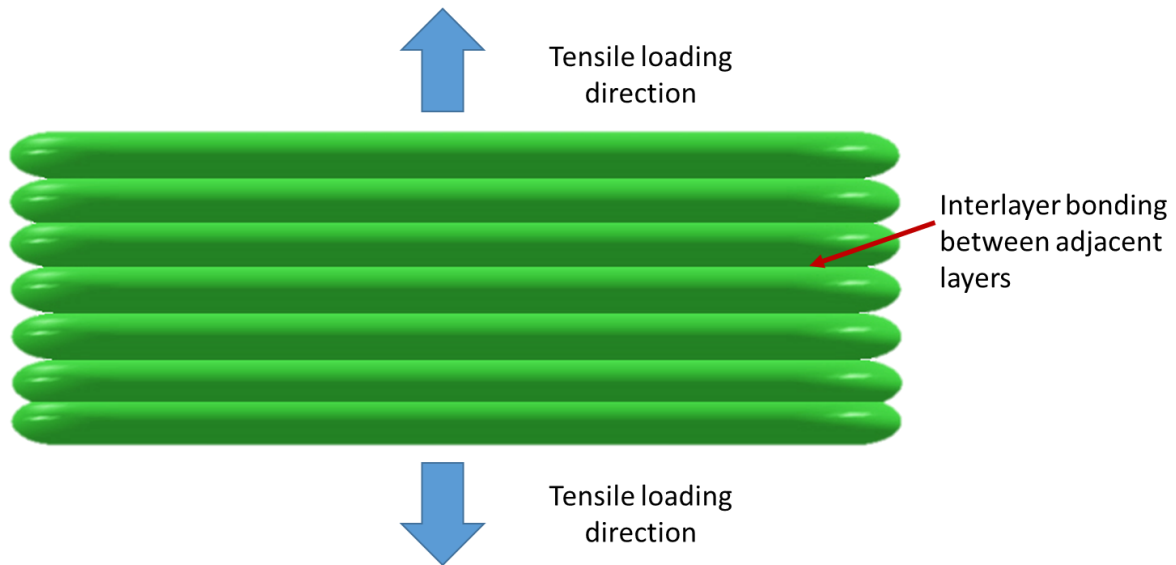


Figure 4.5: Schematic diagram of raster deposition in ZXY build orientation

ZXY orientation was mainly because of interlayer bonding. The interlayer bonding of FDM fabricated part is not as strong as the material itself which cause a decrease in UTS. In all the three build orientations, the highest UTS was obtained using a negative RRAG introduced into the visual feedback method. A negative RRAG causes a partial overlapping of the rasters, which in turn, removes the gap in between rasters (Figure 4.1-4.3). This may lead to the increase in UTS observed for all the three build orientations.

The t-test results (Table 4.2) showed that the results obtained using the default method, and visual feedback method were significantly different, at a 95% confidence level, or p value less than 0.05. The only exception was found for the specimen built in ZXY build orientation using the RA of $45^{\circ}/-45^{\circ}$. The reason is that the gaps between rasters and contour were not significantly removed, which can be seen in Figure 4.3 (for the specimens built in ZXY build orientation). The specimens built in the ZXY built orientation were surrounded by the support material during building, and also it shows a visible seam line, which altogether leads to a poorer surface finish (Appendix D Figure D5). That might cause high standard deviation in the results. The ANOVA test (Table 4.3) shows the results of UTS for different RAs. The results show that changing the RAs has no

Table 4.2: t-test results comparing UTS of default and visual feedback method

Build orientation	RA	Sample 1	Sample 2	t-statistical	t-critical	p-value
XYZ	0°/90°	Default	Visual feedback	5.11	1.85	4.5e-04
	30°/-60°	Default	Visual feedback	8.51	2.01	1.84e-04
	45°/-45°	Default	Visual feedback	9.65	1.85	5.5e-04
XZY	0°/90°	Default	Visual feedback	13.01	1.85	5.75e-07
	30°/-60°	Default	Visual feedback	4.10	2.01	0.004
	45°/-45°	Default	Visual feedback	3.22	2.01	0.011
ZXY	0°/90°	Default	Visual feedback	2.02	1.85	0.038
	30°/-60°	Default	Visual feedback	3.90	1.85	0.002
	45°/-45°	Default	Visual feedback	1.44	1.85	0.094

significant difference (p value greater than 0.5) in UTS using the same build method and the same build orientation. The only deviation in the results was found for the Insight revision method and visual feedback method using the ZXY orientation. The poorer surface finish, mentioned earlier, might be the reason for this exception (Appendix D Figure D5). In the experiment, the delta angle (subtraction of RAs between two adjacent layers) was kept constant at 90°. As a result, the directional effect created by one layer might be nullified by the adjacent layer. That might be the reason that there was no significant difference of UTS among the RAs. However, Masood *et al.*

Table 4.3: ANOVA table for UTS to compare results in 3 RAs for each method considering all three build orientations

Build orientation	RA	Sample 1	Sample 2	Sample 3	F-value	F-critical	p-value
XYZ	0°/90°	0°/90°	30°/-60°	45°/-45°	2.54	3.88	0.120
	30°/-60°	0°/90°	30°/-60°	45°/-45°	0.70	3.88	0.511
	45°/-45°	0°/90°	30°/-60°	45°/-45°	1.64	3.88	0.234
XZY	0°/90°	0°/90°	30°/-60°	45°/-45°	1.38	3.88	0.288
	30°/-60°	0°/90°	30°/-60°	45°/-45°	3.34	3.88	0.069
	45°/-45°	0°/90°	30°/-60°	45°/-45°	3.76	3.88	0.053
ZXY	0°/90°	0°/90°	30°/-60°	45°/-45°	3.06	3.88	0.083
	30°/-60°	0°/90°	30°/-60°	45°/-45°	5.89	3.88	0.016
	45°/-45°	0°/90°	30°/-60°	45°/-45°	4.72	3.88	0.030

[17] suggested otherwise, and mentioned that changes of RAs have an effect on UTS, either with an increase or decrease. However, statistical analysis was not performed with those results.

The result of Young's modulus is shown in Figure 4.6. The highest average value of Young's modulus was obtained 1816 MPa in the XYZ build orientation. This value was achieved for a RA of $0^\circ/90^\circ$ using the visual feedback method (in comparison with the 1595 MPa using default method). In the XZY orientation, the highest average value found was 1884 MPa for a RA of $45^\circ/-45^\circ$ using Insight revision method (1861 MPa was found using the default method). Finally, the highest average value obtained, in the ZXY build orientation, was 1847 MPa for a RA of $45^\circ/-45^\circ$ using the visual feedback method (1801 MPa was obtained using the default method). The

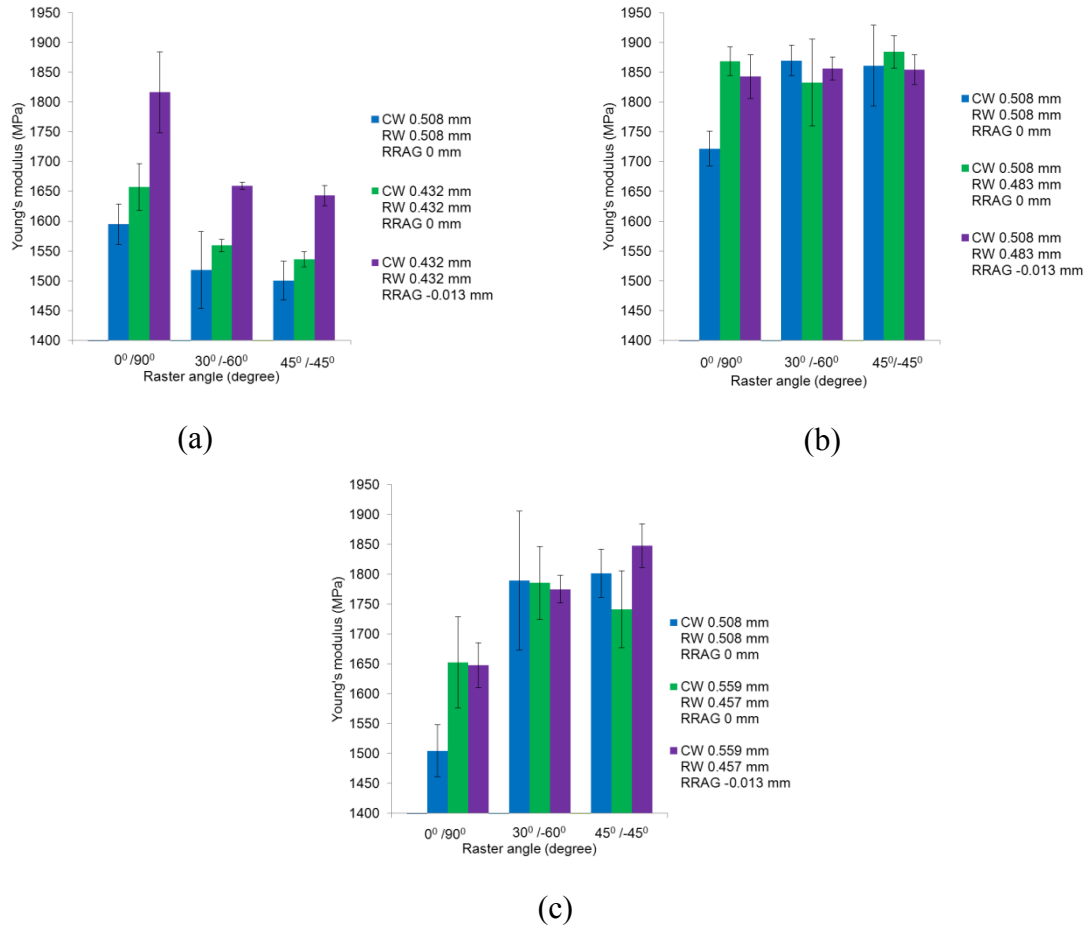


Figure 4.6: Young's modulus for a) XYZ build orientation, b) XZY build orientation and ZXY build orientation. Each bar represents the average of at least 5 specimens and the error bars are +/- standard deviation

optical image analysis led to a realization that the changes in Young's modulus might have a direct relation with air gap removal. For Example, Figure 4.1 shows a considerable removal of air gaps between the default and the visual feedback method for a RA of $45^\circ/-45^\circ$, and the difference in Young's modulus was significant as well. In Figure 4.2, a little to no removal of air gap was observed between the default and visual feedback methods for a RA of $45^\circ/-45^\circ$, and no significant difference in Young's modulus was found.

Figure 4.7 shows the tensile strain results for three build orientations. The highest average value of tensile strain obtained was about 8% for a RA of $45^\circ/-45^\circ$ using the Insight revision method (compared to 4.9% obtained using default method). The value ranges from 3.5%-8% in this

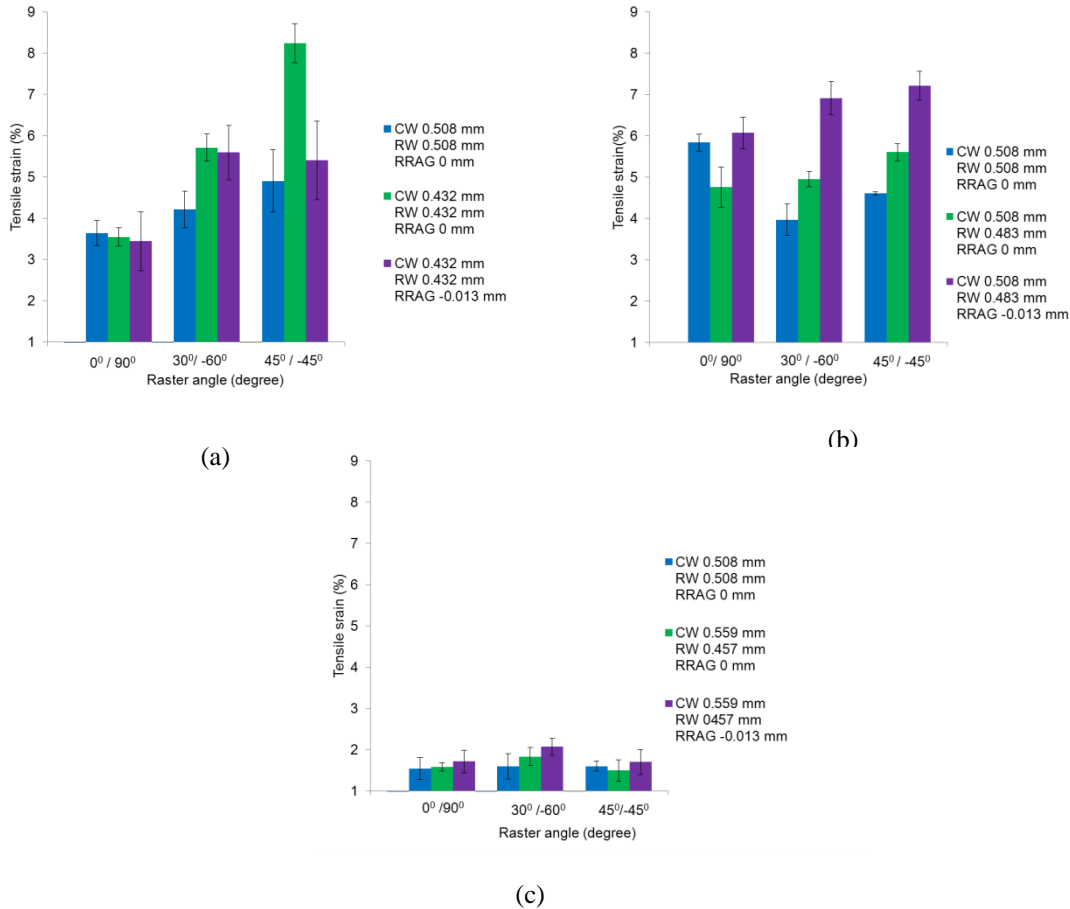


Figure 4.7: Tensile strain for a) XYZ build orientation, b) XZY build orientation and ZXY build orientation. Each bar represents the average of at least 5 specimens and the error bars are \pm standard deviation

orientation. The highest average value obtained of tensile strain, in XZY build orientation, was 7.2% for a RA of 45° using the visual feedback method (whereas 4.6% was obtained using the default method). In this case, the results range from 4%-7.2%. The maximum average value of tensile strain obtained, in the ZXY build orientation, was about 2% for a RA of 30° using the visual feedback method (1.6% was obtained using the default method). With ZXY build orientation, the value ranges from 1.5%-2%. The inter layer bonding is the main resistance to tensile load using ZXY build orientation, where little elastic deformation was observed prior failure. In the other 2 orientations, XYZ and XZY, elastic deformation occurred along the rasters. In this case, much more elongation was necessary for fracture. A tensile strain of 5% using PC was reported by Nadooshan, Daneshman, and Aghanajafi [29]. Finally, it can be noted that the higher values of tensile strain can be obtained by modifying build orientation and building parameters.

The characteristic stress-strain curves, using the results mentioned above, are shown in Figure 4.8. The graph is plotted using the average value obtained for three build orientations (XYZ,

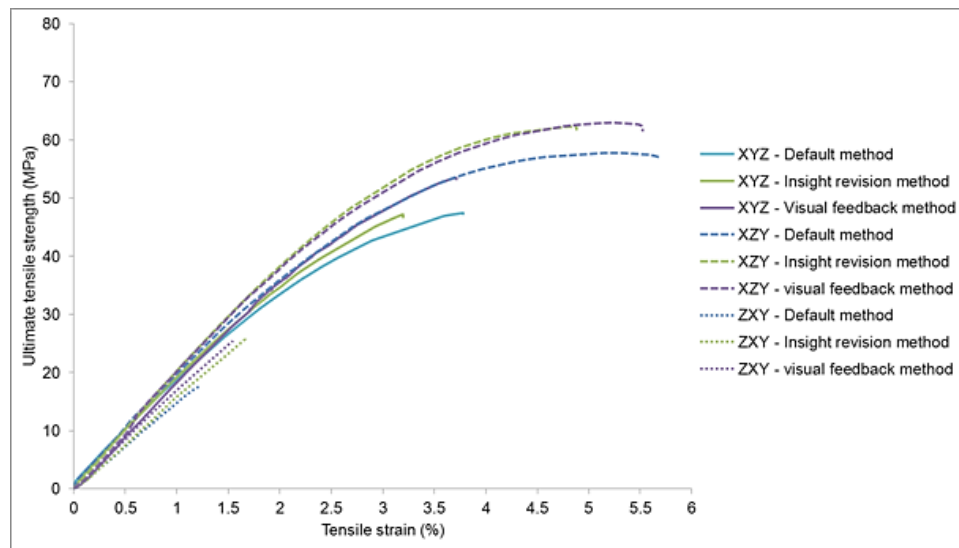


Figure 4.8: Characteristic stress-strain curves for three build orientations: XYZ, XZY, and ZXY. XYZ is represented by a solid line, XZY by a dashed line, and ZXY by a round dotted line. The default, Insight revision, and visual feedback methods are shown in blue, green, and purple lines, respectively

XZY, and ZXY) using the default, Insight revision method, and visual feedback methods. The graph shows the result for a RA of $0^\circ/90^\circ$, as there was not much difference observed using different RAs. The graph illustrates the benefits of performing parameter modification in contrast with mechanical properties.

4.1.3 Density measurement result

The density of three methods (default, Insight revision and visual feedback method) were measured using both of the test methods described in Section 3.5. The density results are shown in Table 4.4. The density increased using the visual feedback method when compared to other two methods. The density increased about 1.9%, and 1.6% using ASTM D1622, and ASTM D792 test methods, respectively when visual feedback method was compared to default method. The density results showed statistically significant difference when comparing default and visual feedback method using t-test for both test methods. The increase in density is an indication of air gap removal which can also act a sign in improving mechanical properties using visual feedback method.

4.2 Thermal Cycle Testing Result

4.2.1 Mechanical testing result

The thermal cycling tests showed that average value of UTS (Figure 4.9) remained in the range of 43.9-45.2 MPa. The results of UTS for no. of cycle 0 and 150 were not statistically

Table 4.4: Density measurement result using build parameter modification

Method	Density measured using ASTM D1622 (g/cm ³)	Standard deviation	Density measured using ASTM D792 (g/cm ³)	Standard deviation
Default	1.07	2.2×10^{-3}	1.098	1.23×10^{-3}
Insight revision method	1.08	8.1×10^{-4}	1.103	6.99×10^{-4}
Visual feedback method	1.09	1×10^{-3}	1.116	6.81×10^{-4}

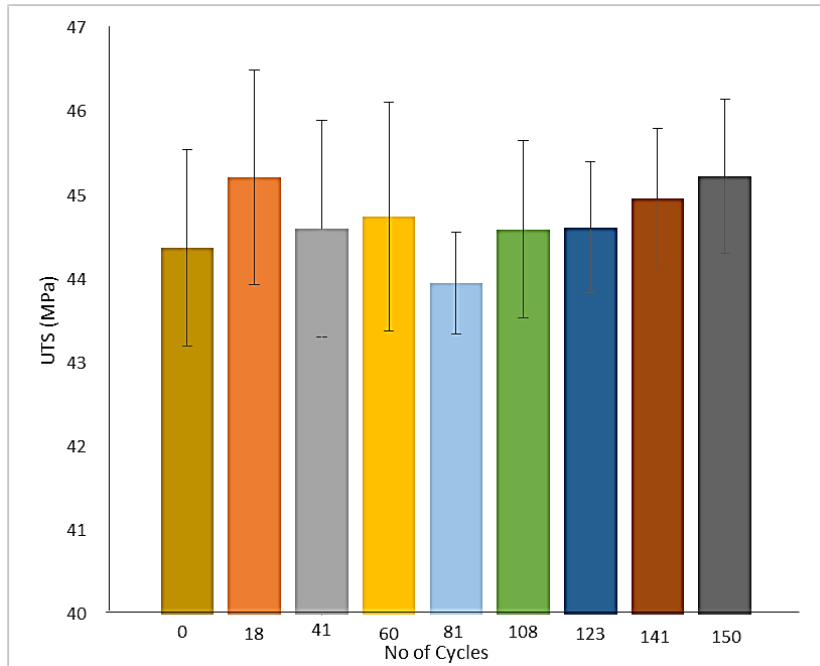


Figure 4.9: UTS result of thermal cycled specimen. Each bar represents the average of at least 5 specimens and the error bars are +/- standard deviation

different. One of the reasons for this might be that the maximum number of cycle was 150, which may be too low to induce a change in the UTS. The unchanged nature of UTS indicates the possibility of higher service life of a PC part, which may be used in the electrical wiring harnesses of automotive cars.

The Young's modulus (Figure 4.10) was increased with the increase of the thermal cycles. The Young's modulus increased from 1389 MPa to 1469 MPa after 150 thermal cycles. The increase in Young's modulus might have happened because of polymer hardening through the expansion and contraction due to thermal cycling [40]. The effect of cross linking of polymers might also increase the Young's modulus, though it is observed that cross-linking has little effect in glassy region [41]. As a result, there was a statistically significant change in Young's modulus when the no. of cycle was 0 and 150. However, this type of study for higher thermal cycles still leave question unanswered.

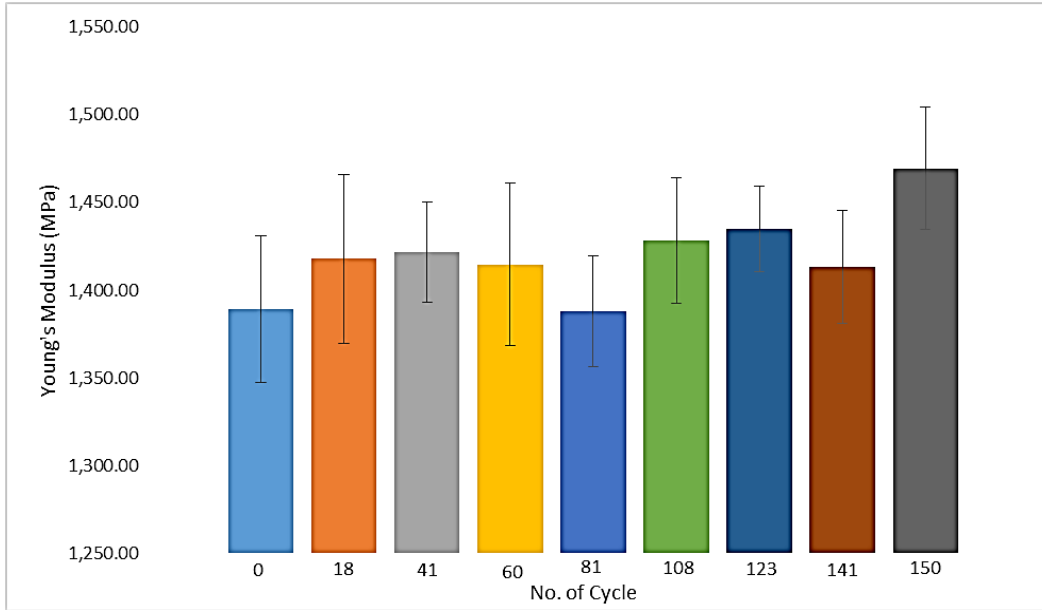


Figure 4.10: Young's modulus result of thermal cycled specimen. Each bar represents the average of at least 5 specimens and the error bars are +/- standard deviation

The tensile strain results (Figure 4.11) showed a tendency of decreasing with the increase of thermal cycle. The tensile strain decreased from 5.43% to 5.32% after 150 thermal cycles. The decrease of tensile strain might depend on the nature of polymer backbone [41]. Further analysis

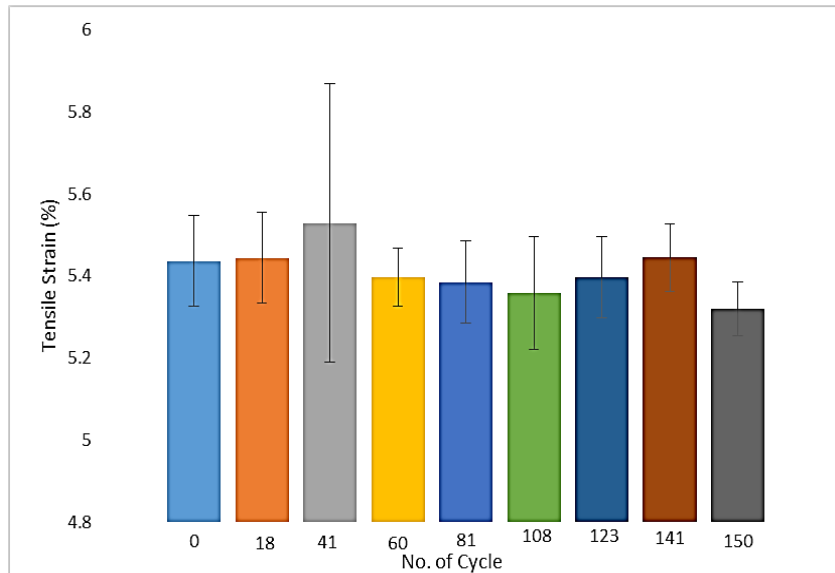


Figure 4.11: Tensile strain result of thermal cycled specimen. Each bar represents the average of at least 5 specimens and the error bars are +/- standard deviation

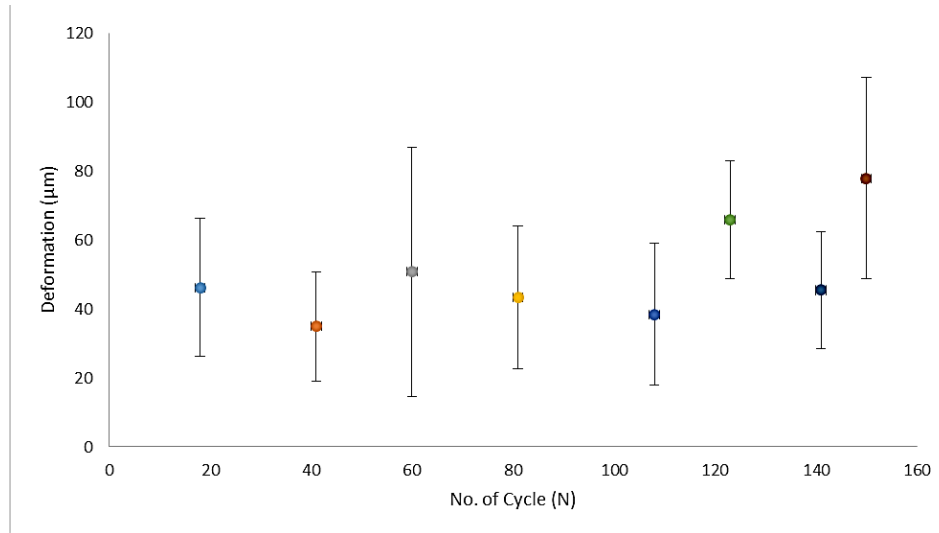


Figure 4.12: Deformation of thermal cycled specimen. Each bar represents the average of at least 5 specimens and the error bars are +/- standard deviation

needs to be performed to describe the tensile strain. The results of tensile strain for no. of cycle 0 and 150 are statistically significantly different, though the change is really small (0.11%).

4.2.2 Deformation result

The deformation of the tensile test specimen was observed throughout the thermal cycling. The deformation results are shown in Figure 4.12. The deformation was found to be around 35 μm – 78 μm . The deformation of the specimen was a result of the thermal cycle. Due to the thermal expansion and contraction of thermoplastic material, the interlayer bonding of two adjacent layers might be degraded. As a result, there might be a deviation from the specimen's previous state.

4.2.3 Glass transition temperature result

The glass transition temperature was measured in order to determine the effect of thermal cycling on the glassy to rubbery condition of PC. The results (Figure 4.13) show that the as-fabricated specimen has an average glass transition temperature of 152.58° C when compared to 161° C reported by Stratasys Inc. [42]. This property did not change significantly throughout the thermal cycle. The thermal cycle was well below the glass transition temperature which enables

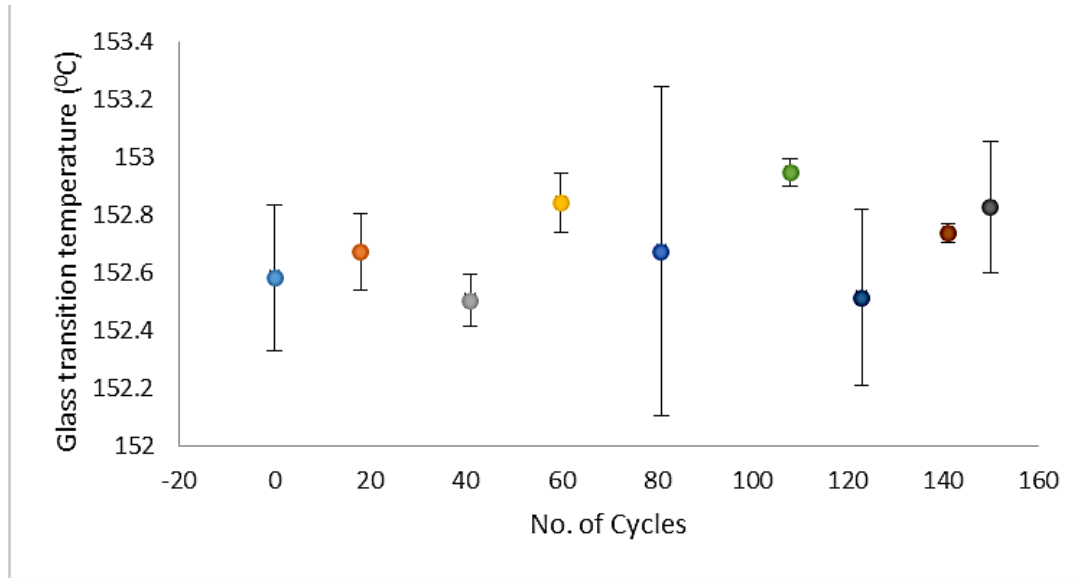


Figure 4.13: Glass transition temperature of thermal cycled specimen. Each bar represents the average of at least 5 specimens and the error bars are +/- standard deviation

the possibility of using PC in such a temperature. A minimum of 3 samples were tested for each step of the thermal cycle. The results showed negligible deviation in glass transition result due to thermal cycling.

4.3 Sealing Algorithm result

4.3.1 Density result

As mentioned earlier, the density of the test parts fabricated using the sealing algorithm was compared with the parts fabricated using the default parameters. The density measurement results are shown in Table 4.5. The results showed an increase of about 5.2%, and 3.4% in density for ASTM D1622, and ASTM D792 method, respectively, when comparing sealing algorithm method to the specimens built using the default parameters. The increase in density indicates the removal of air gaps in the fabricated parts which is the main concern in gaining sealed parts.

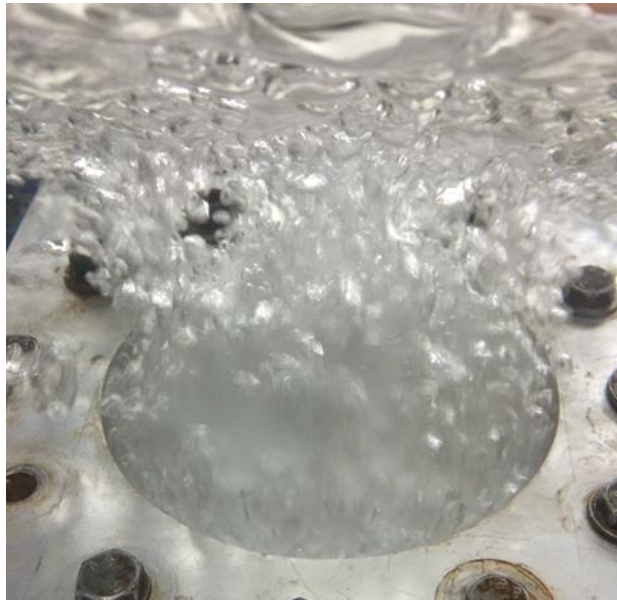
Table 4.5: Density measurement result

	Built using Default Parameters	Built using Sealing algorithm parameters
Number of samples	3	3
Density measured using ASTM D1622 (g/cm ³)	1.082	1.139
Standard deviation	2.13×10^{-3}	5.91×10^{-3}
Density measured using ASTM D792 (g/cm ³)	1.117	1.155
Standard deviation	6.82×10^{-4}	1.07×10^{-3}

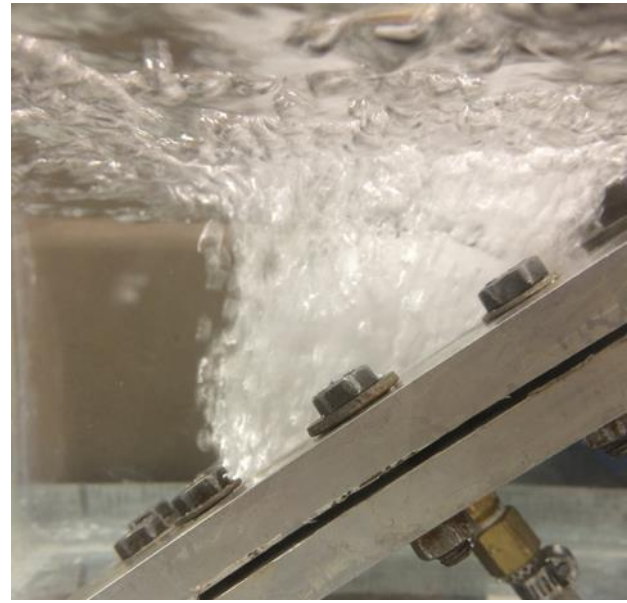
4.3.2 Pressure testing result

The sealing algorithm was developed to reduce or completely remove the air gaps present in FDM fabricated parts. As a baseline, the circular dome, fabricated using the default parameters, was tested using the test set-up described in Section 3.11. The results showed leakage, evident by bubble formation in the water (Figure 4.14) during testing at 34.5 kPa (5 psi). This demonstrates the present condition of FDM fabricated parts in fluid pressure application.

The flat plate specimen showed a sealed part fabrication was possible using FDM system. As mentioned earlier, the flat plate sealed part was achieved using the visual inspection from renderings created by Insight and choosing different RRAG, based on trial and error basis. This method was possible because the simple plate design containing layers of same thickness. Therefore, removing air gaps from one layer with a specific set of FDM processing parameters represented a solution for all layers. This method would obviously be very cumbersome for parts whose layer's geometry changes throughout. As such, the next step was to fabricate a part that can be built without the help of using Insight renderings. As a result, the sealing algorithm was developed to fabricate FDM sealed part using two types of design, 1) square feature and 2) circular dome. The processing parameters were described in Section 3.9. The square feature showed leakage in the pressure testing (Figure 4.15). It is important to note that the leakage was observed mainly in the edges of the part. Point to be noted that the contours were totally exposed in the outer



Front view



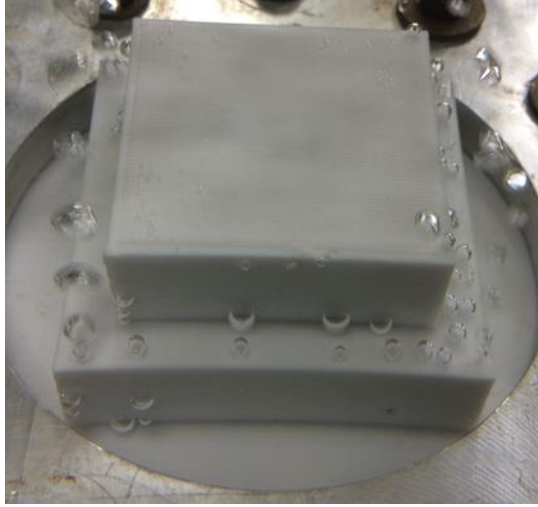
Side view

Figure 4.14: Pressure testing on circular dome using default parameters. The figure depicts a large amount of air bubble formation in the water.

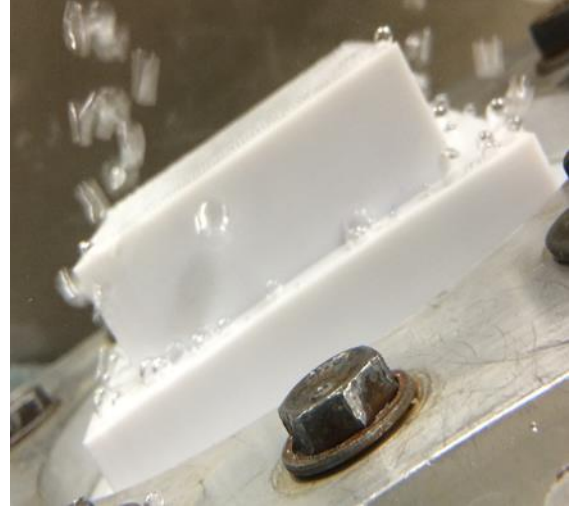
surface which were not modified to remove air gaps in the sealing algorithm method. For the contours, the only modification was the use of linking contour option. It created the link contours in comparison to contours with multiple seams. This was done to minimize the defect of seam lines. The square feature showed less quantity of bubbles in comparison to the circular dome that was built using default parameters (Figure 4.14). In the future, the modification of the contour deposition will also be considered for better performance.

The circular dome was tested using the same procedure and found no visible evidence of air bubbles. The circular dome was completely sealed up to 137 kPa (20 psi). At 30 psi, there was some (around 3-6) bubbles formed that attached to the dome surface. The pressure test results are shown in Figure 4.16.

An analytical study can determine the maximum allowable pressure allowed by an injection molding and compare it with the result obtained from the FDM fabricated parts. For the



Front view



Side view

Figure 4.15: Pressure testing on square feature using modified sealing algorithm parameters. The figure depicts some air bubble formation in the water.

analytical calculation, it was assumed to be thick walled spherical shell [44]. The UTS of injection molded PC parts were taken as 62 MPa [45] and a factor of safety of 4.75 was considered [46].

So, the maximum allowable stress is $(\sigma_{\text{injection molding}})_{\text{allowable}} = \frac{62}{4.75} = 13.05 \text{ MPa}$

For thick walled spherical shell,

$$(\sigma_{\text{injection molding}})_{\text{allowable}} = \frac{PR_2^3}{2(R_2^3 - R_1^3)} + \frac{PR_1^3}{2(R_2^3 - R_1^3)}$$

Here, R_1 = inner radius, 40.64 mm

R_2 = outer radius, 50.8 mm

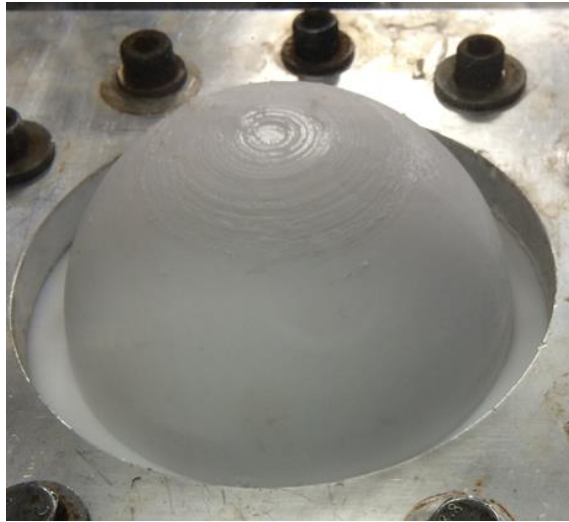
P = internal pressure

By calculating, internal pressure was 6.29 MPa for injection molded PC parts.

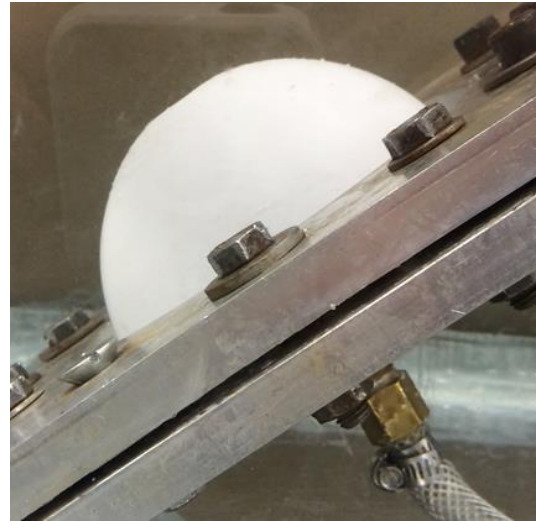
Now, comparing the result obtained from FDM fabricated parts, results obtained from Figure 4.4 for ZXY build orientation (as possible failure might happen due to detaching of interlayer bonding). A UTS of 27.26 was taken for a RA of 0°/90° using visual feedback method.

So, the maximum allowable stress is $(\sigma_{\text{FDM fabrication}})_{\text{allowable}} = \frac{27.26}{4.75} = 5.74 \text{ MPa}$

Using the same equation for thick walled spherical shell, the internal pressure of 2.76 MPa was obtained which is around 50% in compare to injection molded PC parts. If the FDM fabricated



Front view

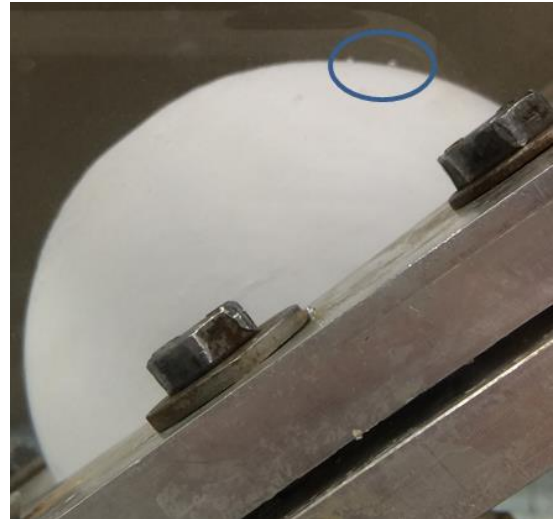


Side view

At 137 kPa (20 psi)



Front view



Side view

At 206 kPa (30 psi)

Figure 4.16: Pressure testing on circular dome using modified sealing algorithm parameters. The figure depicts no air bubble formation in the water at 137 kPa. Few air bubbles formed and stick to the surface at 206 kPa. Some bubbles are circled in the figure.

parts can be fully sealed, it should be able to withstand the pressure of 2.76 MPa using the current setup. It is worth noting that, a maximum pressure of 137 kPa was obtained without showing any kind of bubble formation during experiment.

CHAPTER 5: Conclusion and Recommendations

5.1 Conclusion

It was found that building parameters can play a vital role in improving mechanical properties of FDM produced parts. The higher UTS was obtained using Insight revision method parameters, rather than using default values. The UTS further improved using visual feedback method by introducing negative RRAGs. The visual feedback method resulted in an average increase in UTS of 16%, 7%, and 22% for XYZ, XZY, and ZXY build orientations, respectively, when compared to the default method. The optical image analysis led to the realization that the gap between rasters can have a detrimental effect on mechanical properties. The removal of those gaps actually led to the improvement of the mechanical properties. Another realization was, that although gaps were present, they were not visible with the Insight software. As a result, a negative RRAG was used to remove those previously unidentified gaps. The negative RRAG allowed the rasters to attach with each other in the same layer which ultimately improved the mechanical properties of the fabricated parts. Among three build orientations, XZY showed higher UTS in comparison to the other two. The higher number of contours were deposited along the tensile loading direction when XZY build orientation was used in compare to the other two build orientations. This might be the reason of improvement in achieving higher UTS. In ZXY orientation, the only resistance to tensile loading was the bonding between two adjacent layers. As a result, specimens built in ZXY build orientation depicted lower UTS. This fact has to be considered when producing FDM fabricated parts for engineering applications.

The mechanical properties of thermal cycled parts were also addressed in this study. The mechanical testing results and deformation results showed the possibility of using the PC fabricated parts in engineering applications where thermal cycling might be a factor. The glass transition temperature also did not change significantly during testing.

Finally, a sealing algorithm was developed in this study which is a novel initiative in FDM technology. The entire process was non-destructive and did not need any in-situ monitoring during fabrication process (both are alternative methods that may be considered) which could reduce

various complications in obtaining sealed FDM parts. Previously, the FDM parts were sealed using different kinds of sealant or post processing [32]. The current study did not require any post processing, and sometimes costly, techniques. The pressure test showed that the fabricated part can withstand 138 kPa without showing any type of leakage. This can lead to the possibility of holding a FDM fabricated cup in hand without any chance of leaking. The fabrication of a sealed water hose, or a pipe for a home using a 3D printer might be possible in the future. This study shows the sealed parts up to 138 kPa, in case of higher pressure (e.g., 400 kPa or more) high strength material (such as, PPSF, ULTEM 9085) might be used. This shows the possibilities brought forth by an improvement at the processing parameter selection level. Moreover, the sealing algorithm does not require any additional time or cost of conventional sealing process (applying sealants, hot isostatic pressing, etc.) as there is no additional post-processing involved. Theoretically, FDM fabricated parts can withstand 2.76 MPa, if that's possible, a variety of applications might happen. Obviously, the industries will benefit from gaining access to improved mechanical properties, and sealed FDM parts.

5.2 Recommendations for Future Work

Further studies of the interlayer bonding can be an effective step as interlayer bonding showed lower tensile properties. The external input (e.g., UV light cure, solvent deposition) process in between two adjacent layers can be implemented which might improve mechanical properties for the specimens build in ZXY orientation. The process might contain an additional curing (in case of UV light cure) or material dispensing system (in case of solvent deposition) along with FDM system. The effect of layer thickness can also be tested as it may preferably show good resolution or surface finish after fabrication process but it will surely consume significant amount of time as more layers has to be built.

The higher thermal cycle can be explored to have more insight on mechanical properties, dimensional changes, degradation of material, etc. The temperature rate can be increased to observe any kind of thermal shock and rapid deformation.

The contour modification will be accounted in the sealing algorithm as it surely opens the possibility to seal each layer more properly. As a result, it surely will increase the possibility to obtain as fabricated sealed parts for complex geometries. In addition, a higher pressure test (circular dome was only tested up to 207 kPa) needs to be performed to see the complete leakage. A computed tomography (CT) scan study can be done to see the internal condition of the tested part and compare it with the previous testing condition to figure out weak zone of the design. As well, CT scan can be done on the parts fabricated using sealing algorithm and can be cured the local defect zone using adhesives. In future, the sealing algorithm will include different RAs (e.g., 30°/-60°, 45°/-45°, etc.) in extension of present study for 0°/90° RA. The improvement of mechanical properties using sealing algorithm will also be justified in future. As different machines have different dimensional accuracies and also may have different deposition algorithms, so some protocol factor needs to be obtained to transfer the sealing process from one machine to another.

References

- [1] (2012) Standard Terminology for Additive Manufacturing Technologies. ASTM International. Designation: F2792-12a
- [2] Kruth, J. P., Leu, M.C., and Nakagawa, T., (1998), "Progress in Additive Manufacturing and Rapid Prototyping" Keynote papers, Annals of the CIRP Vol. 47 (2)
- [3] Stucker B (2012) Additive manufacturing technologies: technology introduction and business implications. In: Frontiers of engineering; reports on leading-edge engineering from the 2011 symposium. National Academies Press, Washington DC, pp 5-14
- [4] Murr, L. E., Gaytan, S. M., Medina, F., Martinez, E., Martinez, J. L., Hernandez, D. H., & Wicker, R. B. (2010). "Characterization of Ti-6Al-4V open cellular foams fabricated by additive manufacturing using electron beam melting", Materials Science and Engineering, A527(7), 1861-1868
- [5] Vayre, B., Vignat, F., and Villeneuve, F., 2012, "Designing for Additive Manufacturing", 45th CIRP Conference on Manufacturing Systems 2012, Procedia CIRP 3, pp 632-637
- [6] Crump, S. C., 1992, "Apparatus and Method for Creating Three-Dimensional Objects", United States Patent, Patent number 5,121,329
- [7] Kruth, J.P., Leu, M.C., and Nakagawa, 1998, "Progress in Additive manufacturing and Rapid Prototyping", keynote paper, Annals of the CIRP Vol. 47
- [8] Gibson, I., Rosen, D.W., Stucker, B., 2010, "Additive manufacturing technologies: rapid prototyping to direct digital manufacturing". Springer, New York
- [9] Wang, T., Xi, J., Jin, Y., 2007, "A model research for prototype warp deformation in the FDM process". International Journal of Advanced Manufacturing Technology 33 (11-12), 1087-1096
- [10] Sun Q, Rizvi GM, Bellehumeur CT, Gu P., (2008), "Effect of processing conditions on the bonding quality of FDM polymer filaments". Rapid Prototyping J 14:72-80. doi: 10.1108/13552540810862028
- [11] (2011) Standard Terminology for Additive Manufacturing-Coordinate Systems and Test Methodologies. ASTM International. Designation: F2921-11
- [12] Perez M, Block M, Espalin D, Winker R, Hoppe T, Medina F, and Wicker R., 2012, "Sterilization of FDM-manufactured parts", In: Proceedings of the 2012 Annual International Solid Freeform Fabrication Symposium, Austin, TX, USA
- [13] Espalin D, Arcaute K, Rodriguez D, Medina F, Posner M, Wicker R (2010) "Fused deposition modeling of patient-specific polymethylmethacrylate implants" Rapid Prototyping J 16:164-173. doi: 10.1108/13552541011034825
- [14] Zein I., Dietmar W.H., Tan K.C., Teoh S.H., 2002, "Fused deposition modeling of novel scaffold architectures for tissue engineering applications", Biomaterials 23:1169-1185
- [15] Kalita SJ, Bose S, Hosick HL, Bandyopadhyay A (2003), "Development of controlled porosity polymer-ceramic composite scaffolds via fused deposition modeling". Mater Sci Eng 26:611-620

- [16] Mireles, J., Espalin, D., Roberson, D., Zinniel, B., Medina, F., and Wicker, R., 2012, "Fused Deposition Modeling of Metals", In Proceedings of the 2012 Annual International Solid Freeform Fabrication Symposium, Austin, TX, USA
- [17] Masood, S. H., Mau, K., and Song, W. Q., 2010, " Tensile Properties of Processed FDM Polycarbonate Material", Materials Science Forum Vol. 654-656, pp 2556-2559, doi: 10.4028/www.scientific.net/MSF.654-656.2556
- [18] Ahn S.H., Montero M., Odell D., Roundy S., and Wright PK ,2002, "Anisotropic material properties of fused deposition modeling ABS". Rapid Prototyping J 8:248-257. doi:10.1108/13552540210441166
- [19] Sood A.K., Ohdar R.K., Mahapatra S.S., 2010, "Parametric appraisal of mechanical property of fused deposition modelling processed parts". Mater Design 31:287-295
- [20] Montero, M., Roundy, S., Odell, D., Ahn, S. H., and Wright, P. K.,2001, Proceedings of Rapid Prototyping and Manufacturing Conference, SME
- [21] Bellini, A., Güçeri, S., 2003, " Mechanical characterization of parts fabricated using fused deposition modeling", Rapid Prototyping J, (9)252-264. doi: 10.1108/13552540310489631
- [22] E. Aguilera, J. Ramos, D. Espalin, F. Cedillos, D. Muse, R. Wicker, and E. MacDonald, 2013," 3D Printing of Electro Mechanical Systems",In: Proceedings of the 2013 Annual International Solid Freeform Fabrication Symposium, Austin, TX, USA
- [23] Shimokawa,T., Katoh, H., Hamaguchi, Y., Sanbongi, S., Mizuno, H., Nakamura, H., Asagumo, R., and Tamura, H., "Effect of Thermal Cycling on Microcracking and Strength Degradation of High-Temperature Polymer Composite Materials for Use in Next-Generation," SST Structures", Journal of Composite Materials, 2002, 36:885
- [24] Chung, K., Seferis, J. C., Nam, J., D., " Investigation of thermal degradation of polymeric composites: prediction of thermal cycling effect from isothermal data", Composites: Part A 31 (2000) 945-957
- [25] Sperling, L. H., 2006, "Introduction to Physical Polymer Science", Fourth edition, John Wiley & Sons, Inc. , Hoboken, New Jersey
- [26] Halary, J., Laupretre, F., Monnerie, L., 2011, "Polymer Materials", A John Wiley & Sons Inc. Publication, ISBN 978-0-470-61619-2
- [27] Nicholson, J. W., " The Chemistry of Polymers", Third Edition, The Royal Society of Chemistry, Cambridge, UK, ISBN 0-85404-684-4
- [28] Stratasys, "Strength Under Pressure",
<http://www.stratasys.com/~media/Case%20Studies/Consumer%20Goods/SSYS-CS-Fortus-Toro-08-13.ashx>
- [29] Nadooshan, A.A., Daneshmand, S., Aghanajafi, C., 2007 "Application of RP technology with polycarbonate material for wind tunnel model fabrication", Proc Wrld Acad Sci E 2
- [30] Nagl, M., and T. Lechleitner. "Barrier coatings for medical electronic implants." Vakuum in Forschung und Praxis 17.S1 (2005) 47-50
- [31] Zaheed, L., and R. J. J. Jachuck. "Review of polymer compact heat exchangers, with special emphasis on a polymer film unit." Applied Thermal Engineering 24.16 (2004) 2323-2358
- [32] Mireles, J., Adame, A., Espalin, D., Medina, F., Winker, R., Hoppe, T., Zinniel, B., and Wicker, R., "Analysis of sealing methods for FDM-fabricated parts." University Of TEXAS-El PASO (2011)

- [33] Parker, M., West, M., Arbogast, M. W., & Boysen, A. (2010). "Eliminating Voids in FDM Processed Polyphenylsulfone, Polycarbonate, and ULTEM 9085 by Hot Isostatic Pressing". Minerals, Metals and Materials Society/AIME, 420 Commonwealth Dr., P. O. Box 430 War
- [34] Espalin, D., Medina, F., Arcaute, K., Zinniel, B., Hoppe, T., & Wicker, R. (2009, May). "Effects of vapor smoothing on ABS part dimensions". In Proceedings from Rapid 2009 Conference & Exposition, Schaumburg, IL
- [35] <http://www.globalsecurity.org/military/systems/aircraft/f-22-cockpit.htm>
- [36] (2010) Standard Test Method for Tensile Properties of plastics. ASTM International. Designation: D638-10
- [37] (2008) Standard Practice for Conditioning Plastics for Testing. ASTM International. Designation: D618-08
- [38] ASTM International, "Standard Test Method for Apparent Density of Rigid Cellular Plastics", ASTM D1622-14
- [39] ASTM International, "Standard Test Method for Density and Specific Gravity (Relative Density) of Plastics by Displacement, ASTM D792-13
- [40] Foreman, J., Sauerbrunn, S. R., & Marcozzi, C. L. (2006). "Exploring the sensitivity of thermal analysis techniques to the glass transition". TA Instruments: Thermal Analysis & Rheology
- [41] Pretsch, T. (2010). "Triple-shape properties of a thermoresponsive poly (ester urethane)" Smart Materials and Structures, 19(1), 015006
- [42] Landel, R. F., & Nielsen, L. E. (1993). Mechanical properties of polymers and composites. CRC Press. pp 49-50
- [43] Stratasys, FDM thermoplastics, 3D print durable parts in production-grade materials, <http://www.stratasys.com/materials/fdm>
- [44] Jindal, U.C., 2012, "Strength of Materials", Pearson Education India, ISBN-13: 978-81-317-5909-7
- [45] Żenkiewicz, M., Rytlewski, P., Moraczewski, K., Stepczyńska, M., Karasiewicz, T., Richert, J., & Ostrowicki, W. (2009). Effect of multiple injection moulding on some properties of polycarbonate. Archives of Materials Science and Engineering, 37(2), 94-101
- [46] The Engineering Toolbox, http://www.engineeringtoolbox.com/factors-safety-fos-d_1624.html
- [47] User Guide, FDM Titan, Version 1.4, Stratasys
- [48] uPrint SE, Stratasys, <http://www.stratasys.com/3d-printers/idea-series/uprint-se>
- [49] Fortus 900mc, Stratasys, <http://www.stratasys.com/3d-printers/production-series/fortus-900mc>
- [50] T.T. Wohlers, 2013, "Wohlers Report 2013: Additive Manufacturing and 3D Printing State of the Industry", Annual Worldwide Progress Report, 2013
- [51] Johnson, R. W., Evans, J. L., Jacobsen, P., Thompson, J. R., and Christopher, M., 2004, "The Changing Automotive Environment: High-Temperature Electronics", IEEE transactions on Electronics Packaging Manufacturing, Vol. 27, No. 3

- [52] Hattori, M., 1999, "Needs and applications of high-temperature LSIs for automotive electronic systems," in Proc. HITEN High-Temperature Electronics Conf., pp. 37-43

Appendix A

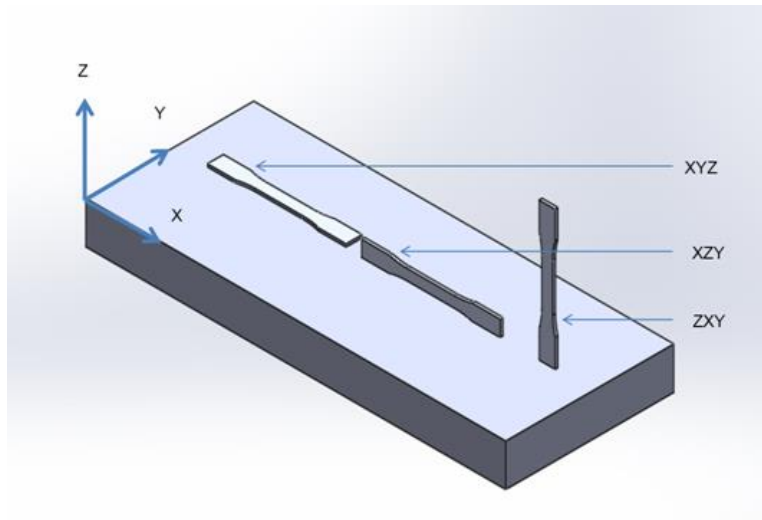


Figure A1: Three build orientations for the tensile specimens based on ASTM F2921 terminology

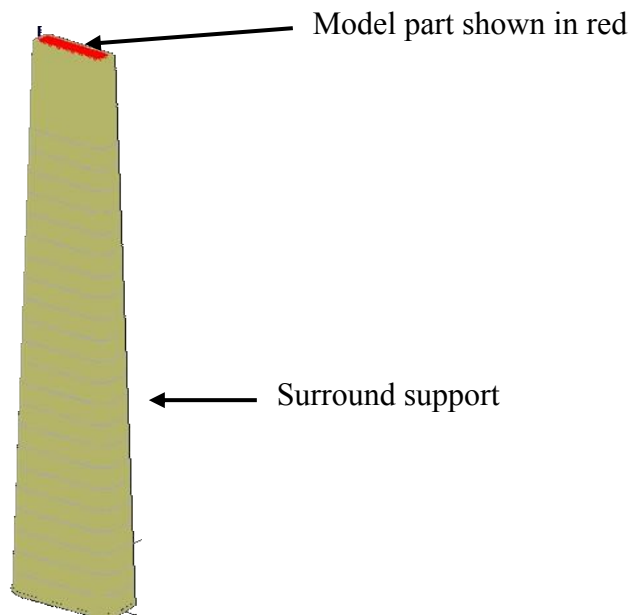


Figure A2: The surround support style for specimen built in ZXY orientation

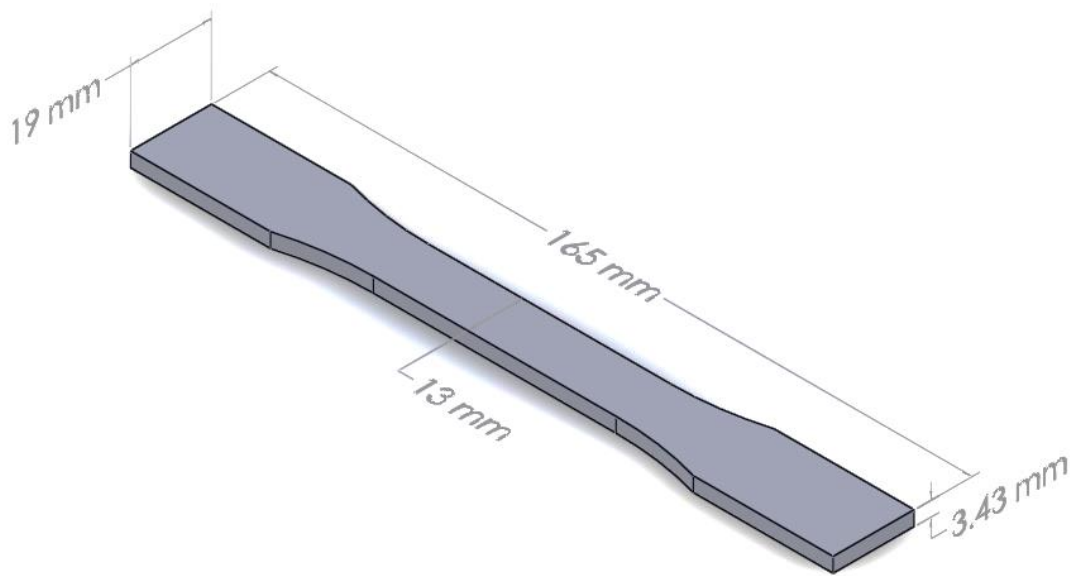


Figure A3: Tensile test specimen. Dimensions according to ASTM D638 type I specimen

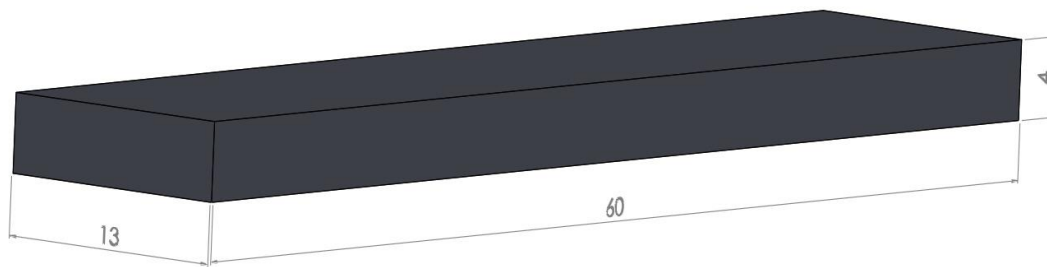


Figure A4: Dimensions of glass transition temperature measurement specimens

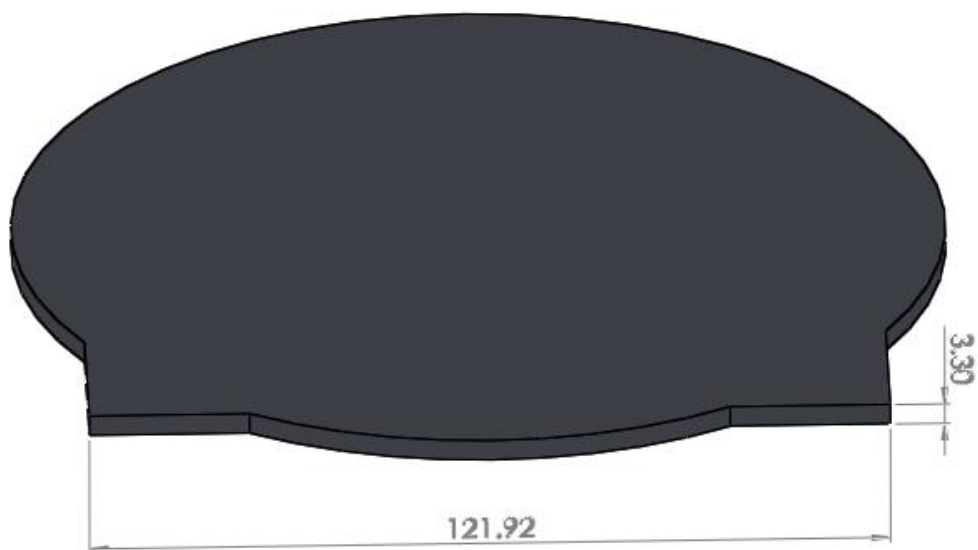
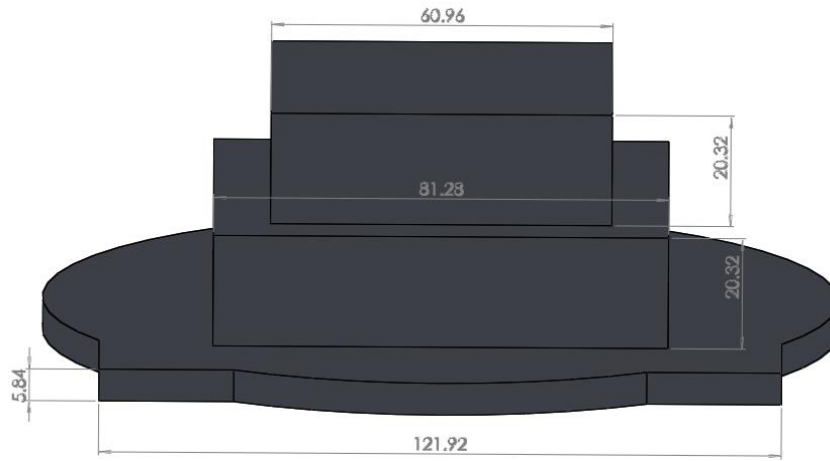
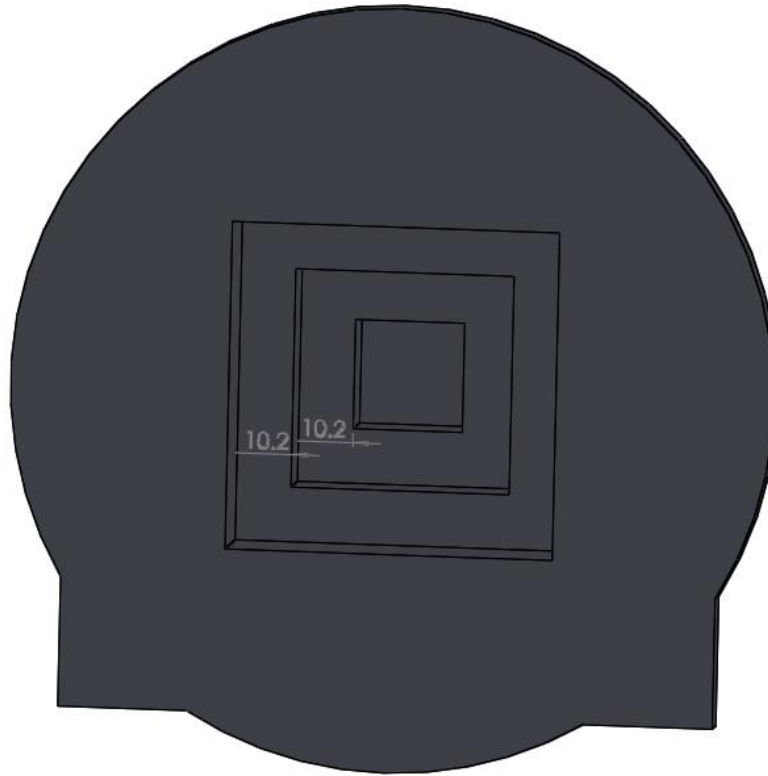


Figure A5: Flat plate specimen for pressure test. All the dimensions are in mm

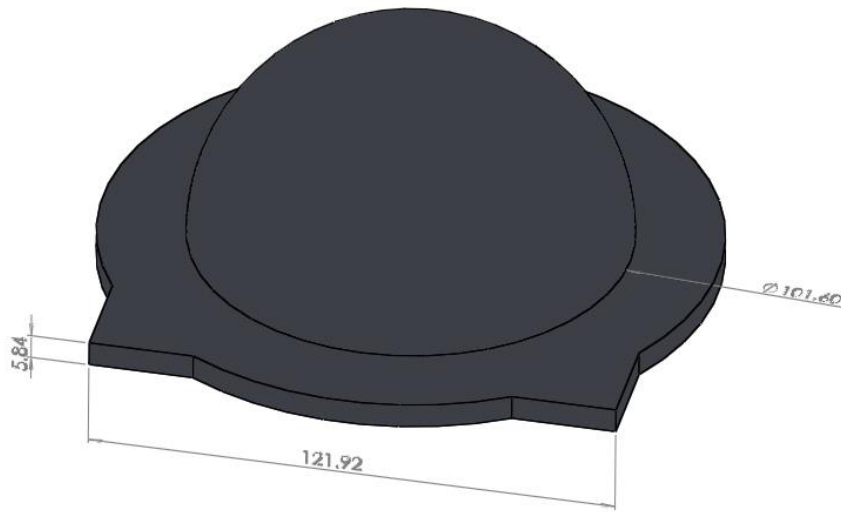


(a)

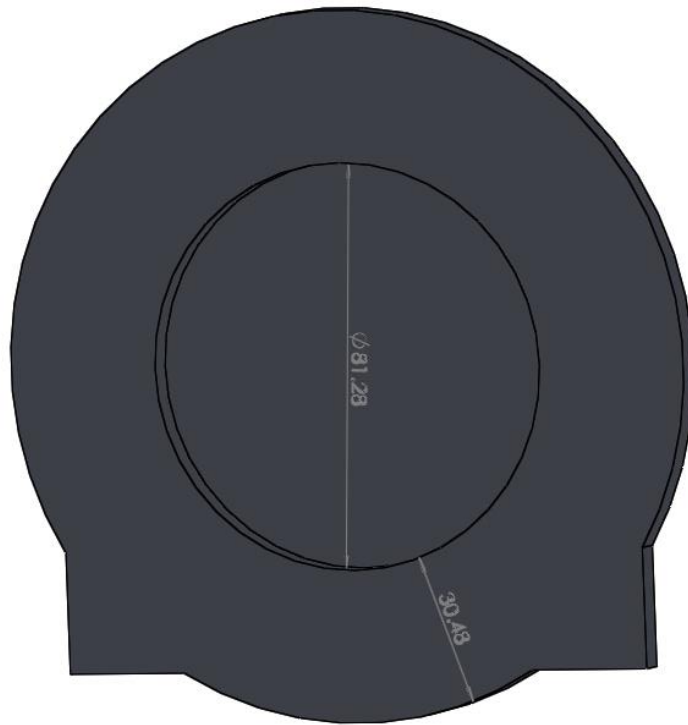


(b)

Figure A6: Square feature specimen for pressure test (a) top view, (b) bottom view. All the dimensions are in mm.



(a)



(b)

Figure A7: Circular dome specimen for pressure test (a) top view, (b) bottom view. All the dimensions are in mm

Appendix B

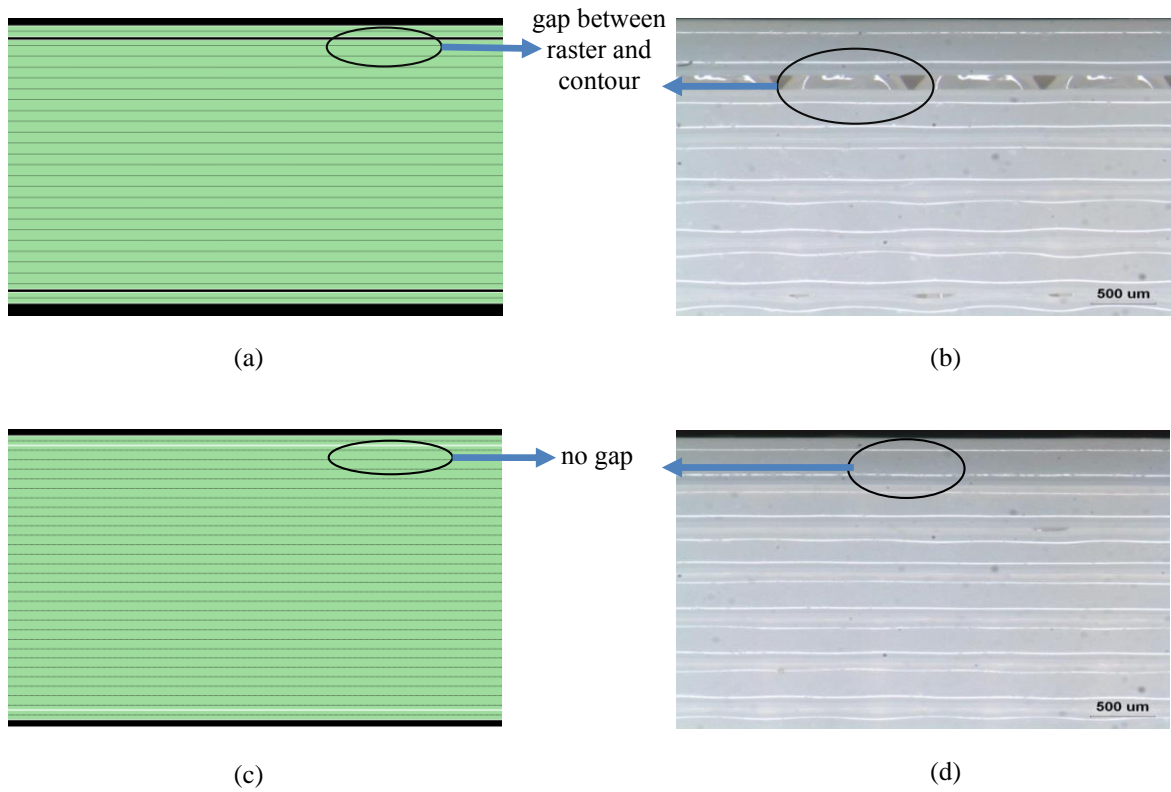


Figure B1: Rendered toolpaths generated by Insight (left) and actual deposited material (right) for the XYZ orientation using a $0^\circ/90^\circ$ raster angle; a) and b) default parameters (CW 0.508 mm, RW 0.508 mm, RRAG 0 mm), c) and d) Insight revision method parameters (CW 0.432 mm, RW 0.432 mm, RRAG 0 mm)

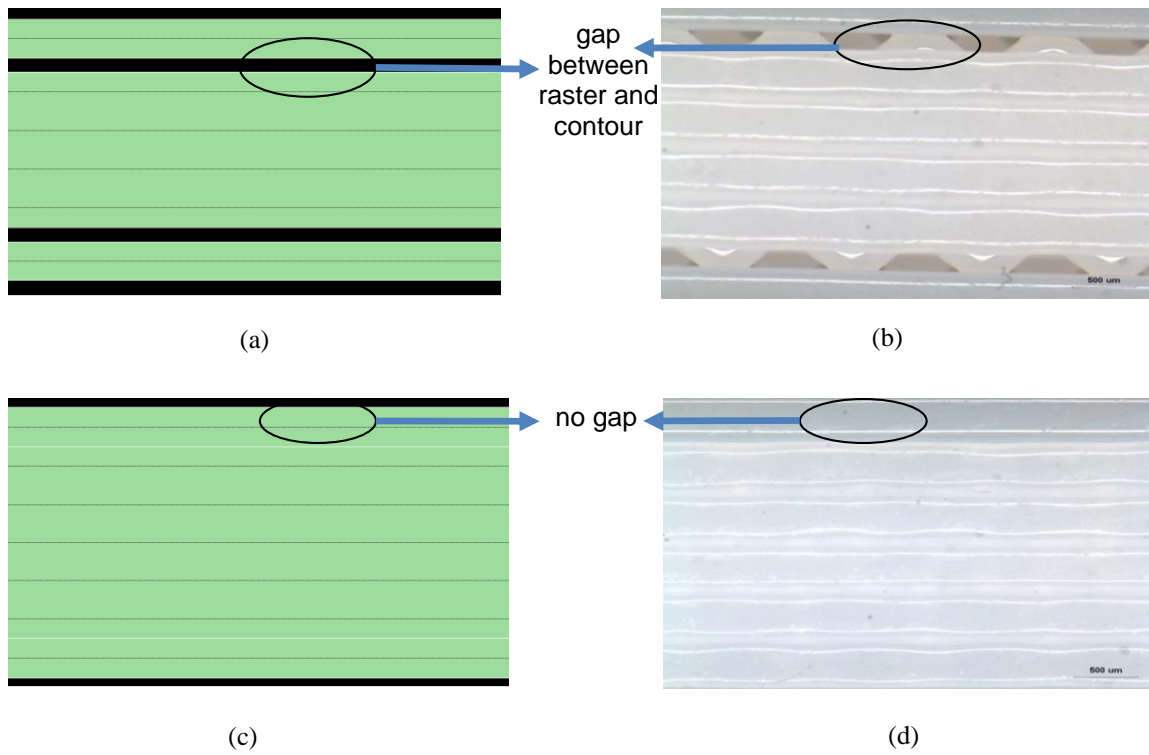


Figure B2: Rendered toolpaths generated by Insight (left) and actual deposited material (right) for the XZY orientation using a $0^{\circ}/90^{\circ}$ raster angle; a) and b) default parameters (CW 0.508 mm, RW 0.508 mm, RRAG 0 mm), c) and d) Insight revision method parameters (CW 0.508 mm, RW 0.483 mm, RRAG 0 mm)

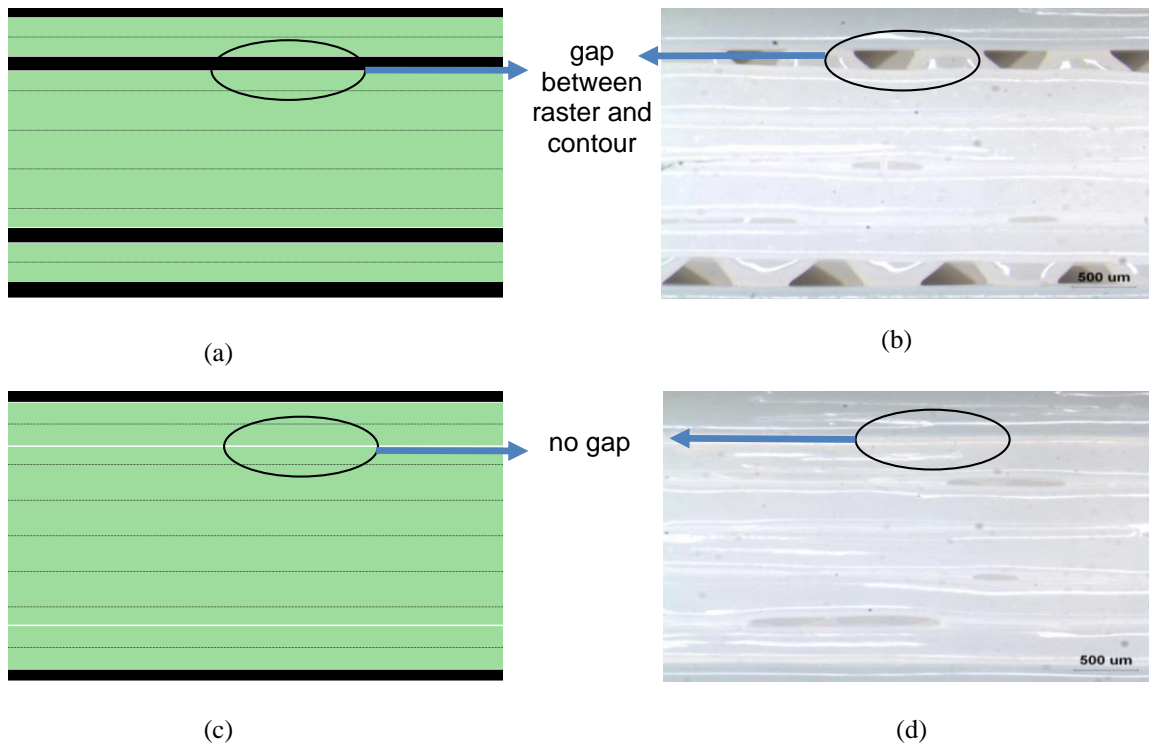


Figure B3: Rendered toolpaths generated by Insight (left) and actual deposited material (right) for the ZXY orientation using a $0^\circ/90^\circ$ raster angle; a) and b) default parameters (CW 0.508 mm, RW 0.508 mm, RRAG 0 mm), c) and d) Insight revision method parameters (CW 0.559 mm, RW 0.457 mm, RRAG 0 mm)

Appendix C

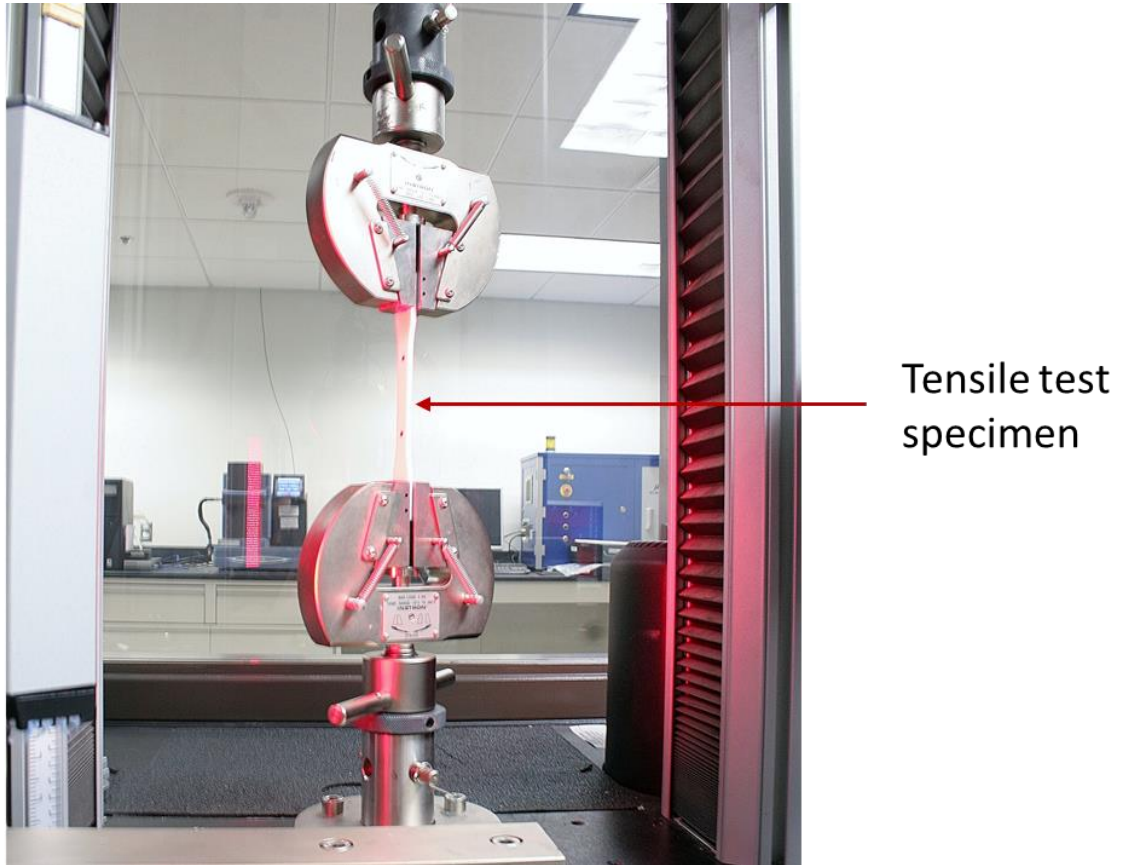


Figure C1: Tensile test set-up

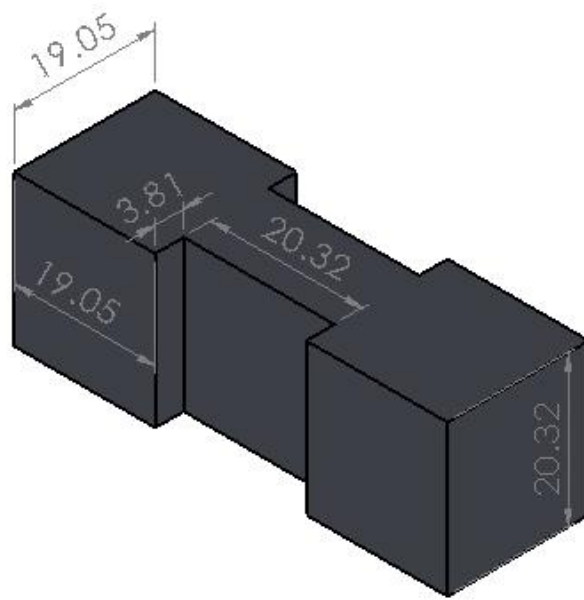


Figure C2: Dimensions of specimens for density measurement test using modifying parameter



Warping test specimen

Figure C3: Warping measurement

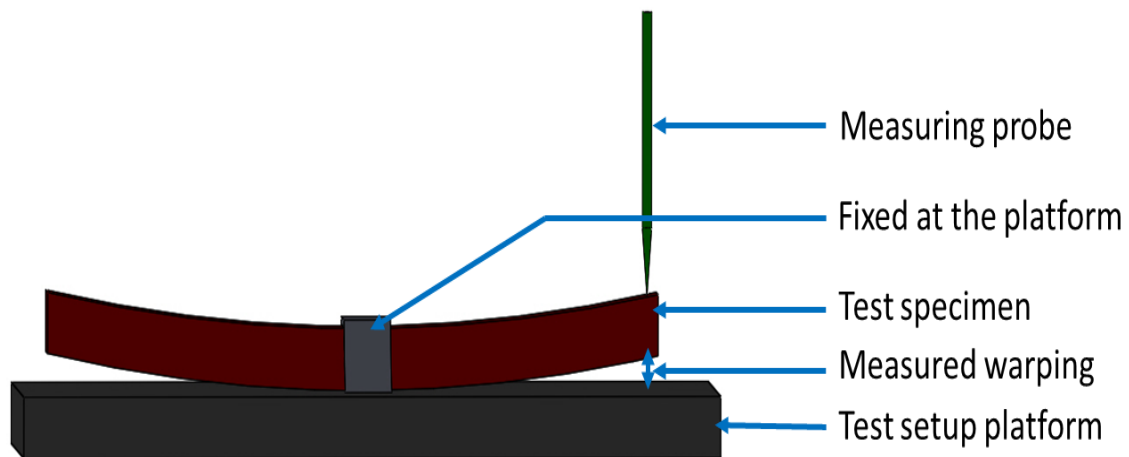


Figure C4: Schematic diagram of warping measurement procedure

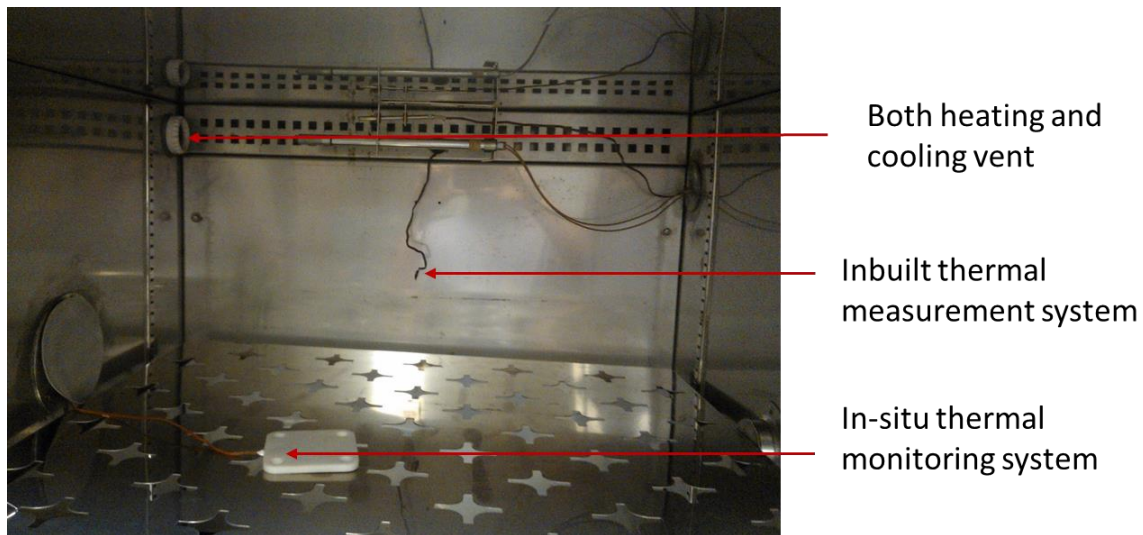


Figure C5: Thermal test set-up

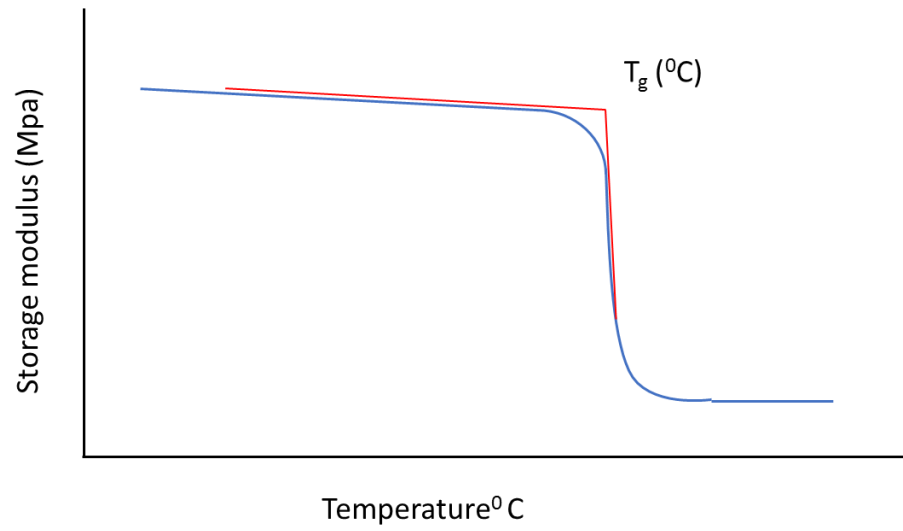


Figure C6: Schematic diagram of glass transition temperature measurement

Appendix D

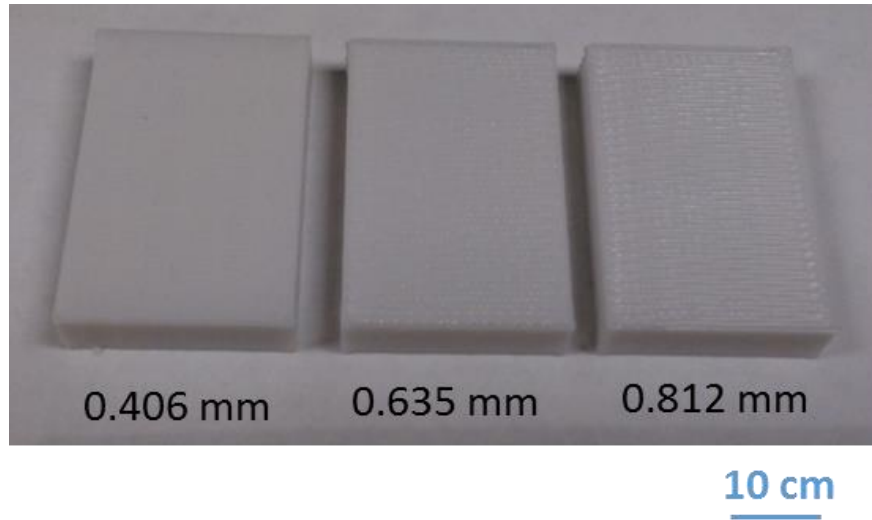
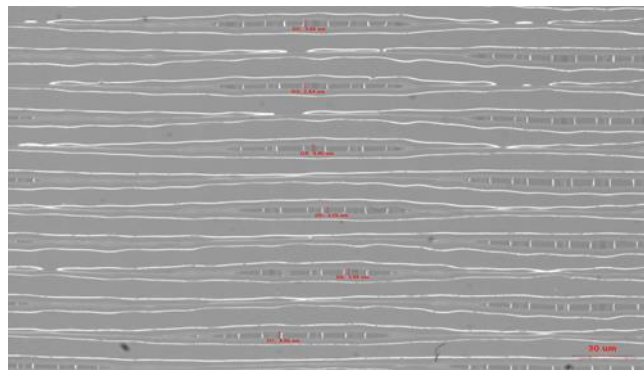


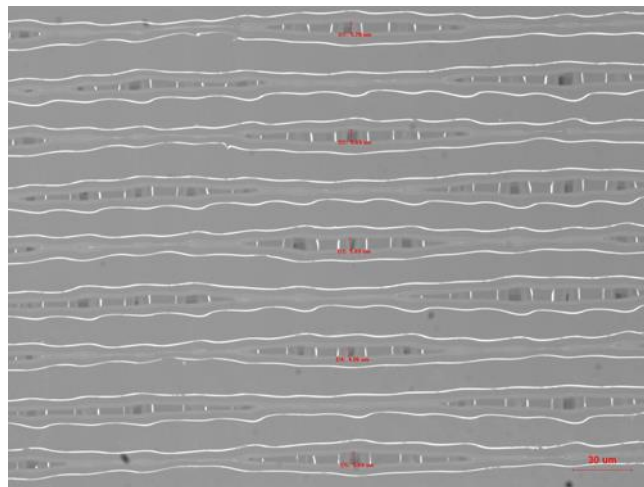
Figure D1: Specimens for determining RW limit based on gaps in between rasters. In this case, three different samples were fabricated using RW equal to 0.406 mm, 0.635 mm, and 0.812 mm respectively.



RW 0.406 mm RRAG 0

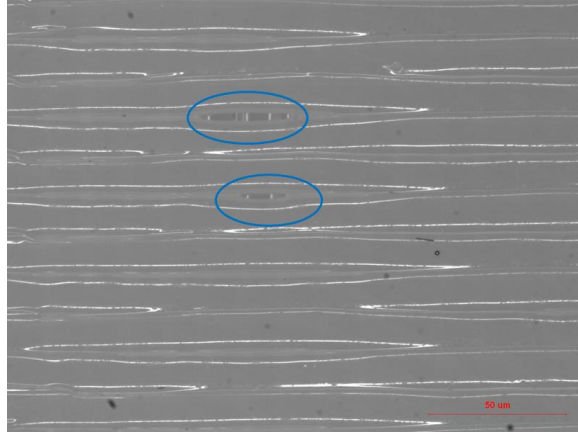


RW 0.635 mm RRAG 0

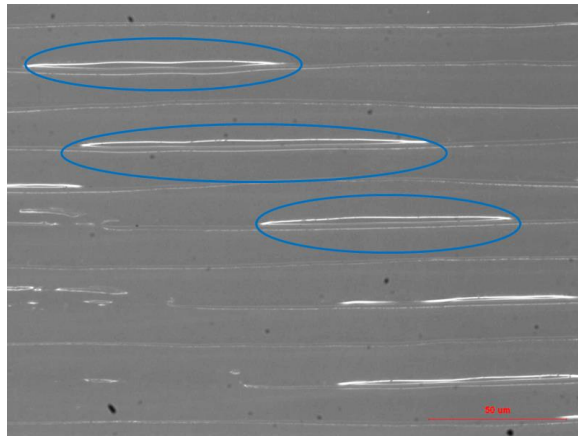


RW 0.812 mm RRAG 0

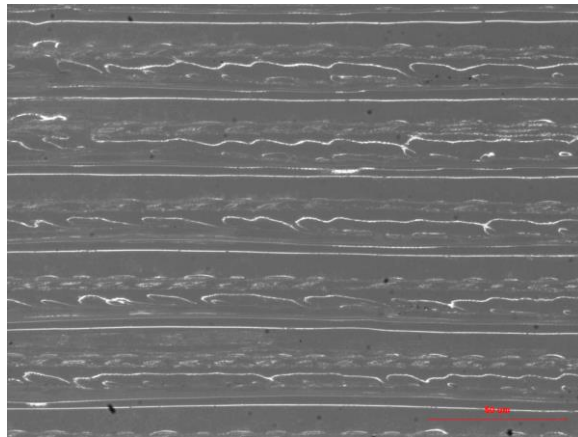
Figure D2: Optical image of specimens for determining RW limit. The gaps between rasters are shown in figure



RW 0.508 mm RRAg -0.022 mm



RW 0.508 mm RRAg -0.030 mm

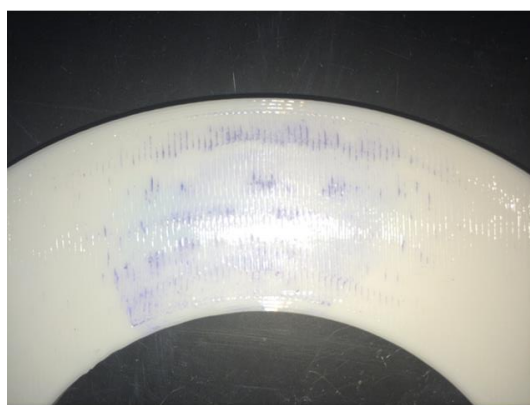


RW 0.508 mm RRAg -0.038 mm

Figure D3: Optical image of rasters deposition using three different RRAgs



RW 0.508 mm RRAG -0.022 mm



RW 0.508 mm RRAG -0.030 mm



RW 0.508 mm RRAG -0.038 mm

Figure D4: Optical view of rasters deposition using three different RRAGs. The blue color was used to visualize the surface more clearly. Note that the bottom image has the higher concentration of blue color indicative of a rougher surface.

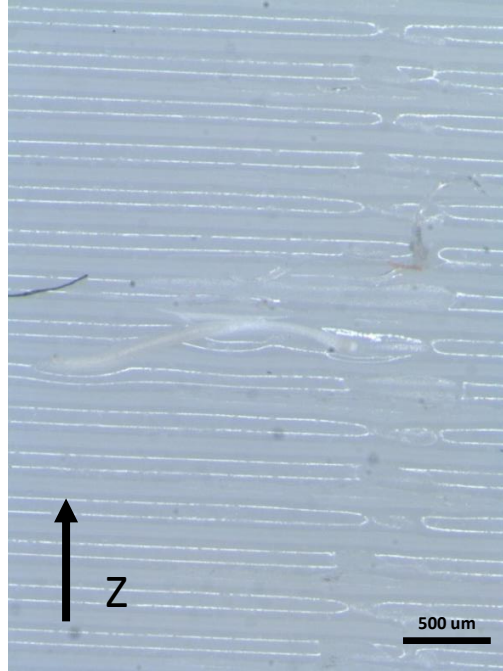


Figure D5: Poor surface finish observed during building in ZXY build orientation

Appendix E

Table E1: RW obtained for square feature using sealing algorithm for each layer. The RWs are in inch

Layer No	RW	Layer No	RW	Layer No	RW
6	0.017	37	0.023	68	0.023
7	0.017	38	0.023	69	0.023
8	0.017	39	0.023	70	0.023
9	0.017	40	0.023	71	0.023
10	0.017	41	0.023	72	0.023
11	0.017	42	0.023	73	0.023
12	0.017	43	0.023	74	0.023
13	0.017	44	0.023	75	0.023
14	0.017	45	0.023	76	0.023
15	0.017	46	0.023	77	0.023
16	0.017	47	0.023	78	0.023
17	0.017	48	0.023	79	0.023
18	0.017	49	0.023	80	0.023
19	0.017	50	0.023	81	0.023
20	0.017	51	0.023	82	0.023
21	0.017	52	0.023	83	0.023
22	0.017	53	0.023	84	0.023
23	0.017	54	0.023	85	0.023
24	0.017	55	0.023	86	0.023
25	0.017	56	0.023	87	0.023
26	0.017	57	0.023	88	0.023
27	0.017	58	0.023	89	0.023
28	0.017	59	0.023	90	0.023
29	0.017	60	0.023	91	0.023
30	0.023	61	0.023	92	0.023
31	0.023	62	0.023	93	0.023
32	0.023	63	0.023	94	0.023
33	0.023	64	0.023	95	0.023
34	0.023	65	0.023	96	0.023
35	0.023	66	0.023	97	0.023
36	0.023	67	0.023	98	0.023

Layer No	RW	Layer No	RW	Layer No	RW
99	0.023	129	0.023	158	0.021
100	0.023	130	0.023	159	0.021
101	0.023	131	0.023	160	0.021
102	0.023	132	0.023	161	0.021
103	0.023	133	0.023	162	0.021
104	0.023	134	0.023	163	0.021
105	0.023	135	0.023	164	0.021
106	0.023	136	0.023	165	0.021
107	0.023	137	0.023	166	0.021
108	0.023	138	0.023	167	0.021
109	0.023	139	0.023	168	0.021
110	0.023	140	0.023	169	0.021
111	0.023	141	0.023	170	0.021
112	0.023	142	0.023	171	0.021
113	0.023	143	0.023	172	0.021
114	0.023	144	0.023	173	0.021
115	0.023	145	0.023	174	0.021
116	0.023	146	0.023	175	0.021
117	0.023	147	0.023	176	0.021
118	0.023	148	0.023	177	0.021
119	0.023	149	0.021	178	0.021
120	0.023	150	0.021	179	0.021
121	0.023	151	0.021	180	0.021
122	0.023	152	0.021	181	0.021
123	0.023	153	0.021	182	0.021
124	0.023	154	0.021	183	0.021
125	0.023	155	0.021	184	0.021
126	0.023	156	0.021	185	0.021
127	0.023	157	0.021		
128	0.023				

Table E2: RW obtained for Circular dome using sealing algorithm for each layer. The RWs are in inch

Layer No	RW	Layer No	RW	Layer No	RW
6	0.02	43	0.016	80	0.017
7	0.02	44	0.016	81	0.018
8	0.02	45	0.016	82	0.021
9	0.02	46	0.016	83	0.021
10	0.02	47	0.023	84	0.018
11	0.02	48	0.017	85	0.021
12	0.02	49	0.017	86	0.021
13	0.02	50	0.017	87	0.017
14	0.02	51	0.016	88	0.021
15	0.02	52	0.016	89	0.02
16	0.02	53	0.016	90	0.018
17	0.02	54	0.017	91	0.016
18	0.02	55	0.017	92	0.02
19	0.02	56	0.016	93	0.016
20	0.02	57	0.016	94	0.017
21	0.02	58	0.019	95	0.018
22	0.02	59	0.017	96	0.017
23	0.02	60	0.02	97	0.018
24	0.02	61	0.02	98	0.017
25	0.02	62	0.02	99	0.017
26	0.02	63	0.019	100	0.017
27	0.02	64	0.019	101	0.024
28	0.02	65	0.02	102	0.024
29	0.02	66	0.022	103	0.021
30	0.016	67	0.019	104	0.018
31	0.016	68	0.019	105	0.021
32	0.016	69	0.02	106	0.016
33	0.016	70	0.022	107	0.02
34	0.016	71	0.017	108	0.018
35	0.021	72	0.019	109	0.018
36	0.017	73	0.02	110	0.017
37	0.017	74	0.017	111	0.018
38	0.017	75	0.019	112	0.019
39	0.017	76	0.019	113	0.023
40	0.017	77	0.017	114	0.02
41	0.016	78	0.017	115	0.017
42	0.016	79	0.016	116	0.019

Layer No	RW	Layer No	RW	Layer No	RW
117	0.023	155	0.016	193	0.018
118	0.016	156	0.018	194	0.02
119	0.016	157	0.017	195	0.016
120	0.018	158	0.016	196	0.017
121	0.021	159	0.023	197	0.021
122	0.023	160	0.018	198	0.017
123	0.021	161	0.017	199	0.022
124	0.022	162	0.018	200	0.017
125	0.016	163	0.016	201	0.017
126	0.016	164	0.016	202	0.023
127	0.017	165	0.018	203	0.021
128	0.017	166	0.017	204	0.017
129	0.021	167	0.02	205	0.017
130	0.019	168	0.023	206	0.019
131	0.019	169	0.025	207	0.021
132	0.016	170	0.016	208	0.025
133	0.02	171	0.016	209	0.021
134	0.017	172	0.017	210	0.022
135	0.017	173	0.019	211	0.016
136	0.02	174	0.02	212	0.017
137	0.016	175	0.018	213	0.018
138	0.018	176	0.025	214	0.023
139	0.016	177	0.016	215	0.016
140	0.017	178	0.017	216	0.018
141	0.016	179	0.024	217	0.021
142	0.016	180	0.017	218	0.025
143	0.016	181	0.024	219	0.018
144	0.016	182	0.022	220	0.023
145	0.019	183	0.017	221	0.024
146	0.019	184	0.024	222	0.022
147	0.02	185	0.02	223	0.019
148	0.019	186	0.018	224	0.024
149	0.02	187	0.016	225	0.022
150	0.017	188	0.022	226	0.024
151	0.017	189	0.023	227	0.023
152	0.017	190	0.017	228	0.018
153	0.016	191	0.025		
154	0.017	192	0.016		

Vita

Mohammad Shojib Hossain was born on May 13, 1989. He is the son of Mrs. Rojina Begum and Mr. Mohammad Mobarak Hossain. Mohammad completed his Bachelor of Science in Mechanical Engineering in March 2012 from Bangladesh University of Engineering & Technology. He received technical scholarship from Bangladesh University of Engineering & Technology. He worked as a Teaching Assistant in The University of Texas at El Paso. He also acted as a judge of the poster presented by LSAMP scholars, UTEP students and visiting undergraduates in UTEP COURI Summer Symposium in August of 2013. Mohammad helped undergraduate students in research, hosted training sessions of different lab equipment and software. He also peer reviewed technical papers and wrote journal paper as well as conference papers.

Permanent address: Vill: South Churain, P.O: Churain, P.S.: Nawabganj,
Dist: Dhaka, Bangladesh.

This thesis was typed by Mohammad Shojib Hossain.